

STREAMER CHAMBER DEVELOPMENT

by

F. Bulos, A. Odian, F. Villa, and D. Yount

June 1967

Technical Report
Prepared Under
Contract AT(04-3)-515
for the USAEC
San Francisco Operations Office

Printed in USA. Available from CFSTI, National Bureau of Standards,
U. S. Department of Commerce, Springfield, Virginia 22151
Price: Printed Copy \$3.00; Microfiche \$0.65

ACKNOWLEDGEMENTS

The development of the two-meter streamer chamber at SLAC represents the culmination of more than three years of effort involving a large number of people. We have space to mention only a few.

Dr. A. Boyarski, Dr. R. Diebold, and Professor B. Richter were among the SLAC physicists who participated in the early phases. The streamer chamber program carried out by Drs. D. Benaksas and R. Morrison at Stanford has provided us with the reassuring information that it is possible to operate streamer chambers in high magnetic fields and that it is practical to use these chambers in the photon beams produced by electron linacs. As is clear from the text, we have benefitted considerably from discussions and numerous private communications with J. C. Martin and I. Smith of AWRE in England, both of whom visited SLAC to contribute in this program.

P. Thingstad, D. Lebet, and R. Bell were the mechanical engineers most closely associated with this work. M. Hargain, C. Jones, A. Omahen, and G. Schultz were closely involved in the construction, assembly, and testing of the various components and systems; they have shared, on a day-to-day basis, our numerous frustrations and occasional successes. In addition, we are grateful for the generous help of the shops and the accelerator staff at SLAC.

Finally, it is a pleasure to acknowledge the support and encouragement of Professor R. Mozley, Dr. D. Drickey, Dr. D. Fries, Dr. I. Derado, and the other members of the streamer chamber group.

TABLE OF CONTENTS

	<u>Page</u>
I. Introduction	1
II. Streamer Theory and Experiment	4
A. Single Avalanche (Townsend Equations)	5
B. Streamer Formation (Meek Equations)	10
C. Experimental Studies of Streamer Brightness	13
D. Experimental Studies of Streamer Diffusion and Memory	16
E. Ionization Measurements in Streamer Chambers	21
III. Optics	27
A. Image Intensifiers Versus Direct Photography	28
B. Selecting the Demagnification and f-Number	33
C. Film, Lenses, and Measuring Machines	36
D. Data Analysis: Streamer Chambers versus Bubble Chambers	41
IV. Chamber Technology	46
A. Single versus Double Gap	46
B. Small versus Large Chambers	47
C. Electrodes	50
D. Cells and Targets	51
E. Purifier	55
V. High Voltage Technology	63
A. Introduction	63
B. High Voltage Generators	68
C. Pulse Shaping Networks	77
D. Pulse Monitoring	85

	<u>Page</u>
VI. Development of the Two-Meter Streamer Chamber	89
A. A Brief History	89
B. Summary of the Final System	96
C. Initial Performance of the Two-Meter Streamer Chamber	104
D. Speculation	108
References	113
Appendix A	117
Appendix B	127
Appendix C	134

LIST OF ILLUSTRATIONS

	<u>Page</u>
1. Streamer tracks with 0.15- μ sec delay in the high voltage pulse, photographed with f/2.8 lens aperture	2
2. Q versus E/p in kV/(cm · torr). Q, which is roughly proportional to 1/E, is the ratio of the rates for producing protons and free electrons during avalanche formation	8
3. α /p versus E/p in kV/(cm · torr). α is the first Townsend coefficient and is roughly proportional to the electric field E.	9
4. Streamer track with 20- μ sec delay in the high voltage pulse. Diffusion of the primary electrons is seen clearly in the view parallel to \vec{E} (left side of picture).	18
5. Projected scatter of the diffused streamer track plotted as a function of the pulse delay τ in μ sec. Essentially this figure indicates the accuracy with which the axis of a streamer track can be found with various pulse delays	19
6. The effects of an admixture of Freon 12 on the memory of the chamber and on the track quality. In (a) the streamer density is plotted as a function of the pulse delay for 14 PPM Freon 12. The time at which the streamer density has dropped to half the T = 0 value is shown in (b) for various concentrations f of Freon 12 in PPM. In (c) the minimum streamer length visible in the side view (f/1.5, RAR 2475 film) is plotted as a function of the memory time	20
7. Streamer gap length distribution for 0.15- μ sec delayed high voltage pulse. The expected distribution is exponential, and the cut-off at about 2.0 mm indicates that approximately 50% of the streamers are prevented from developing by a robbing action between closely spaced streamers. The mean streamer density corrected for robbing is 4.0/cm and the mean gap about 2.8 mm	23
8. Average number of streamers per cm of track length versus the pulse delay in μ sec. Delta rays and bright clusters are excluded in analyzing the streamer data.	24
9. Average number of streamers per cm of track length versus the chamber pressure in atm. Robbing by adjacent streamers is apparently not important below about 0.2 atm.	26
10. Layout for a three-stage image intensifier. The streamer chamber, with maximum depth of field Δu , is on the left and the film plane on the right	31
11. Comparison of Kodak SO 340 film on the left with Kodak RAR 2475 on the right. The exposure was 1/100 sec in each case, and the development was in Nikor Reel D-19 developer at 83°F. The grain density versus time for 3 min, 6 min, 8 min, and 10 min of hand development is given for each film	37

	<u>Page</u>
12. Comparison of hand development on the right with spray machine development on the left. The exposure in each case was 1/100 sec with a W-21 filter, and the development was in modified Dupont x-ray developer at 83° F. The high speed spray developing machine was run at 50 ft/min	38
13. Comparison of effect of forced developing (left) versus standard developing (right)	39
14. Resolution chart photographed with RAR 2475 film on the right and SO 340 film on the left. For RAR 2475 film the large box has fuzzy edges, while for the SO 340 film the edges are quite sharp . . .	40
15. An early single-gap streamer chamber developed at SLAC. The dimensions of the sensitive volume are length 50 cm, width 50 cm, and gap 10 cm	48
16. An early double-gap chamber developed at SLAC. The dimensions of the sensitive volume are length 150 cm, width 45 cm, and double gap 30 cm; the view is from the input end. The outer, ground electrodes have been joined to enclose completely the central high voltage electrode	49
17. Purifier for the 90% neon-10% helium streamer chamber gas. As described in the text, the pump and control unit can be used either with Ca-Na reactors indicated or with a molecular sieve cooled to LN ₂ temperature	56
18. Nitrogen contamination as a function of time. In (a) the flow rate was 2400 liters/hour through a single 900-liter foam cell with the Ca-Na reactors providing the active unit. In (b) the 50-kg molecular sieve at LN ₂ temperature was used to purify a cell containing initially about 50% air(40% nitrogen). The flow rate was 250 liters/hour into one 900-liter cell	60
19. Gas impurities versus the equilibrium flow rate, versus the neon volume flowed per day, and versus the neon cost. A leak rate of 0.01% per hour into two 900-liter foam cells is assumed here and is similar to the actual leak rates observed during tests, including a preliminary run in the photon beam	61
20. Block diagram illustrating the principal elements of the streamer chamber system (a) and a chamber layout to be considered either as a capacitor or as a transmission line (b)	65
21. Streamer track photograph with the 2-meter chamber terminated by an impedance 35% lower than the characteristic value. The ionizing particle was incident from the input end of the chamber where the track is brightest	67

	<u>Page</u>
22. A four-stage, single-polarity Marx generator. The spark gap capacity C_G , the stray capacity to ground C_S , and the interelectrode capacity C_I are shown with dashed lines and should satisfy the condition $C_G \ll C_S, C_I$ for reliable triggering. The trigger capacitor C_T is added to the trigger gap to increase the energy discharged by this gap and thus to increase the light output	69
23. Circuit diagram for the 17-gap, 34-stage Marx generator used to drive the 2-meter streamer chamber. A photograph of this generator is shown in Fig. 38	71
24. Marx generator equivalent circuit. The procedures by which one can determine the capacitance and the internal inductance and resistance of a Marx generator are described in the text	72
25. Circuit for measuring the capacity at a given high voltage (a) and the results of such a measurement (b) made with a barium-titanate capacitor similar to those used in the 17-gap, 34-stage Marx generator	74
26. Schematic drawings of a stacked stripline generator (a) and a spiral generator (b). These and several other generators are discussed in detail in the article by R. A. Fitch and V. T. S. Howell, Ref. 48	76
27. Three pulse shaping networks driven by Marx generators. These are the capacitor with series (S) and shorting gaps (S') shown in (a), the dielectrically loaded line shown in (b), and the Blumlein line shown in (c). Also sketched are the characteristic output pulses for each type of pulse shaping network	79
28. Two views of a system in which the parasitic capacitance C_p has been enhanced and in which series and shorting gaps have been added to a Marx generator to form a pulse shaping network. A photograph of this system is shown in Fig. 32	80
29. Analysis of the operation of a Blumlein line. The five-electrode Blumlein (a) is equivalent to two three-electrode Blumleins (b) each of which can be considered as a constant impedance line interrupted at the center by the load NZ . The first Blumlein pulse begins at time τ after the spark gap fires and continues until time 3τ where τ is the time required for a wave to travel from the spark gap to the end of the charged electrode. When the impedances of the Blumlein and load are properly matched ($N=2$), the amplitude of the first pulse is equal to the charging voltage, and all succeeding pulses are zero	83
30. Charging the Blumlein with a bridge circuit to control the Blumlein prepulse which appears across the chamber. By adjusting the prepulse properly, one can cancel the displacement of the streamer origins which normally occur when a driving pulse of only one polarity is used	86

	<u>Page</u>
31. A resistive probe (a), a capacitive probe (b), and the pulses (c and d) obtained on the 2-meter streamer chamber with each. The pulses are similar for the two probes except for the small amplitude, high frequency ringing in the capacitive case. The pulse amplitude for streamers is nearly 600 kV across the 30-cm chamber gaps. The rise time is 4 nsec and the pulse duration about 12 nsec at half the peak voltage. The characteristic rise time for each probe is about 1 nsec.	87
32. Photograph of a double-gap streamer chamber driven by a Marx generator with an intermediate capacitor and with series and shorting spark gaps used as a pulse shaping network. The chamber, with electrodes in the vertical plane, has a sensitive volume 50 cm wide and 150 cm long with two gaps of 15 cm each. Drawings of this system are shown in Figs. 28 a and b	92
33. Side view of the experimental arrangement for the photoproduction program. A highly collimated, hardened bremsstrahlung beam is incident from the left and passes through a 1/2-inch-diameter hydrogen gas target in the upper of two foam cells	97
34. Top view of the experimental arrangement for the photoproduction experiment. Events which occur in the chamber are photographed stereoscopically by three cameras through the hole left by the absent upper pole piece. The magnet windings, three below and seven above, are unbalanced to compensate for the missing pole piece and to improve the field uniformity	98
35. A three-dimensional, x-ray vision drawing of the experimental arrangement for the photoproduction program	99
36. A photograph of the experimental arrangement for the photoproduction program. The view is similar to that shown in Fig. 35, but the vacuum pipe for the photon beam is not in place	100
37. Photograph of the experimental arrangement for the photoproduction program. In this figure, the beam is incident from the right. The "elbow" can be seen on the right arching from the Marx generator - Blumlein oil tank to the streamer chamber, which passes through the magnet between the visible upper and lower magnet coils. The vertical trigger-counter array, consisting in this case of 16 counters, is supported on the downstream side of the magnet. The trigger electronics is visible on the magnet column nearest the counters. The magnet, including the entire streamer chamber and drive system and the trigger counters, can be driven in and out of the photon beam along the tracks visible in the floor	101

38. Photograph of the 17-gap, 34-stage Marx generator used to drive the 2-meter streamer chamber. A circuit diagram of this generator appears in Fig. 23. The carbon rod resistors used in charging the capacitor stages are not shown in the photograph, but supporting fixtures can be clearly seen. The modular construction permits the rapid removal of any stage in case of capacitor failure, and the spark gap manifold can also be replaced in a matter of minutes. The arrangement of the capacitor stages is designed to enhance the interstage capacity C_I and the stray capacity C_S to ground, while the capacity of each spark gap C_G is minimal. Thus the design satisfies the condition $C_G \ll C_I, C_S$ as discussed in the text. In addition, light emitted from any one gap has an excellent chance to induce photoionization in the succeeding gaps and thus to insure the reliable triggering of all gaps. 103
39. The Blumlein and "elbow" used in shaping the 10-nsec, 600-kV pulse which drives the streamer chamber. The sheet metal which normally encloses the Blumlein and elbow has been largely removed for viewing. The vertical elements of the Blumlein taper outward and upward from the spark gap in such a way that the 23-ohm chamber impedance is everywhere matched and that the electrical paths leading from the gap to the chamber are as nearly equal in length as possible. When mounted in the oil tank with the Marx generator, the Blumlein is emersed in oil up to the point where the Blumlein and elbow are joined. At this point there is a large bulge in the center electrode of the elbow to compensate for the impedance change at the air-oil interface 105
40. Photograph of the streamer chamber installed in the magnet. The sheet metal rf enclosure at the downstream end of the chamber has been removed for viewing. The lucite supports for the central electrode as well as the carbon-rod terminating resistors are clearly visible. A corona guard encircles the central electrode to prevent breakdown at the edges. The electrode itself consists of 0.25-mm wires spaced 1 cm apart and supported on a 1/4-inch-thick aluminum window frame 106
41. Photograph of a foam cell used in the 2-meter streamer chamber. Each cell is 30 cm deep, 150 cm wide and about 230 cm long at the location of the target. Nylon fishline is used here to space the mylar windows away from individual electrode wires so that breakdown does not occur. In later models, 1/8-inch-diameter lucite rods are used in place of the nylon, and the spacing between the rods is increased to 6 inches. The hydrogen gas target is supported under tension by the lucite fixtures at each end. The target can be pressurized to about 60 psig to enhance the signal-to-background ratio for backgrounds not originating in the target 107
42. A K^0 decay which occurred in the 2-meter streamer chamber during the first preliminary run in the photon beam 109

	<u>Page</u>
43. A nuclear interaction event which occurred in the streamer chamber during the first preliminary run in the photon beam	110

Appendix A

A. 1. DC electric field for breakdown in several gases versus the gas pressure. This figure was obtained originally by A. Kusko and has been recopied from Fig. 2 of the article by J. G. Trump, Ref. 1	118
A. 2. Breakdown electric field versus pulse duration for several gases. This figure was recopied from the article by P. Felsenthal and J. M. Proud	120
A. 3. Electric field for pulse breakdown in transformer oil versus the electrode area. These are unpublished data communicated to us by J. C. Martin and I. Smith of AWRE	122
A. 4. Electric field for pulse breakdown in deionized water versus the electrode area. These are unpublished data communicated to us by J. C. Martin and I. Smith of AWRE	123
A. 5. Electric field for pulse breakdown in thin sheets of mylar, lucite, and polyethylene versus the sample volume in cm ³ . These are unpublished data communicated to us by J. C. Martin and I. Smith of AWRE	125

Appendix B

B. 1. Switch equivalent circuit (a) and the time dependence of the voltage across a triggered gap (b).	128
B. 2. Schematic drawing of a triggered spark gap. The trigger needle is located at the center of the lower electrode, and its penetration into the gap can be adjusted by turning the larger threaded shaft to which the needle is attached. A cylindrical ceramic insulator is imbedded in the lucite which surrounds the threaded shaft, and it is used to isolate the trigger needle as it passes through the lower electrode.	131

Appendix C

C. 1. Layout and construction details for the autotransformer developed by J. C. Martin and I. Smith of AWRE	135
C. 2. Three different circuit configurations for the autotransformer developed by J. C. Martin and I. Smith of AWRE	136

C.3. Equivalent circuit for the autotransformer developed by J. C. Martin and I. Smith of AWRE 138

C.4. Calculated rise time in nsec for $V_{out}/V_{in} = 800 \text{ kV}/50 \text{ kV}$ versus b_{max} , the maximum width of the tapered autotransformer winding. Calculations were made for the three circuit configurations indicated and for the transformer radii shown with each curve. Additional parameter values are included in the text 140

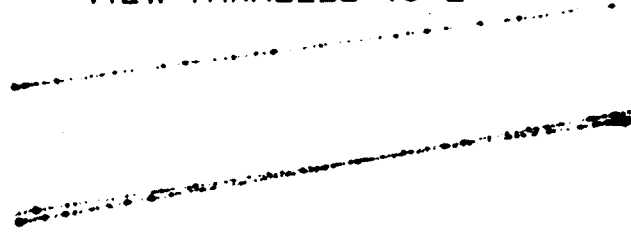
C.5. Calculated output voltage maximized with respect to the number of turns in a center-tap autotransformer versus the output rise time in μsec . The maximum width b_{max} of the tapered winding, and the radius r identify the different curves. Additional parameter values are included in the text 141

I. INTRODUCTION

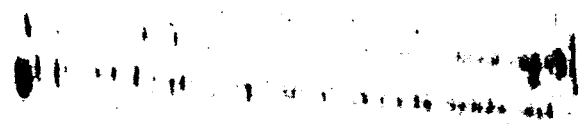
The continuing interest in spark chamber development has recently led to two new types: the wide-gap spark chamber¹⁻⁸ and the wide-gap streamer chamber.^{5,9-19} In the first of these, the magnitude and length of the high voltage pulse permit spark formation and a continuous discharge along a particle path which necessarily extends between the high voltage plates. In the streamer chamber, however, the discharge is arrested at an early stage so that the track, when viewed perpendicular to the field, appears as a series of streaks (streamers) whose length and brightness depend upon the parameters of the high voltage pulse. When viewed through transparent electrodes along the electric field and parallel to the streamer axes, the track appears as a series of dots similar to a track in a bubble chamber. An example is shown in Fig. 1.

Work at SLAC has concentrated on streamer chambers rather than wide-gap spark chambers for several reasons. The isotropy, multiple track efficiency, and track following capability are superior for the streamer chamber, and vertices which occur in the chamber gas are clearly visible. Like wide-gap and conventional spark chambers, streamer chambers have an important advantage over bubble chambers as far as SLAC is concerned. Because they are triggered, they can use the full 360-cycle repetition rate and are not, for example, limited by the intensity that can be obtained in a secondary beam during one pulse. Streamer chambers are preferred over conventional spark chambers on the basis of multiple track efficiency and isotropy, and they may also provide useful ionization data. The long memory of the streamer chamber ($\sim 200 \mu\text{sec}$), which can be shortened, is not a problem here since the duration of the linac pulse is only $\sim 1.5 \mu\text{sec}$ and since pulses are separated by $\sim 2800 \mu\text{sec}$ at 360 cycles/second. Poor light output in the streamer

VIEW PARALLEL TO \vec{E}



VIEW PERPENDICULAR TO \vec{E}



285-8-4

FIG. 1--Streamer tracks with 0.15- μ sec delay in the high voltage pulse, photographed with f/2.8 lens aperture.

mode is, however, a serious limitation; but fast films (ASA > 1000), small f-numbers ($\sim f/2$), and high demagnification (~ 70) provide an acceptable solution.

A particular goal has been the development of a working chamber of large sensitive volume ($\sim 2 \text{ meters}^3$) for use in photoproduction experiments. In this application the chamber is operated in a magnetic field and is triggered in such a way as to minimize biases while at the same time providing a highly enriched sample of events. A thin cylindrical hydrogen gas target is inserted into the streamer chamber, and interactions from a pencil photon beam produce events similar in character to those seen in a hydrogen bubble chamber except that the vertex is not visible. The solid angle, however, is essentially 4π for the events of interest.

In this article a detailed account is given of our present understanding of streamer chamber technology. This involves streamer theory, various properties and experimental observations relating to streamers, optics, chamber and high voltage technology, and finally a brief comparison of data analysis problems for streamer and bubble chambers. It includes most of the formulae, rules of thumb, recipes, impressions, and helpful hints we have gathered in the course of developing the 2-meter chamber. Most of what we have to say is well known, at least to specialists in the related fields; but we feel it is useful to collect in one place the information which relates to this recent and rapidly developing application.

II. STREAMER THEORY AND EXPERIMENT

A great deal of theoretical and experimental work has been done on gaseous discharge, spark gaps, and spark formation over the past 70 years.²⁰⁻²⁹ A quantitative theory of the initial avalanche phase at low pressures was developed by Townsend²⁰ by 1914, and the transition of an avalanche into a streamer was observed experimentally by Raether³⁰ in 1937. The semi-empirical conditions under which this occurs were worked out by Meek³¹ and by Raether³² shortly thereafter. Unfortunately, a quantitative description of the streamer phase has not yet been achieved, principally because the spectral distributions and the effectiveness of the photons involved in the photo-ionization mechanism are poorly understood.

Our own interest is in producing short streamers of sufficient brightness for photography. What we hope to get from avalanche theory is then some indication of how the brightness depends upon the duration and amplitude of the applied field when the photographable streamer length is constrained. In Section A we review the avalanche phase of streamer formation and outline the classical methods which have been used to study these phenomena. In Section B we consider the transition from the avalanche to the streamer phase and derive two relationships between avalanche brightness and the duration and amplitude of the applied field. These relationships, based on avalanche theory, are not expected to hold for real streamers but are the best we can do in the absence of a quantitative streamer theory. In Section C we summarize our own observations concerning streamer brightness and relate these to the theory developed in Sections A and B.

Before discussing avalanche theory, we should point out that the light emitted by streamers consists of discrete spectral lines and not of a continuum of black-body radiation. If all of the energy of the driving pulse incident on the streamer is absorbed, the energy density $\epsilon_0 E^2$ times the streamer volume V is of the order

of 10^{-11} joules. Assuming this energy is distributed uniformly throughout the streamer volume and using the law of Dulong and Petit to calculate the specific heat, we obtain a temperature rise of order 10^{-5} °C. This means, in effect, that only a small fraction of the atoms in the gas are participating in the photon emission.

A. Single Avalanche (Townsend Equations)

Three basic methods have been used to study the avalanche process in a gas.²⁹ In the cloud chamber method, the ions produced by ionizing collisions of the electrons in the avalanche act as condensation nuclei upon which the supersaturated cloud chamber vapor condenses to form visible droplets. This technique is sensitive to a single ion in the avalanche and is particularly useful in studying the spatial distribution of the ions after a pulse of a given amplitude and duration has been applied. In the electrical method, the drifting electrons and ions of the avalanche produce an electrical current during their transit time. This pulse can be displayed on an oscilloscope and provides a continuous record of the avalanche current as a function of time.

In the optical method, the drifting electrons of the avalanche excite the gas molecules and cause them to emit light. A photomultiplier can be used to convert the light into an electrical pulse which can then be displayed on an oscilloscope as in the electrical method. If an image intensifier is used to collect the light, the spatial distribution can also be studied as in the cloud chamber method. Under suitable conditions direct photography is barely possible. The optical method is of particular interest in the case of streamer chambers since the information contained in a track consisting of many adjacent streamers can only be extracted in this way. An indication of the brightness per electron in the avalanche is given by experiments involving a single avalanche in which the optical and electrical methods are used simultaneously.

Let us consider now what happens when an electric field acts on an electron left by an ionizing charged particle. For a sufficiently high field, the energy lost by elastic collisions ($\propto 2m/M$ where m and M are the masses of the electron and atom, respectively) is negligible, and the electron continues to gain energy until it multiplies by ionization. This assumes a small energy loss due to the excitation of atomic levels. The total number of drifting electrons grows as

$$n_-(x) = \exp(\alpha x) . \quad (1)$$

The first Townsend coefficient α is the mean number of ionizing collisions made by one electron per cm; thus the mean free path for ionization is $1/\alpha$. The variable x is the length attained by the avalanche and is given as a function of time t by the equation

$$x = v_- t = bEt \quad (2)$$

where v_- is the drift velocity of the electrons, b is the electron mobility, and E is the electric field. The drift velocity for electrons is typically about 10^7 cm/sec (1 mm/10 nsec) and for ions about 10^5 cm/sec.²⁹ Thus the ions are virtually stationary during the interval (~ 10 nsec) of interest here.

Because of the diffusion of the electrons perpendicular to the field, the radius of the avalanche also increases as a function of time. Roughly 85% of the electrons are contained within a spherical cloud of radius r given by

$$r^2 = 4Dt \propto E^{1/2} t \quad (3)$$

where at zero field the diffusion coefficient D is finite and proportional to the thermal energy.²⁹ The approximate relationship, $D \propto E^{1/2}$, is verified experimentally.³³ For an electric field E and pressure p such that $(E \text{ V/cm})/(p \text{ torr}) \sim 20 \text{ V/(cm torr)}$ (e.g., 15 kV/cm/760 torr), the radius is of the order of 1 mm or less after 10 nsec.

It is generally assumed²⁹ that the number of photons created between t and $t + dt$ is proportional to the total number of drifting electrons:

$$dp(t) = \delta n_-(t) v_- dt \quad (4)$$

where δ is the number of photons produced by one electron per cm. (The mean lifetime of the excited states is assumed to be small compared to $1/\alpha v_-$.) The number of drifting electrons can be found as a function of time by substituting x from Eq. (2) into the Townsend equation, Eq. (1):

$$n_-(t) = \exp(\alpha v_- t). \quad (5)$$

The number of electrons produced in dt is then

$$dn_-(t) = \alpha n_-(t) v_- dt. \quad (6)$$

Thus both the number of photons and the number of electrons produced are proportional to the number of drifting electrons. This can be expressed as

$$dp(t) = Q dn_-(t), \quad (7a)$$

$$Q = \delta/\alpha. \quad (7b)$$

Experimentally Q is roughly proportional to $1/E$, while the first Townsend coefficient α goes as E . These features are illustrated in Figs. 2³⁴ and 3³⁵. They indicate that δ is, to some approximation, independent of E . The order of magnitude of Q is unity at 1 atm pressure and at $E/p \sim 15-20$ kV/(cm torr). An avalanche containing 10^8 electrons will thus emit 10^8 photons of which 10^3 might be collected and focused by a lens. If the film sensitivity is one 7-micron grain per 10^3 photons, then at most only 1 grain will be formed, and the avalanche will not be detectable. The number of electrons and photons in a streamer is one or two orders of magnitude higher than in an avalanche.

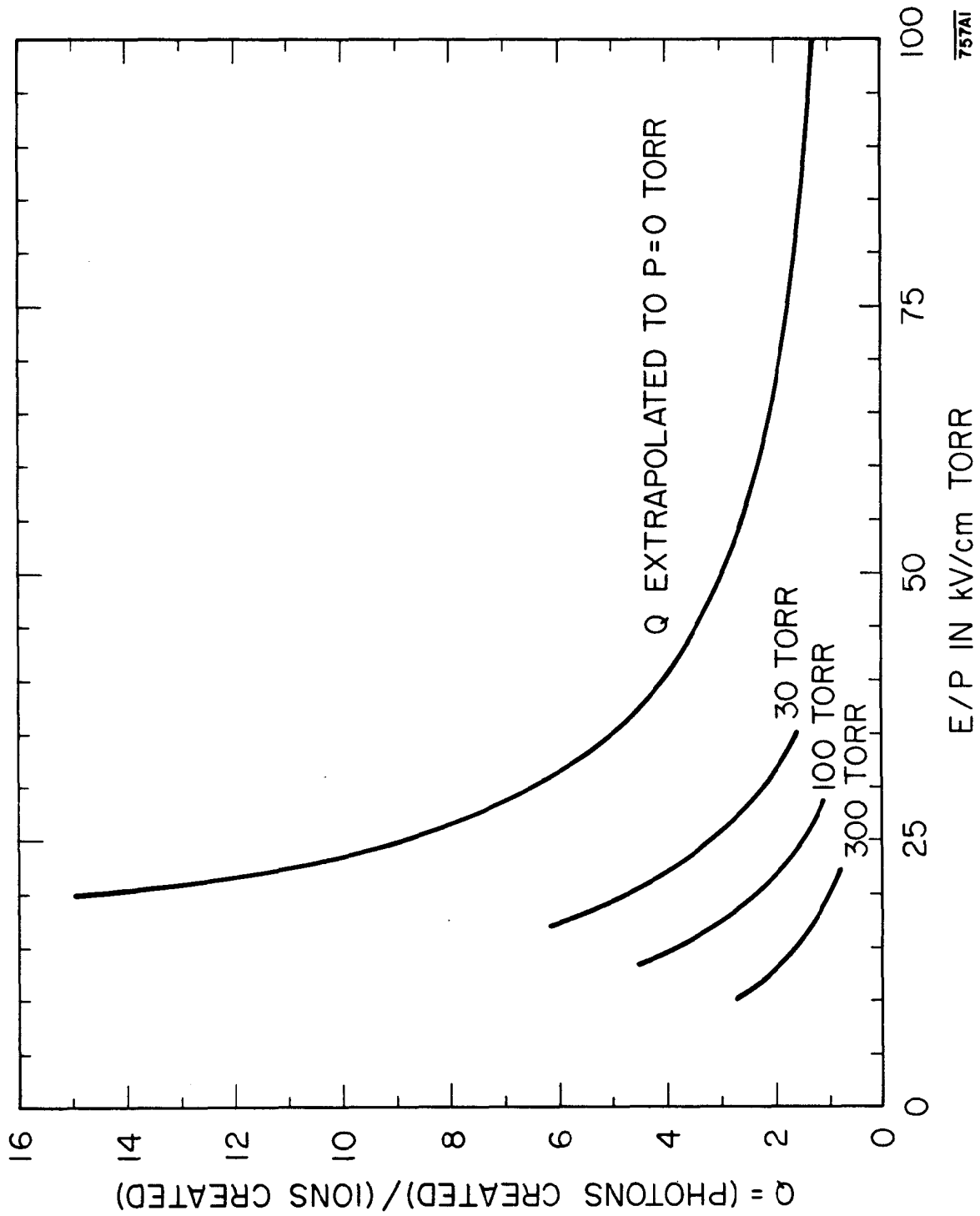
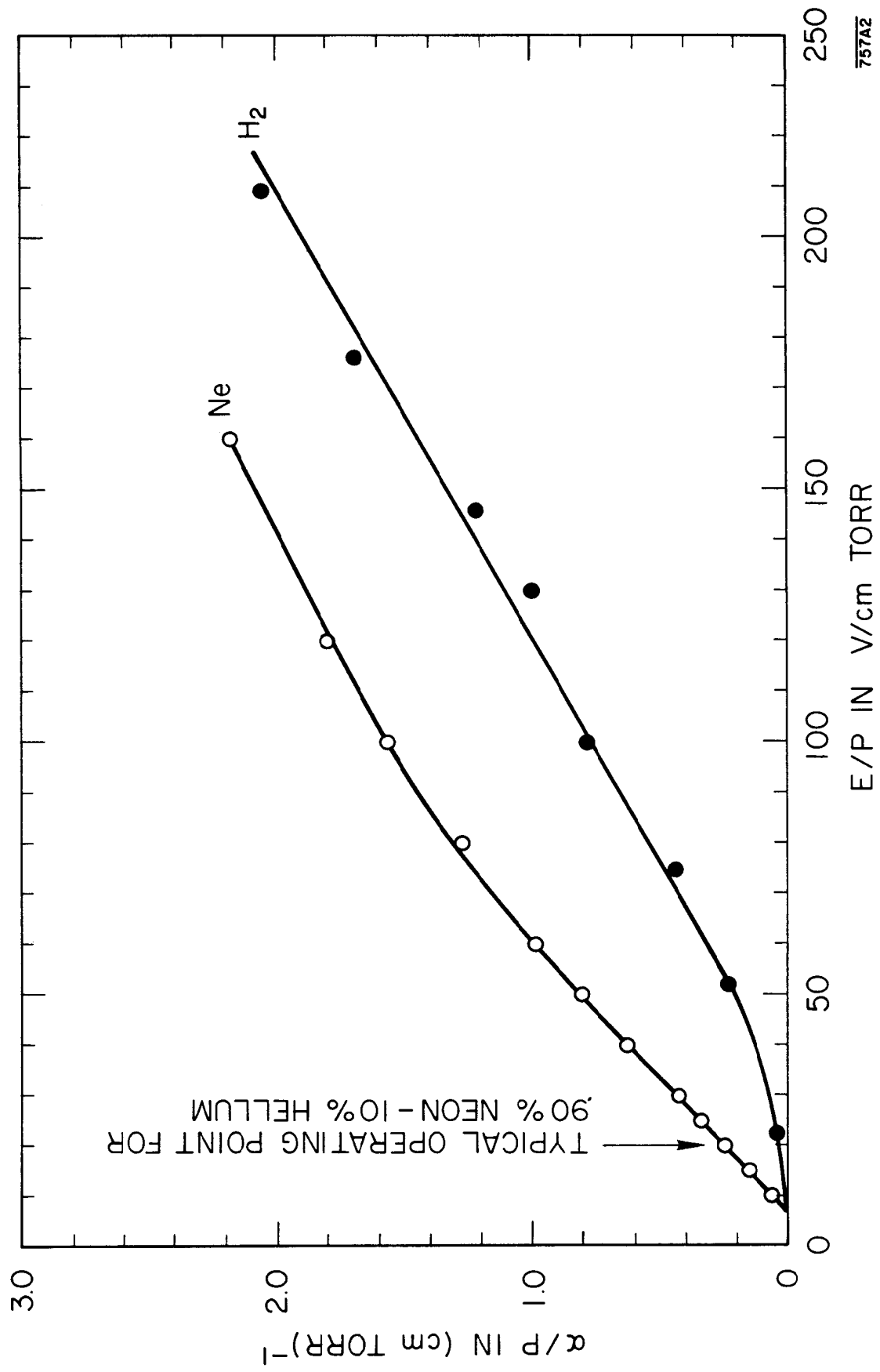


FIG. 2-- Q versus E/p in $\text{kV}/(\text{cm} \cdot \text{torr})$. Q , which is roughly proportional to $1/E$, is the ratio of the rates for producing photons and free electrons during avalanche formation.



757A2

FIG. 3-- α/p versus E/p in $kV/(cm \cdot torr)$. α is the first Townsend coefficient and is roughly proportional to the electric field E .

B. Streamer Formation (Meek Equations)

After a certain point, the space charge developed by the avalanche itself transforms the avalanche into a streamer. A striking feature of this transformation is the rapid longitudinal extension of the streamer, which occurs at a rate of at least 10^8 cm/sec²⁹ (1 cm/10 nsec). This is an order of magnitude faster than the drift velocity of the electrons and the rate of extension of the primary avalanche, and it indicates that a different mechanism or mechanisms are involved.

When the applied field is only slightly higher than is required for streamer formation, the growth is toward the anode from the region of highest electron density in the avalanche. This can be due either to the increased electron velocity in the perturbed field or to photo-ionization. A still higher field leads to growth also in the cathode direction, and this can be explained only by photo-ionization.

In the case of streamer chambers, the applied field is 5 to 10 times the field required for static breakdown. After the primary avalanche is formed, the dominant process is ionization by photons produced in the original avalanche. These are emitted isotropically and produce other electrons and photons in the gas by photo-ionization. The additional electrons produce localized secondary avalanches, particularly near the positive and negative tips of the original avalanche, where the field is intensified by the additional space charge. The new avalanches feed the tips of the original avalanche symmetrically, leaving behind space charge which extends the streamer symmetrically in both the anode and cathode directions. The threshold for streamer breakdown is set by the condition that the secondary avalanches be self-sustaining, e. g. , that the electrons feeding the positive tip of the primary avalanche, and thus neutralizing it, leave behind positive ions equal in density to those that existed in the primary avalanche.

Notice that although the streamers themselves are symmetrical, they originate in the head of the original avalanche where the space charge density is highest. Thus, their centers are displaced from the origin of this avalanche by a distance $v_- t_M$ where t_M is the time required to reach the streamer phase. For short streamers, the total pulse duration τ is only a few nsec longer than t_M .

The critical point in the development of a streamer occurs when the density of the electrons is so high that the resulting field is a significant fraction of the applied field. The number of electrons in dx is $dn_-(x) = \alpha \exp(\alpha x) dx$, and these are contained within a volume $\pi r^2 dx$. The electron density is then given by

$$\rho_-(x) = \alpha \exp(\alpha x) / \pi r^2 \quad (8)$$

and the space-charge field strength at a distance r inside or at the edge of the avalanche is given in MKS units by

$$E' = e \alpha \exp(\alpha x) / 3 \pi \epsilon_0 r \propto \alpha \exp(\alpha x) / r \quad (9)$$

where e is the charge of the electron and ϵ_0 is the permittivity constant.

In practice, the space-charge field becomes a significant fraction of the applied field when

$$\exp(\alpha x_M) \sim 10^8 \quad (10a)$$

$$\alpha x_M \sim 20 \quad (10b)$$

$$x_M \sim 20/\alpha \quad (10c)$$

As already noted, α is roughly proportional to the external field E , so that the critical avalanche length or "Meek length" (and thus the displacement of the streamer centers) goes inversely as the applied field. Putting $x_M \propto E t_M \propto 20/E$, we observe that the Meek criterion is equivalent to the requirement:

$$E^2 t_M = \text{constant} . \quad (10d)$$

In the range from 0.1 to 1.0 atm in a 90% neon-10% helium gas mixture, we have observed that the value of $E^2 \tau/p$ for photographable streamers is typically 2500-3500 (kV/cm)² nsec/atm where τ is again the duration of the driving pulse.

We will conclude this section by considering the question: What is the dependence of avalanche brightness upon the amplitude [or upon the duration via Eq. (10d)] of the applied field when the Meek criterion is satisfied? Before doing so, we should point out that the Meek criterion is in no sense a condition for constant streamer length or even for constant avalanche length. We have already seen explicitly that the length of the avalanche is constant when Et is constant and not when $E^2 t$ is constant. When the Meek condition is satisfied, the length of the avalanche (Meek length) varies inversely as the field. Furthermore, these results may have no relevance at all when photo-ionization becomes the dominant process.

We shall define the avalanche brightness perpendicular to the applied field to be proportional to the number of photons emitted, divided by the projected area of the avalanche. The data obtained with the optical and electrical methods give

$$\begin{aligned}
 B_{\perp} &\propto \text{total number of photons/avalanche area} \\
 &\propto Q n_{-}(t)/rx \\
 &\propto (E^{-1}) [\exp(E^2 t)] / (E^{-3/4})(E^{-1}), \quad (11a) \\
 B_{\perp} &\propto E^{3/4}.
 \end{aligned}$$

Our second derivation is based on the assumption that the brightness per unit avalanche length is proportional to the product of Q ; of $\rho_{-}(x)$, the density of electrons at the point x ; and of r , the depth of the streamer along the line of sight.

This gives, from Eqs. (3) and (8):

$$\begin{aligned}
 B_{\perp} &\propto Q \rho_{-}(x) r \\
 &\propto (E^{-1}) [E \exp(E^2 t) / E^{-3/2}] (E^{-3/4}), \\
 B_{\perp} &\propto E^{3/4}. \quad (11b)
 \end{aligned}$$

The brightness seen along the avalanche axis is given by

$$\begin{aligned}
 B_{||} &\propto Q n_-(t)/r^2 \\
 &\propto (E^{-1}) \left(\exp(E^2 t) \right) / (E^{-3/4})^2, \\
 B_{||} &\propto E^{1/2}.
 \end{aligned}
 \tag{12}$$

We emphasize again that the equations just derived for the brightness apply only to avalanches and only when the Meek criterion is satisfied. With this constraint, we cannot vary the field without changing the avalanche radius and length; thus the compactness of the avalanche is an important factor in determining the calculated brightness in either view. In particular, if the radius r is not resolved, the brightness in the side view is independent of the field, and in the end-on view the brightness decreases as $E^{-1/4}$. In spite of their limitations, the brightness equations for avalanches clearly imply that brighter streamers will result if the field is increased and the pulse duration decreased so that the streamer length remains constant. The point is that the brightness increases (or is nearly constant) with E , while the Meek length decreases. We can therefore exceed the Meek condition and let E increase with constant t in such a way as to hold the streamer length constant. Thus the brightness with constant streamer length varies even faster with E than does the avalanche brightness when the Meek condition is satisfied.

C. Experimental Studies of Streamer Brightness

We have investigated the dependence of streamer length and brightness on the parameters of the high voltage pulse experimentally.¹⁶⁻¹⁸ Cosmic ray tracks were photographed on Kodak 2475 film both directly and with image intensifiers, and various pulses ranging in duration from about 7 to about 22 nsec and in amplitude from about 11 to about 22 kV/cm were tried. For each pulse, the f-number was increased in steps of 1/4 f-stop from 1.5, the minimum available, up to 11, a

value well past cut-off (i . e . , well past the point at which streamers on the average become too faint to be practically useful). For each f-stop, at least 10 tracks were photographed, and from these data the f-number at cut-off was determined. The results are given in Table I.

Such measurements are difficult because of the unavoidable fluctuations of the pulse parameters and the possible, though mild, variation of the light output with the degree of ionization by particles producing the track,⁵ a factor which was not controlled in this experiment. Furthermore, the pulse rise time is not negligible, the optical resolution changes with the f-number, the streamer radius is not resolved in either view and is not expected to be constant for a constant streamer length, and finally the threshold of the film introduces a somewhat arbitrary cut-off on the streamer length and brightness that can be observed. On the other hand, the experimental conditions are precisely those which one must accept in photographing streamer chambers; thus, these data have for us some practical value.

In our earlier interpretation¹⁸ of the brightness data for direct photography, we assumed that the square of the f-number at cut-off was proportional to the brightness B in the streamer view perpendicular to the field and proportional to the total light output TL in the view along the field. We then assumed that each of the properties L , B , and TL followed a power law of the electric field E in kV/cm and of the pulse width τ in nsec:

$$(\text{property})_i \propto E^{x_i} \tau^{y_i} . \quad (13)$$

For each property, a fitting program was used to find the best values of x and y for the different E , τ groups. These results are given in Table II.

TABLE I

Direct Photography				
τ (nsec)	E (kV/cm)	L (mm)	f-number at cut-off end view	f-number at cut-off side view
8.7	17.0	4.7	2.6	2.2
10.4	18.4	6.5	3.7	2.6
17.2	14.6	4.4	2.4	2.0
6.9	21.2	5.3	4.1	3.4
7.9	18.6	5.9	3.7	3.1
19.2	13.2	3.7	2.2	2.2
Image Intensifier				
τ (nsec)	E (kV/cm)	L (mm)	f-number at cut-off end view	f-number at cut-off side view
6.7	17.0	1.9	2.8	2.8
7.2	22.4	3.3	8.0	8.0
18.0	12.5	2.5	4.8	4.8
6.9	18.2	1.2	4.0	4.0
22.1	11.3	2.0	2.8	2.8

TABLE II

Property	x	y
Streamer Length L	4.7 ± 0.9	1.16 ± 0.32
Streamer Brightness B	2.4 ± 0.6	-0.09 ± 0.23
Total Light TL	5.2 ± 1.0	1.03 ± 0.38

The ratio of the power of E to that of τ indicated by Table II is large for all three properties. While the length of a primary avalanche is constant for constant $E\tau$ and while the Meek condition is reached for constant $E^2\tau$, the length of photographable streamers is roughly constant when $E^5\tau$ is fixed. This, like the observed streamer symmetry, is clear evidence for the importance of the photo-ionization

mechanism in our own case. We are not photographing avalanches, but rather true streamers arrested early in their development.

As already noted, the brightness data are subject to a number of experimental reservations. Furthermore, the analysis in terms $E^x \tau^y$ has little to recommend it, either a priori or a posteriori. In the first place, we are dealing not with a single process but rather with two successive processes: electron multiplication and photo-ionization, which becomes dominant after the electron multiplication has run its course. At the very least, we should separate τ into two parts, the time t_M required for avalanche formation and the time t_S remaining for streamer growth. In the second place, the fits obtained in Table II are not especially good, nor do the data for each property permit the determination of more than two parameters, as would be required if one assumes a more complicated functional dependence.

The principal thing which we have concluded from the brightness data is that short streamers occur at 1 atm when $E^2 \tau$ is in the range from 2500 to 3500 $(\text{kV/cm})^2 \text{ nsec}$. Beyond that, we can state only that within our operating range the brightness seems still to be increasing with increasing field when the pulse duration is shortened to maintain constant streamer length.³⁶ More explicitly, if we set $L = \text{constant}$ in Table II, we obtain

$$B \propto E^{2.8 \pm 1.2} \quad (14a)$$

$$TL \propto E^{1.0 \pm 2.3} \quad (14b)$$

D. Experimental Studies of Streamer Diffusion and Memory

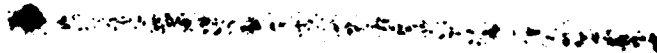
In studying streamer diffusion and memory, a 30-cm \times 30-cm \times 12-cm chamber was used.¹⁸ The chamber was filled with a mixture of 90% Ne - 10% He, and cosmic ray tracks were photographed with variable pulse delays ranging

from 0.15 μ sec to 200 μ sec. Figure 4 illustrates the diffused character of the track which results from the high voltage pulse delay.

In Fig. 5 the accuracy σ with which the axis of a diffused streamer track can be found is plotted as a function of the pulse delay. Equation (3), which was used to estimate the diffusion during avalanche formation, should also be valid for the diffusion of individual streamers at zero field. Thus the apparent width of a track should increase according to this equation. Similarly, the accuracy or scatter, which depends upon the measurer's ability to find the center of a diffused track, should also increase as $t^{1/2}$; but the "diffusion constant for scatter" D_s will be different. The data are in good agreement with the expected dependence $\sigma \propto t^{1/2}$; but the diffusion constant for scatter D_s is 412 cm^2/sec , more than a factor of 5 smaller than the accepted value for ordinary diffusion.²⁹ Measurements of track width agree with the accepted diffusion constant, indicating that in this case, the measurer was able to determine the track center to about 1/5 of the width.

A chamber 15 cm \times 15 cm \times 6 cm was used¹⁸ to study the effect of admixtures of several promising gases on memory reduction. To speed up data taking, β rays from an Sr^{90} source were used with thin counters and windows. Freon-12, ethylene, and methane were all found to be effective in reducing the chamber memory to less than 5 μ sec without decreasing the light output appreciably. SO_2 , while effective in reducing the memory, has undesirable side effects. Figures 6a, b, and c show the results of a detailed study of the effect of a few parts per million admixture of Freon-12 on the memory of the chamber and on the track quality. It is clear that the memory of the chamber can easily be reduced to 1 μ sec or less if desired. As mentioned in the Introduction, memory is not a problem at SLAC where the linac pulse is only 1.5 μ sec, 360 cycles/second.

VIEW PARALLEL TO \vec{E}

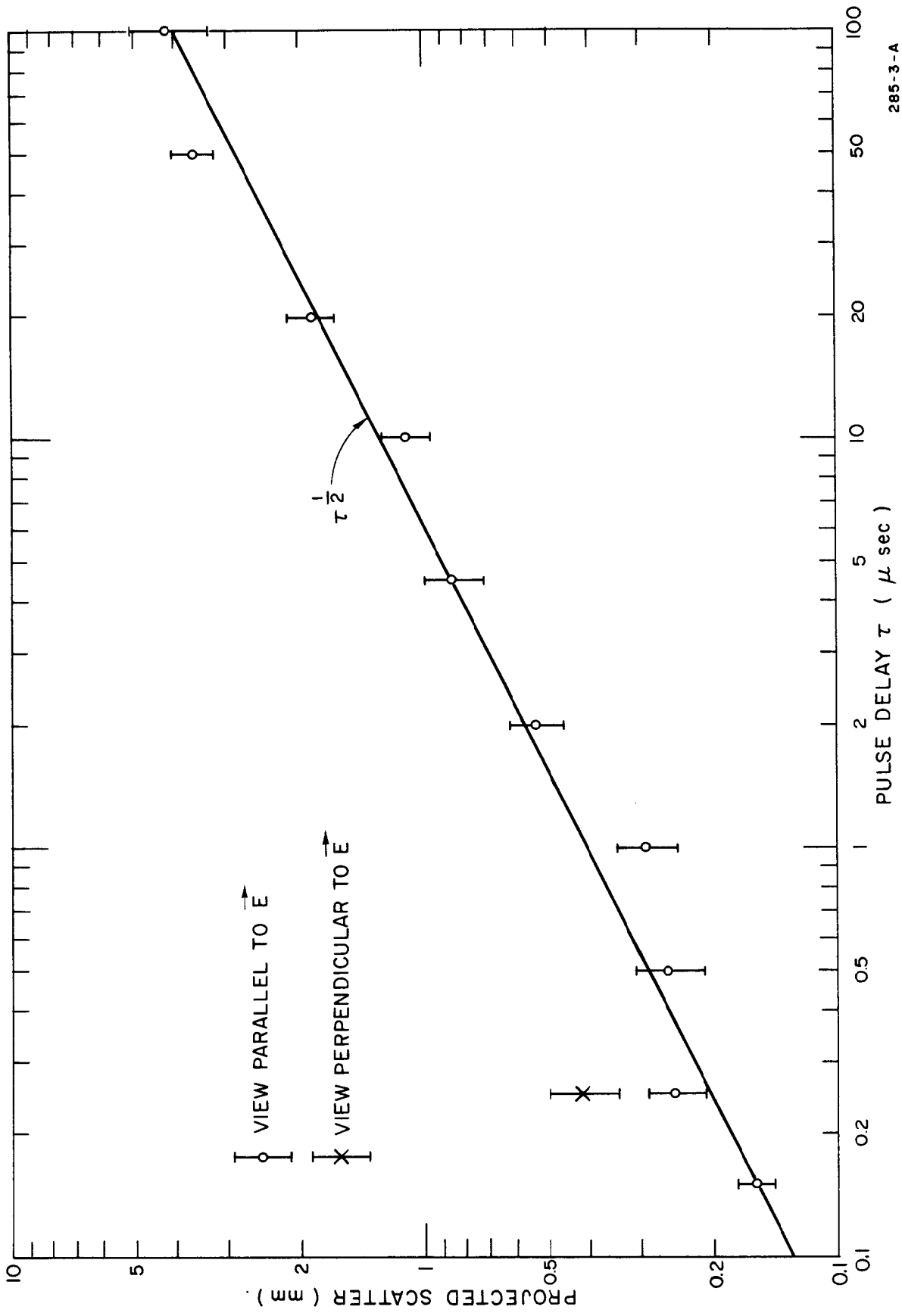


VIEW PERPENDICULAR TO \vec{E}



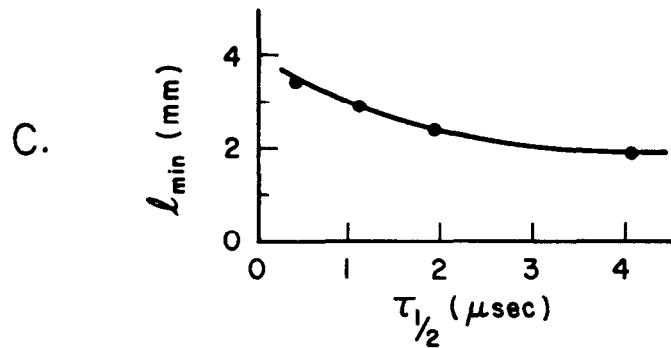
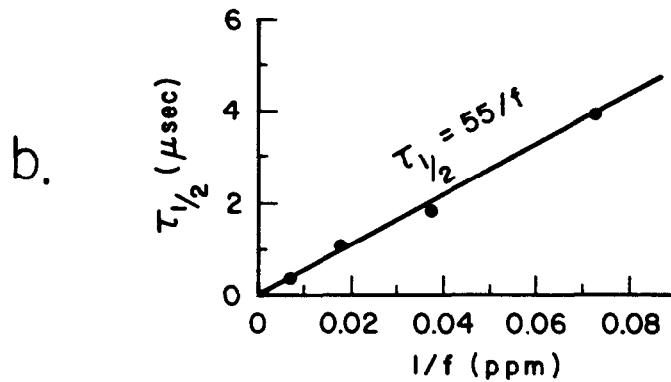
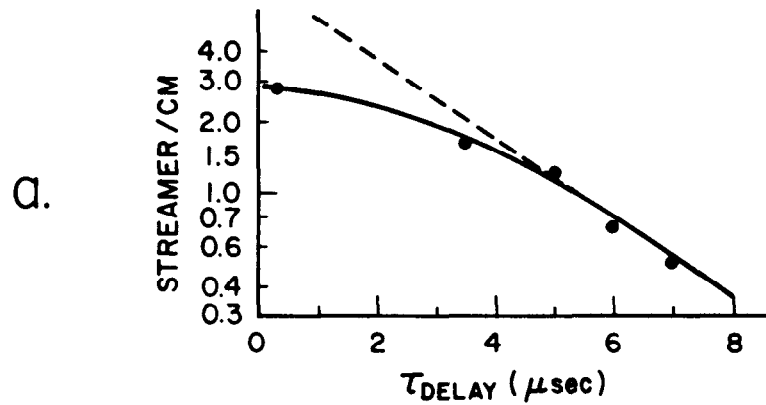
2B5-9-4

FIG. 4--Streamer track with 20- μ sec delay in the high voltage pulse. Diffusion of the primary electrons is seen clearly in the view parallel to \vec{E} (top part of picture).



285-3-A

FIG. 5--Projected scatter of the diffused streamer track plotted as a function of the pulse delay τ in μ sec. Essentially this figure indicates the accuracy with which the axis of a streamer track can be found with various pulse delays.



757A5

FIG. 6--The effects of an admixture of Freon 12 on the memory of the chamber and on the track quality. In (a) the streamer density is plotted as a function of the pulse delay for 14 PPM Freon 12. The time at which the streamer density has dropped to half the $T = 0$ value is shown in (b) for various concentrations f of Freon 12 in PPM. In (c) the minimum streamer length visible in the side view ($f/1.5$, RAR 2475 film) is plotted as a function of the memory time.

E. Ionization Measurements in Streamer Chambers

The theory outlined above for track formation in streamer chambers leads one to believe that ionization measurements on these tracks should be possible. This belief is strengthened by the striking similarity of streamer and bubble chamber tracks and by the wide use made of ionization data in the latter case.

Five properties of streamer tracks are expected to depend upon primary ionization:

1. the gap length distribution between adjacent streamers;
2. the number of gaps per unit length;
3. the number of streamers per unit track length;
4. the track brightness as measured by the degree of darkening of the film;
5. the streamer length viewed perpendicular to the electric field.

The first three properties are closely related and are analogous to gap length distribution, gap counting, and bubble counting used in the case of bubble chambers and to the corresponding properties used in the case of emulsions. Streamer brightness and length have also been studied extensively,^{5,10,37} both experimentally and theoretically. Unfortunately, as we have seen, the streamer brightness and particularly the streamer length vary rapidly with the magnitude E of the applied field and with the angle between the track and the field. The difficulties in regulating the characteristics of the high voltage pulse across a large chamber have persuaded us at SLAC to concentrate on the counting properties.

In our first study of ionization,^{17,18} 80 tracks produced by a momentum-analyzed beam of "minimum ionizing" pions were measured and compared with 40 proton tracks that were 2.3 times minimum ionizing. The ratio of proton to pion streamer densities in 90% neon - 10% helium at 1 atm pressure was only 1.2, considerably less than the 2.3 ionization ratio. We also chose a few tracks of 600-MeV/c protons obtained during the same run and studied the gap length distribution for these using the method of Ref. 38. The results are shown in

Fig. 7. The expected distribution is exponential, and the cut-off at about 2.0 mm indicates that approximately 50% of the streamers are prevented from developing by a robbing action between closely spaced streamers. The mean streamer density corrected for robbing is 4.0/cm and the mean gap 2.8 mm. This density is an order of magnitude smaller than the mean number of ions left by the track.

It was noticed during the diffusion studies of Section D that when the high voltage pulse was delayed, the number of photographable streamers increased to a certain value. The fact that it did not decrease thereafter removed the possibility that the discrepancy between the number of streamers and the number of primary ions was due to electron recombination or attachment during the high voltage pulse delay, and it suggested a method of eliminating the robbing effect. One simply delays the high voltage pulse until the electrons have diffused a sufficient distance apart so that interaction of the separate streamers is minimal.

In a second series of tests,¹⁹ a streamer chamber was triggered on cosmic rays with pulse delays of 0.25 to 200 μ sec. Streamer-counting measurements were made on several tracks at each delay. The average number of streamers per cm of track length is plotted as a function of the delay in μ sec in Fig. 8. The streamer density is seen to increase from a few per cm to about 10/cm. This is similar to the value of about 12 ions/cm³⁹ expected for the primary ionization in neon at 1 atm, but is rather less than the total ionization of about 37 ions/cm.³⁹ The agreement with the primary ionization rather than with the total ionization is due, we believe, to the exclusion of both delta rays and bright clusters in analyzing the streamer data. In addition, some streamers may be too faint to register on film, and the probability for a single electron to form a streamer may be less than unity. The flatness of the curve in the region from 60 to 200 μ sec suggests that electron losses are not significant and that robbing by adjacent streamers is no longer important.⁴⁰

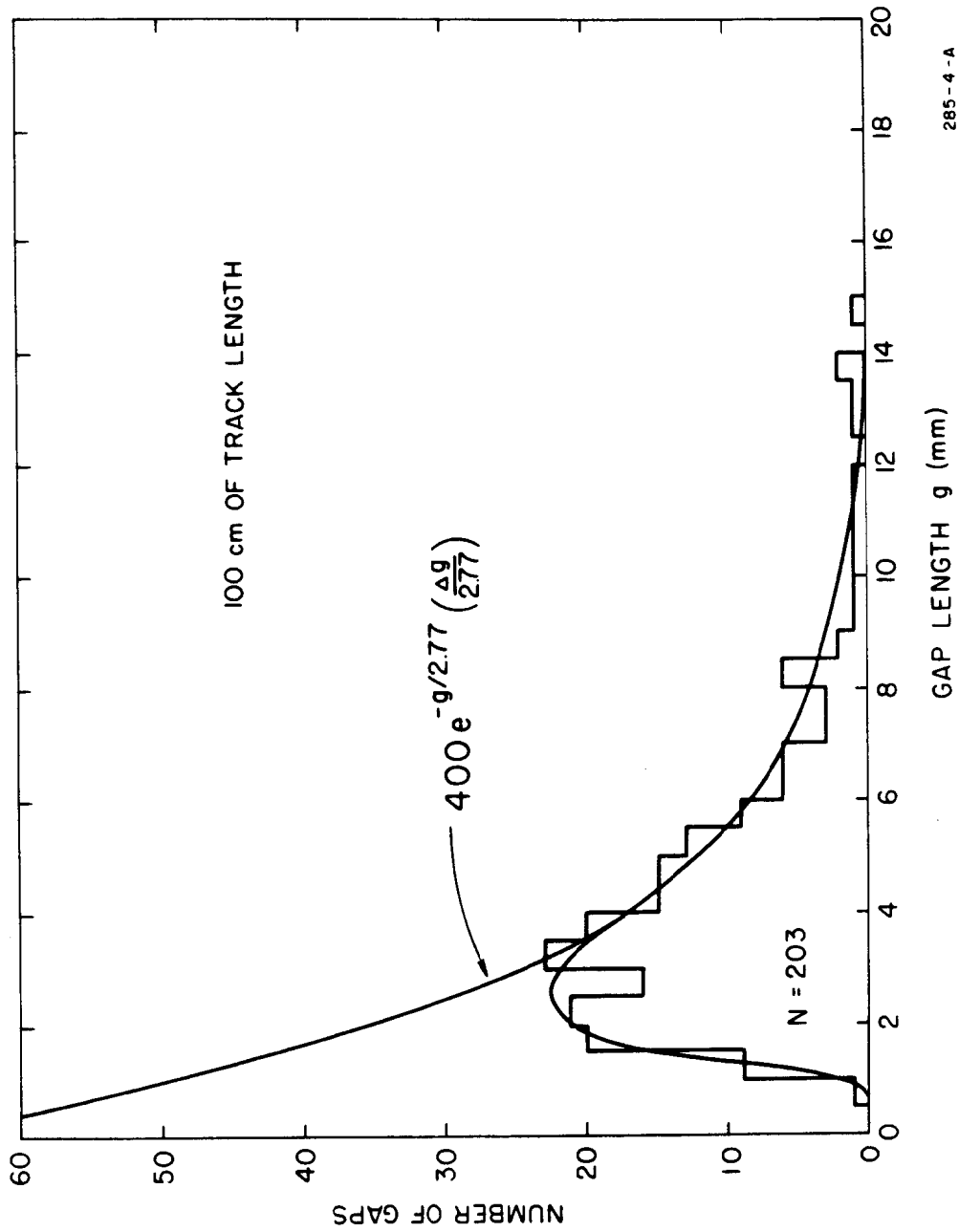


FIG. 7--Streamer gap length distribution for 0.15- μ sec delayed high voltage pulse. The expected distribution is exponential, and the cut-off at about 2.0 mm indicates that approximately 50% of the streamers are prevented from developing by a robbing action between closely spaced streamers. The mean streamer density corrected for robbing is 4.0/cm and the mean gap about 2.8 mm.

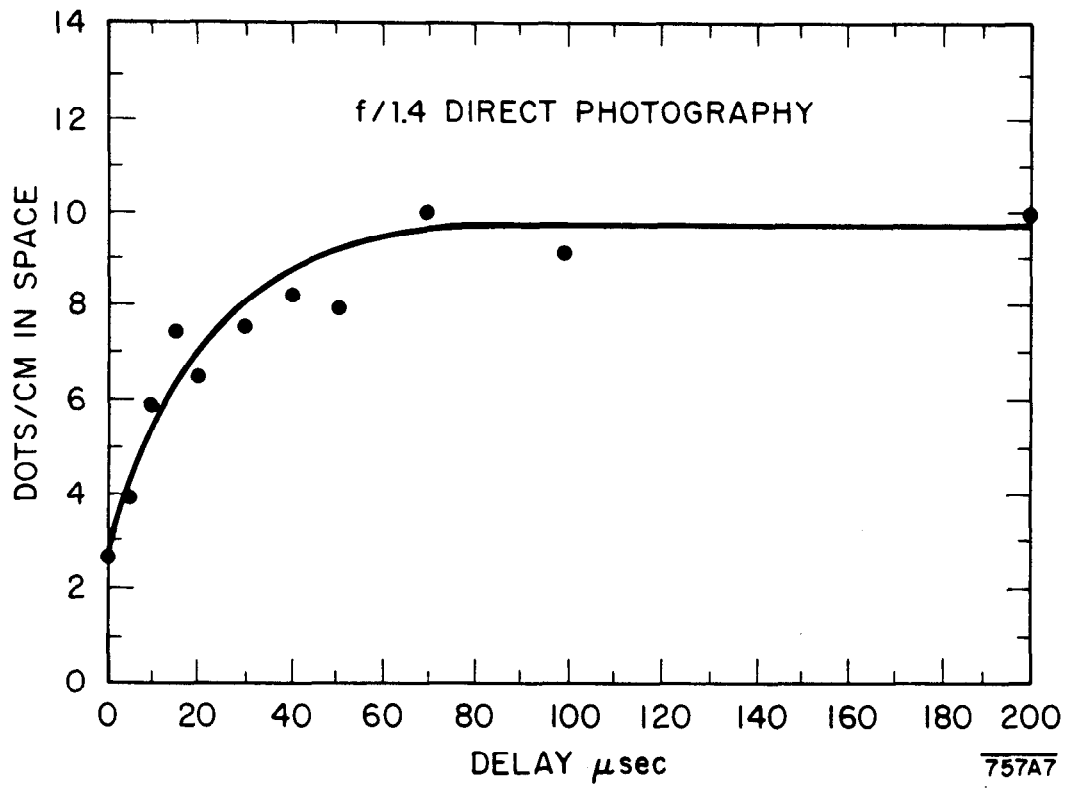


FIG. 8--Average number of streamers per cm of track length versus the pulse delay in μsec . Delta rays and bright clusters are excluded in analyzing the streamer data.

In a third series of tests,¹⁹ we attempted to eliminate the robbing effect by reducing the pressure in the chamber, i. e. , by reducing the number of ions/cm.⁴¹ The results obtained in the range from 0.03 to 1.0 atm are shown in Fig. 9. Below about 0.2 atm there is no further evidence of robbing. The image intensifier data are somewhat higher than the results for direct photography, suggesting that some faint streamers may have been lost. The image intensifier results extrapolate to about 10 streamers/cm, a value similar to that found in the studies of pulse delay.

Unless many streamers are measured at various points along a track, there is some loss of spatial accuracy when the driving pulse is delayed. Nevertheless, we consider this technique to be more promising than low pressure operation due to the considerable loss of light in the latter case. Furthermore, it is difficult to construct large chambers that can withstand a pressure differential of nearly 1 atm.*

* Robbing can also be avoided by using very early streamers or primary avalanches (F. Schneider, private communication).

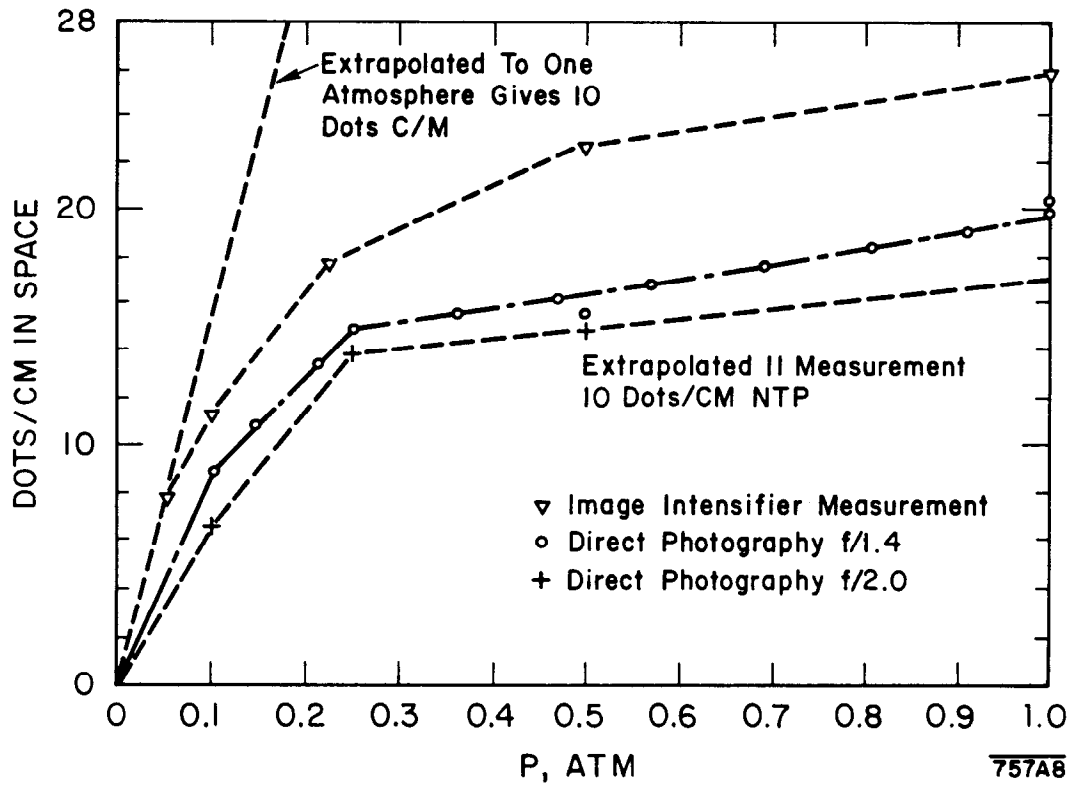


FIG. 9--Average number of streamers per cm of track length versus the chamber pressure in atm. Robbing by adjacent streamers is apparently not important below about 0.2 atm.

III. OPTICS

Perhaps the most serious problem associated with streamer chambers is the low intrinsic brightness of tracks formed in the streamer mode. We have already seen in Chapter II that one can gain in brightness without sacrificing resolution only by increasing the electric field while simultaneously decreasing the pulse duration so as to leave the streamer length unchanged. In practice it is difficult to produce either high voltages or short pulses, and it is doubly hard to achieve the two simultaneously. Ultimately the brightness is limited by one's skill and patience in high voltage pulse technology; and after a certain point one is persuaded to try, as far as possible, to solve the problem optically.

In the case of large chambers the difficulties associated with streamer brightness are intensified. Higher voltages are required simply to maintain a given electric field, and the rise time and minimum pulse duration tend to increase with the dimensions of the chamber. At the same time the most straightforward optical solution, direct photography with small f-numbers, is made less attractive by the increased depth of field. One is then tempted to try other solutions, particularly image intensifiers* which may yield a factor of 100 greater sensitivity and may thereby increase the maximum f-number allowed from about $f/2$ to $f/20$. This, in turn, would reduce the circle of confusion resulting from a finite depth of field by a factor of 10; or it would allow a chamber 10 times as deep to be photographed;

* We should mention in passing that we have also considered the use of vidicon TV cameras to digitize streamer chamber tracks, a technique used previously with conventional spark chambers. We were unable to find vidicons sensitive enough to be used with streamer chambers, and image orthicons are too unreliable and too nonlinear to be useful, although they do have the required sensitivity. A new type known as a secondary emission vidicon seems to have the required sensitivity and stability but is partially classified.

or finally, it would permit streamers to be photographed with 1/100 of the brightness.* The factor of 100 in sensitivity is based on assumptions of a 10% photocathode efficiency as compared with a 0.1% film efficiency (i. e., one seven-micron grain per 1000 photons sensitivity).

As we shall see in Section A, the depth of field problem with the two-meter chamber is not yet so serious as to require the use of image intensifiers. Demagnification and film are discussed in Sections B and C; and in the last section of this chapter, the analysis of streamer chamber data is considered with special emphasis on those features which distinguish this case from that of bubble chambers.

A. Image Intensifiers Versus Direct Photography

From the lens formula, $(1/u) + (1/v) = 1/f$, and the definition of demagnification, $M = u/v$, it is easily shown that a finite depth of field in the object space, Δu , leads to an apparent depth of field in the image space of $\Delta v = \Delta u/M^2$. The diameter d of the circle of confusion in the film plane is $\Delta v(D/v)$, where D is the diameter of the lens. In addition, we have $v = f(M + 1)/M$ giving

$$d = \Delta v(D/v) = (\Delta u/M^2)(D/f)(M/M + 1) = (\Delta u/M^2 f_{no})(M/M + 1)$$

where $f_{no} = f/D$ is the f-number. Thus, in the film plane the diameter of the circle of confusion for large M is roughly proportional to M^{-2} . Projected back to object space, the diameter of the circle of confusion is M times the diameter in the image space or $(\Delta u/M f_{no})(M/M + 1)$. The ratio of the diameter of the circle of confusion to the size of a streamer in object space therefore decreases

* There is an important qualitative difference in film and the image intensifier in that the film has a sensitivity threshold while the image intensifier will indicate a single photoelectron and has a statistical possibility of detecting a single photon. The factors used here assume equal quantum statistics, while the resolution of the image intensifier may not be statistics-limited in the range of interest.

linearly with increasing demagnification. Note that the effect of a finite depth of field in the film plane increases linearly with M so that we have decreased the sensitivity to depth of field in object space by accepting a greater sensitivity in image space. As a consequence, vacuum platens or some other method are essential for keeping the film flat.

It is useful now to distinguish two types of resolution related to the photography of streamer chambers. The first and more commonly considered is the minimum distance in space at which two separate streamers can be resolved. This is useful in determining the location of a vertex in space and also in counting gaps along a track to measure ionization. The second type of resolution, which is related to the first, is the accuracy with which the center of a streamer can be located. It is this accuracy which limits the precision with which the momentum and production angle of a track can be determined, and it is this type of resolution which interests us here.

We will now assume that the accuracy with which the center of a streamer can be located is a certain fraction of the effective streamer size S , photographed and projected to full size in space. The effective source size for direct photography is then given approximately by the square root of the sum of the squares of the following terms:

1. actual source size in space s (i. e. , the diameter of a streamer seen end-on);
2. diameter of the circle of confusion due to object depth of field;
3. diameter of the circle of confusion due to image depth of field, i. e. , to film jitter;
4. diffraction from the lens opening;
5. resolution of the lens projected into space; and
6. resolution of the film projected into space.

If these terms are independent, we have :

$$S^2 \approx s^2 + \left(\frac{\frac{\Delta u}{2}}{(M+1)f_{no}} \right)^2 + \left(\frac{M^2 \frac{\delta}{2}}{(M+1)f_{no}} \right)^2 + [(M+1)\lambda f_{no}]^2 + \left(\frac{M}{R_1} \right)^2 + \left(\frac{M}{R_2} \right)^2 \quad (15)$$

where the focus occurs at the center of Δu , and where Δu is the extreme depth of field, $M \gg 1$ is the demagnification, f_{no} is the f-number of the lens, δ is the extreme jitter in film flatness, λ is the wavelength of the light photographed, R_1 is the resolution of the lens (50% modulation), and R_2 is the resolution of the film (50% modulation).

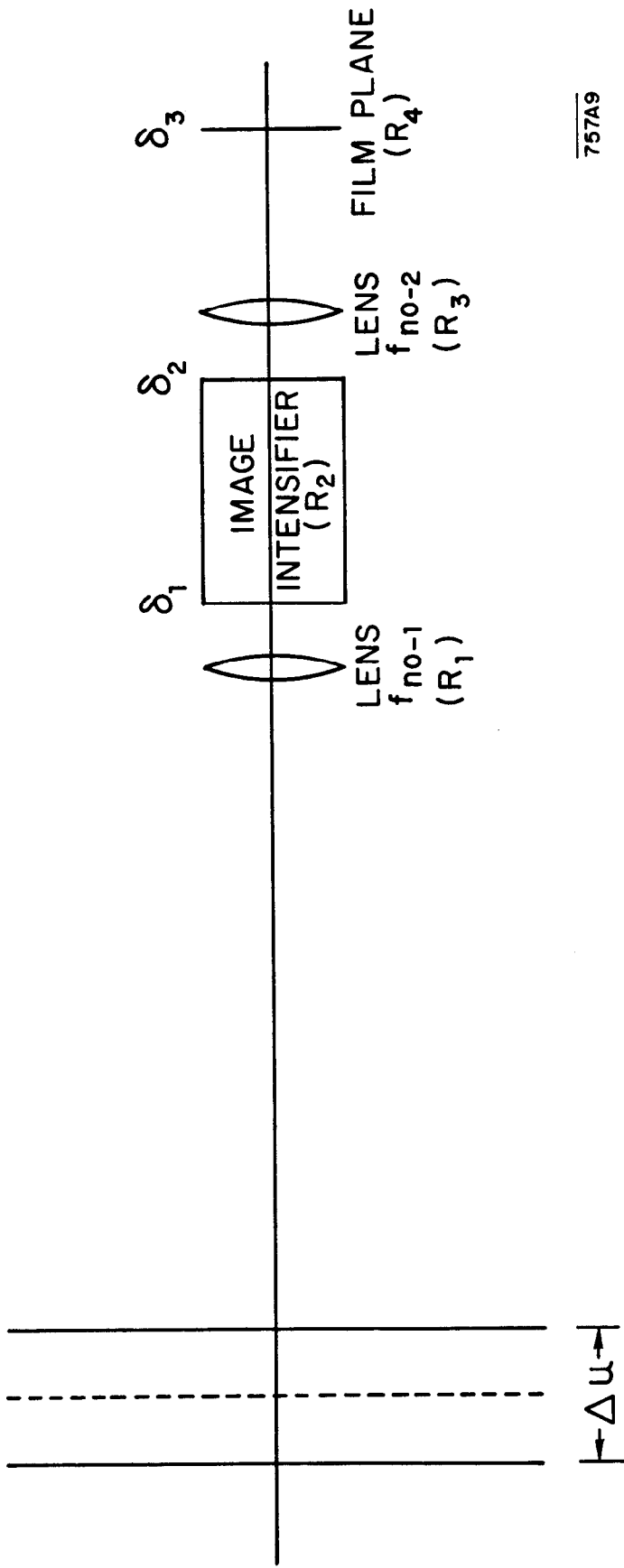
For the two-meter streamer chamber, we will take $\Delta u = 600$ mm, $M = 70$, $f_{no} = 2$, $\delta = 0.01$ mm, $\lambda = 6 \times 10^{-4}$ mm, $R_1 \approx 50$ line-pairs/mm, $R_2 \approx 70$ line-pairs/mm, and $s \approx 1$ mm. The values of M and of f_{no} are chosen approximately to minimize S^2 . The result is:

$$S^2 = (1)^2 + (2.1)^2 + (0.2)^2 + (0.1)^2 + (1.4)^2 + (1.0)^2;$$

$$S = 2.9 \text{ mm} .$$

Assuming the center of the streamer is located to $\pm S/10$, we obtain a resolution of $\sim \pm 0.3$ mm in space.

We now consider a three-stage image intensifier as shown schematically in Fig. 10. Let M_1 be the demagnification to the image intensifier, f_{no-1} be the f-number of the first lens, f_{no-2} be the f-number of the second lens, δ_1 be the non-flatness of the cathode of the image intensifier, R_1 be the resolution of the first lens, λ_1 be the wavelength of the light from the chamber, Δu be the maximum depth of field in object space, R_2 be the resolution of the image intensifier, δ_2 be the non-flatness of the output phosphor of the image intensifier, R_3 be the



757A9

FIG. 10--Layout for a three-stage image intensifier. The streamer chamber, with maximum depth of field Δu , is on the left and the film plane on the right.

resolution of the second lens, λ_2 be the wavelength of light from the image intensifier, M_2 be the demagnification of the second lens, δ_3 be the film jitter, and R_4 be the resolution of the film. The apparent source size is then given by:

$$\begin{aligned}
S^2 = s^2 &+ \left(\frac{\frac{\Delta u}{2}}{(M_1 + 1) f_{no-1}} \right)^2 + \left[(M_1 + 1) \lambda_1 f_{no-1} \right]^2 + \left(\frac{(M_1 + 1) \delta_1 / 2}{f_{no-1}} \right)^2 \\
&+ \left(\frac{M_1}{R_1} \right)^2 + \left(\frac{M_1}{R_2} \right)^2 + \left(\frac{M_1 \delta_2 / 2}{f_{no-2} (M_2 + 1)} \right)^2 + \left(\frac{M_1 M_2}{R_3} \right)^2 \\
&+ \left[\lambda_2 f_{no-2} M_1 (M_2 + 1) \right]^2 + \left(\frac{(\delta_3 / 2) M_1 M_2^2}{f_{no-2} (M_2 + 1)} \right)^2 + \left(\frac{M_1 M_2}{R_4} \right)^2 . \quad (16)
\end{aligned}$$

For the two-meter streamer chamber, we assume $s = 1$ mm, $\Delta u = 600$ mm, $M_1 = 25$, $f_{no-1} = 20$ (10 times the f-number for direct photography), $\lambda_1 = 6 \times 10^{-4}$, $\delta_1 = 0.1$ mm, $R_1 = 50$ line-pairs/mm (50% modulation), $R_2 = 15$ line-pairs/mm (50% modulation), $M_2 = 3$, $\delta_2 = 0.1$ mm, $R_3 = 50$ line-pairs/mm (50% modulation), $f_{no-2} = 2$, $\lambda_2 = 4.5 \times 10^{-4}$ mm, $\delta_3 = 0.01$ mm, and $R_4 = 100$ line-pairs/mm (assuming a slower film with better resolution). The value $M_1 = 25$ is chosen to image the two-meter chamber onto the 80-mm useful diameter of our 88-mm RCA-C70055 tube, a three-stage, magnetically focused image intensifier. The value of M_2 is chosen to make $M_1 M_2 \approx 70$ and thus to image the two-meter chamber onto double-frame, 35-mm film. (Cameras designed for 70-mm film are available, but they are not in general designed for rapid film advance, and furthermore they are expensive and hard to procure.) The result is:

$$\begin{aligned}
S^2 &= (1)^2 + (0.6)^2 + (0.31)^2 + (0.07)^2 + (0.5)^2 + (1.7)^2 + (0.16)^2 + (1.5)^2 + (0.1)^2 + (0.14)^2 + (1.5)^2; \\
S &= 3.0 \text{ mm.}
\end{aligned}$$

Again assuming that the center of the streamer is located to $\pm S/10$, we obtain for the image intensifier a resolution of $\sim \pm 0.3$ mm in space.

Looking now at the two estimates, we see that the image intensifier is not better on paper than direct photography. While the image intensifiers might be improved with better lenses, better and larger film, or better intensifiers, direct photography would also benefit from improved film as well as from brighter streamers and a correspondingly higher f-number. The type of measuring machine available is a further important consideration since, for example, a machine with a least count of 1 in 5000 will have an intrinsic limitation of about 0.4 mm for a two-meter chamber. Furthermore, we have overlooked the question of distortion, which is far more serious for the image intensifier; and we have not given any weight to the greater difficulty and expense involved in obtaining and in operating a system of far greater complexity than direct photography. Suffice it to say that when faced with this decision, we chose to use direct photography – even after we had obtained image intensifiers of the quality assumed in these estimates!

B. Selecting the Demagnification and f-Number

In the analysis given for direct photography in Section A, the implied design procedure is to fix the source size, the depth of field, and the lens and film parameters and to adjust the two remaining variables, the f-number and the demagnification, to minimize the projected source size S . Terms 3 and 4 in Eq. (15) are negligible when the vacuum platen and wide aperture lens required for direct photography are used. The important terms are those due to the source size, to the object depth of field, and to the resolution of the film and lens.

In practice, one is not really free to adjust the f-number and demagnification over a wide range. In the first place, the light intensity I on the film must be above a certain level c in order to be visible. An equation of the form

$$I = L / (16 S^2 f_{no}^2) \geq c \quad (17)$$

must be satisfied, where L is the light emitted by the source. Experience in

photographing a variety of streamer chambers over a period of three years indicates that there is sufficient light up to $f_{no} \approx 2$. Secondly, the demagnification cannot be reduced below the value which images the fiducial volume fully upon the available film size. We have already seen that for the two-meter chamber and the space available on the double-frame 35-mm film, this value is 70. Luckily, if one chooses $f_{no} = 2$ and solves Eq. (15) for the optimum demagnification, the result is $M = 77$, which is not far from the minimum value of 70.

In the design procedure just described, one tries to minimize the projected source size S because one assumes tacitly that the resolution is given by a certain fraction of S , for example, $\pm S/10$. A second point of view is possible in which the accuracy with which the center of a streamer can be located is treated as a signal-to-noise problem. From this point of view, the resolution is not a fixed fraction of S but is limited only by the sharpness of the image. The noise is due to the grain noise in the film, to nonsymmetric aberrations of the lens such as coma, and to the measuring machine and measuring girl. Noise due to fluctuations in the streamer formation cannot be reduced photographically and for this discussion will be considered unalterable.

From the signal-to-noise point of view, we should not try to minimize S^2 explicitly, but rather we should decrease the demagnification, and thus the projected size of a streamer photographed in focus, until the circle of confusion due to depth of field becomes roughly equal to the projected size of streamers in focus. At this point the light projected back to object space will be imaged over a circle whose diameter is the $\sqrt{2}$ times the diameter for streamers in focus, and the intensity will therefore decrease by a factor of 2. In this sense, the criterion proposed here

sets a practical minimum on the demagnification. From Eq. (15) we have :

$$\left(\frac{\frac{\Delta u}{2}}{(M_o + 1) f_{no}} \right)^2 = s^2 + \left(\frac{M_o^2 \frac{\delta}{2}}{(M_o + 1) f_{no}} \right)^2 + [(M_o + 1)\lambda f_{no}]^2 + \left(\frac{M_o}{R_1} \right)^2 + \left(\frac{M_o}{R_2} \right)^2 \quad (18)$$

where the symbols and origins of the various terms are discussed in the previous section. For the parameter values assumed in Section A, the minimum practical demagnification M_o is equal to about 71, a value which is again rather close to the value of 77 obtained by minimizing S^2 as well as the minimum value of 70 imposed by the film size.

We have stated that in practice one usually increases the f-number until there is barely sufficient light. This is implicit in Eq. (15) and Eq. (18) with the constraint imposed by Eq. (17). It is perhaps useful to point out more explicitly what happens if the demagnification is held constant and the f-number is decreased from 2 to a value of, let us say, 1. The intensity of the tracks in focus increases by almost a factor of 4, being less than this value because of the poorer lens resolution associated with the larger aperture. At the extremes of the chamber depth of field, the diameter of the streamers increases by almost a factor of 2 so that the intensity is essentially unchanged. This leads to the situation in which tracks near the center are overexposed and small, while those near the extremes are barely photographable and large.

We have assumed throughout this section a source size in space of $s = 1$ mm. This is appropriate for streamers viewed end-on, but is a minimum for streamers viewed at an angle. In particular, for an 18° stereo view, the projection of a finite streamer length of ΔZ is $\Delta X = \Delta Z \tan 18^\circ$; and this is in addition to the 1-mm streamer diameter. Streamer length becomes an important consideration when $\Delta Z \tan 18^\circ \sim S$, or in our case when $\Delta Z \sim S/\tan 18^\circ \sim 2.9 \text{ mm}/0.3 \sim 1 \text{ cm}$. We will use this value as an upper limit on the allowable streamer length.

C. Film, Lenses, and Measuring Machines

Various parameters have been used in comparing film : resolution, modulation transfer function, etc. In our view the key to evaluating film for use with streamer chambers is not resolution but acutance, i. e. , the "space-rise" of a sharp edge photographed on film. This is analogous to the question of frequency response versus rise time in a pulse circuit; the two views are equivalent, but the concept of rise time is more appropriate and more useful in this application.

Until recently the best available film appeared to be RAR 2475 put out by Kodak.* Figure 11 shows some of the characteristics of this film and of a newer film called Special Order 340, also from Kodak. The grain density versus time for 3 minutes, 6 minutes, 8 minutes, and 10 minutes of hand development is given for each film. After about 8 minutes there is little improvement and little that can be gained by forced development.

Figure 12 provides a comparison of hand and spray machine development. The right-hand graph is hand developed. The SO 340 film is faster than RAR 2475, and machine developing gains speed for both. Figure 13 shows the effect of forced developing on the left as compared with standard developing on the right.

Figure 14 shows a resolution chart photographed by contact exposure with RAR 2475 film on the right and SO 340 film on the left. The overall dimensions of the chart are 0.75 mm \times 0.75 mm, and the resolution of the SO 340 film is 70 line-pairs/mm. For RAR 2475 film the large box has fuzzy edges, while for the SO 340 film the edges are quite sharp. RAR 2475 exhibits hairlike arrays of grains which extend from the developed into the undeveloped region. SO 340 is free from this defect, and edges photographed with this film are straight except for grains which protrude a grain diameter of about 6 microns from the edge. SO 340 film is thus superior to RAR 2475 both in speed and in acutance.

* Eastman Kodak Company, Special Sensitized Products Sales Division, Rochester, N. Y.

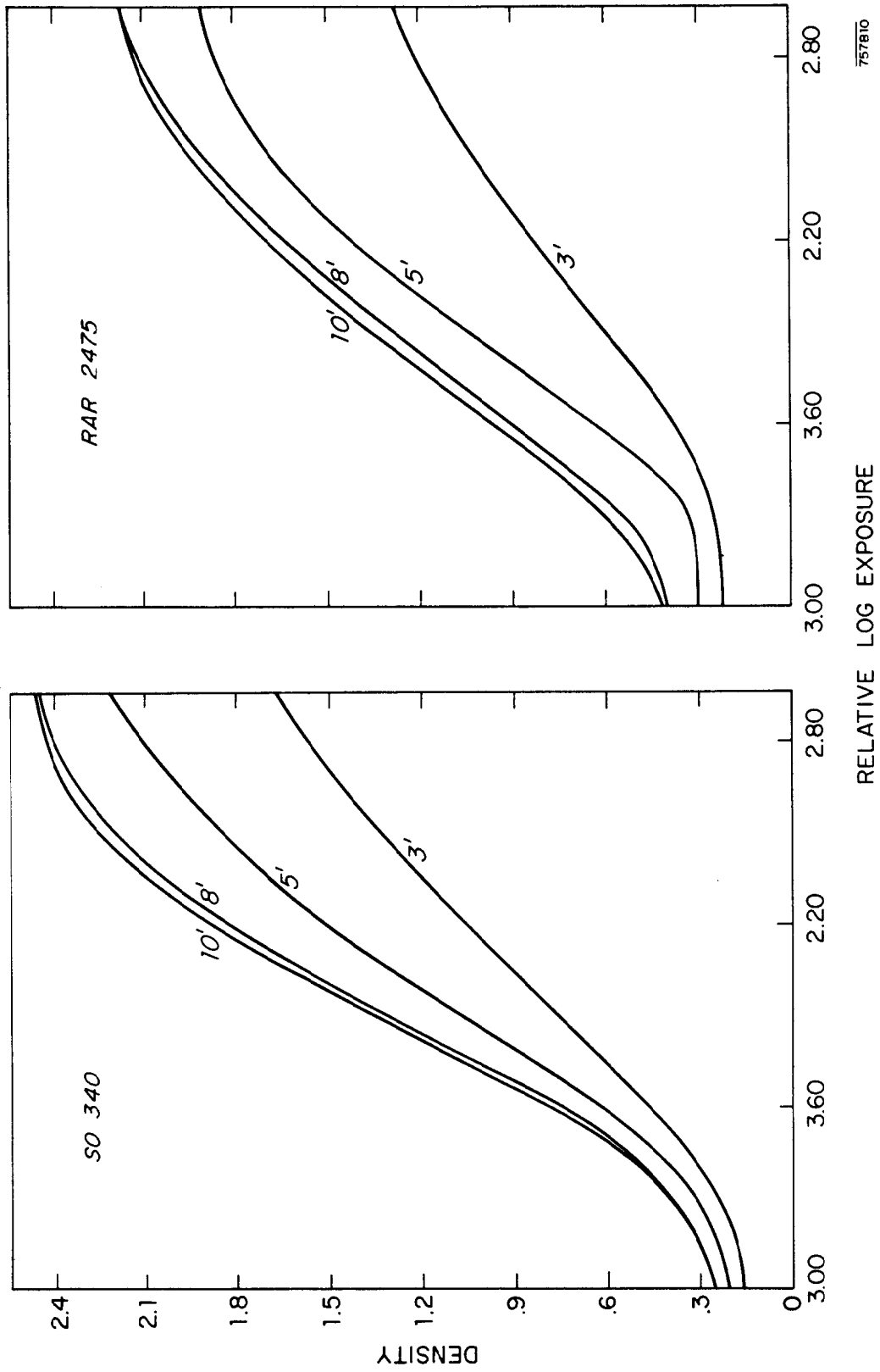


FIG. 11--Comparison of Kodak SO 340 film on the left with Kodak RAR 2475 on the right. The exposure was 1/100 sec in each case, and the development was in Nikor Reel D-19 developer at 83° F. The grain density versus time for 3 min, 6 min, 8 min, and 10 min of hand development is given for each film.

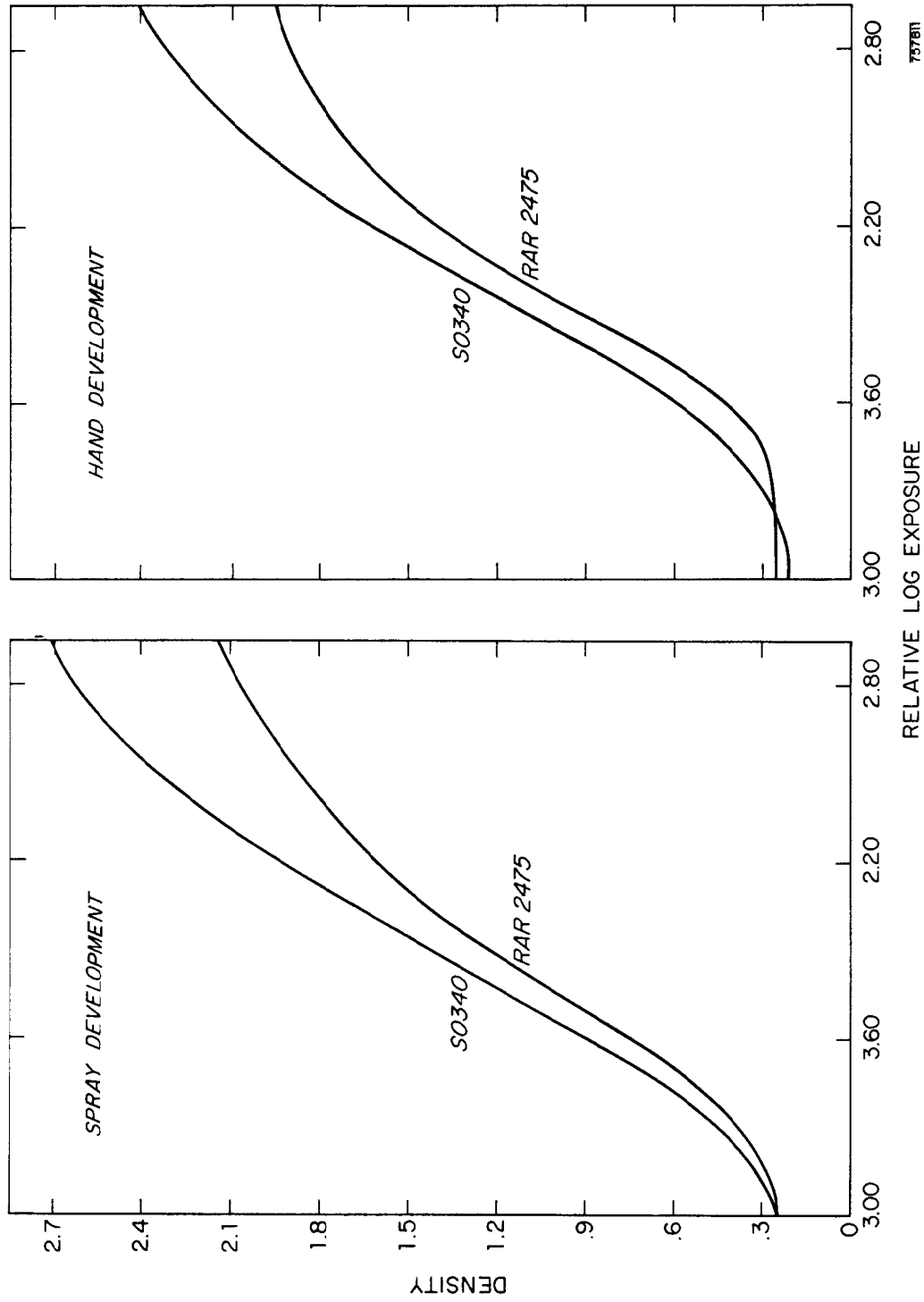


FIG. 12--Comparison of hand development on the right with spray machine development on the left. The exposure in each case was 1/100 sec with a W-21 filter, and the development was in modified Dupont x-ray developer at 83°F. The high speed spray developing machine was run at 50 ft/min.

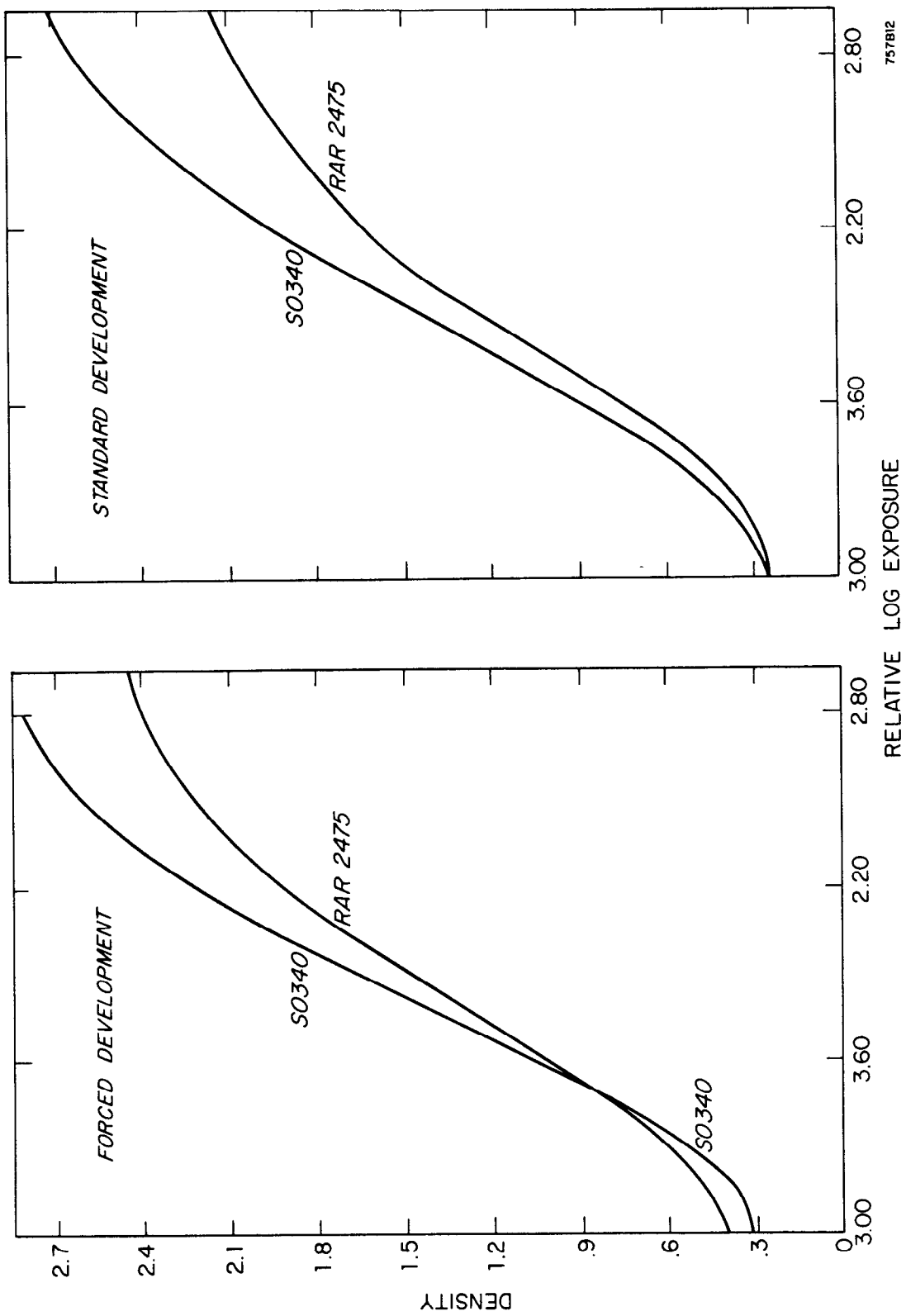


FIG. 13--Comparison of effect of forced developing (left) versus standard developing (right).

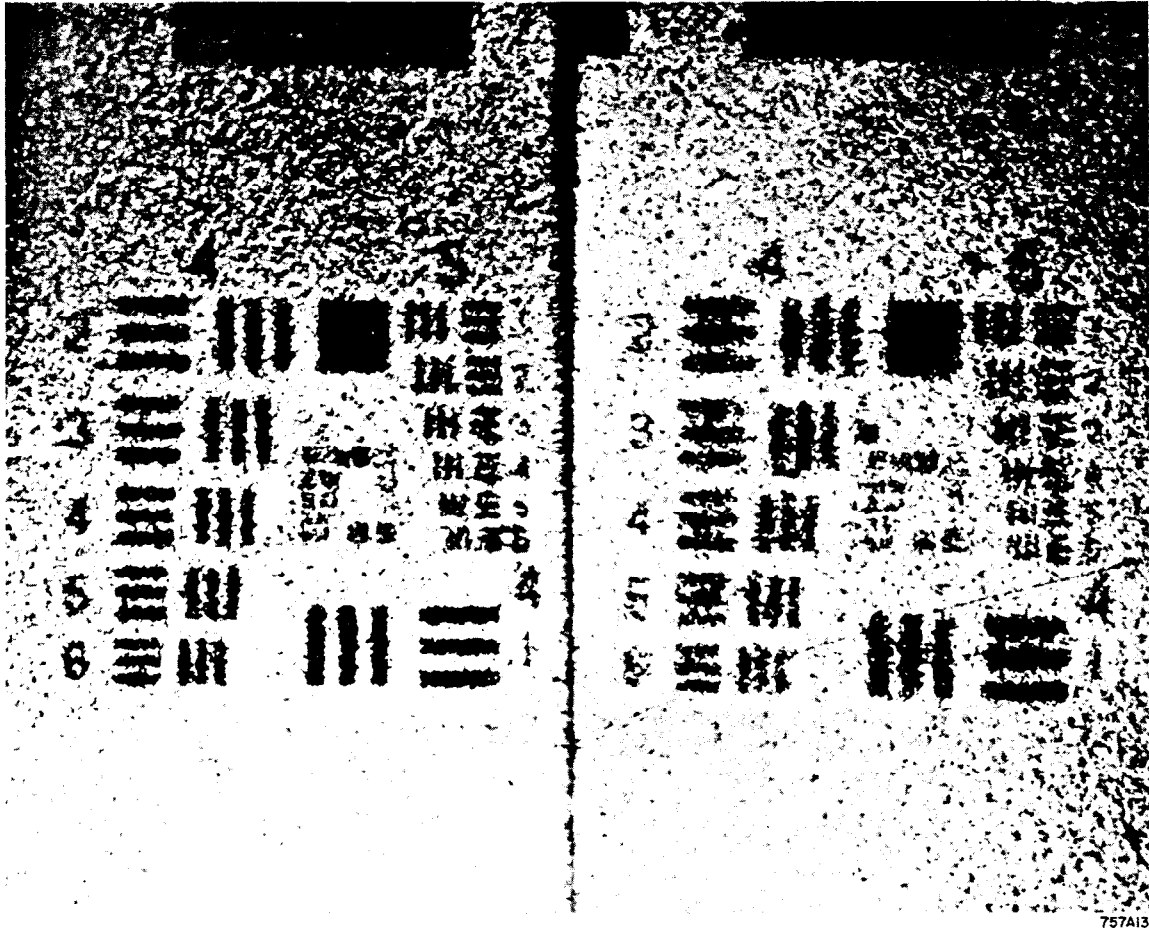


FIG. 14--Resolution chart photographed with RAR 2475 film on the right and SO 340 film on the left. For RAR 2475 film the large box has fuzzy edges, while for the SO 340 film the edges are quite sharp.

The accuracy with which the center of a small dot can be located with SO 340 film is about ± 3 microns due to grain noise. The inaccuracy of the Zeiss lenses* chosen for the two-meter chamber is also about ± 3 microns, while the SP-5-B** measuring machine with image plane digitizer adds about ± 4 microns. Errors contributed by the measuring girl are also about ± 4 microns. The square root of the sum of the squares of these numbers is ± 7 microns in the film plane. For our demagnification of 70, this corresponds to ± 500 microns $\approx \pm 0.5$ mm in space. Streamer noise contributes about ± 0.2 mm in space and does not appreciably affect the resolution. The value of ± 0.5 mm corresponds to about $\pm S/6$.

D. Data Analysis: Streamer Chambers Versus Bubble Chambers

Clearly there are many similarities and many differences in streamer and bubble chambers - even when, as in our case, they can both be adapted to the same kind of physics. The principal advantage of the streamer chamber, as with spark chambers generally, is that it can be triggered. This implies an enriched sample of events with possibly some biases for certain types. It also means that the history of tracks leaving the chamber can be studied; particle ranges can, for example, be measured and particle types identified in a variety of ways. A second point is that peripheral equipment can conveniently be used.

A significant advantage of the streamer chamber is that there is virtually no multiple Coulomb scattering in the chamber gas. Multiple scattering due to strong interactions is also negligible, and this is a more serious limitation in large hydrogen bubble chambers at energies above about 5 GeV than is multiple Coulomb scattering. The nuclear process is especially troublesome since these interactions are rather more complicated and less well understood than the electromagnetic

* We have chosen Zeiss Planar lenses on the basis of highest acutance and largest angle of view for f/1.4. Carl Zeiss Inc., 444 Fifth Ave., New York, N.Y. 10018.

** The SP-5-B measuring machine with image plane digitizer was constructed at SLAC and is based on a design from the Lawrence Radiation Laboratory, University of California, Berkeley, California.

interactions involved in multiple Coulomb scattering. Another point related to the low density of the sensitive region of the streamer chamber is that there is negligible energy loss even for heavy particles of quite low energy. Such particles, once they enter the sensitive volume, will surely be detected. On the other hand, the low interaction rate is a disadvantage in some applications; for example, the probability for converting and detecting a gamma ray is quite low unless additional material is added.

The problems associated with the determination of particle type from track ionization data have been rather thoroughly studied in the case of bubble chambers. The results of Chapter II indicate that precise ionization measurements should be possible in streamer chambers under favorable conditions. If the electrons are allowed to diffuse by adding a suitable delay in the time of arrival of the driving pulse, it may even be possible to count streamers from single electrons left by primary ionization. Track brightness provides another indication even when the driving pulse is not delayed. In all cases, however, it is essential to reproduce the pulse shape rather precisely at different points in the chamber and also from pulse to pulse. Furthermore, the apparent ionization depends upon the angle between the track and the electric field, and the quality of the ionization data and possibly the precision of the measurements of the particle trajectory deteriorate as the tracks become more and more parallel with the applied field. Thus, while the two-meter chamber may eventually provide some ionization information, we have assumed initially that it will not. Ionization is, therefore, a point in favor of bubble chambers.

Provided that the streamer chamber is operated at ambient pressure, the windows through which events are viewed can be made of thin mylar. Furthermore, the chamber gas, which is geometrically thick, has an index of refraction closely

equal to that of air. Thus, even for a very large chamber (e. g. , one meter thick) having several windows of 0.0015-inch mylar, the apparent position of a streamer differs from the actual position by less than ~ 0.05 mm in space, an amount which is negligible. This limit is valid even for stereo angles of $\sim 22^\circ$ and even if some of the refractive layers (e. g. , several of the mylar windows) are tilted up to 5° with respect to the others. In the case of a bubble chamber with a viewing window 5 cm thick, the displacement due solely to the window is already about 1 cm. This is indicative of the large optical corrections and correspondingly large errors which are made in analyzing bubble chamber data as a result of the differing indices of refraction.

The most serious disadvantage of streamer chambers from the point of view of analysis is that the best gas for tracks, namely neon, is not the most desirable target element. In the two-meter streamer chamber, a hydrogen gas target is installed within the neon volume. This consists of a thin-walled mylar tube of about 0.002-inch wall thickness, one-half inch in diameter, through which the collimated beam of photons passes. For one thing, the wall thickness puts a cut-off of about 85 MeV/c on the minimum momentum a recoil proton can have and still be detected. This is somewhat higher than for hydrogen bubble chambers, which typically go down to about 50 MeV/c, but it is not a limiting factor. Of much greater importance is the fact that the vertex of an event originating within the target is not observed. Thus the vertex is an unmeasured parameter which is determined by fitting the observed tracks. In fact, several trajectories must be fitted and reconstructed simultaneously instead of singly, as is done in the usual bubble chamber programs. This is a major consideration because it means that the programs are more complicated in this respect. This would also be true of many of the schemes proposed for automatic scanning and measuring.⁴²

As is customary in the case of bubble chambers, the axes of the three cameras used to photograph the two-meter streamer chamber are parallel. This minimizes the depth of field and simplifies the track reconstruction programs. The cameras are arranged to provide stereo angles of about 18° , while the most distant edges of the chamber in a given view are about 22° off-axis. For large f-numbers, such as those used in photographing bubble chambers, the lens distortions even at this large angle are not serious. The small f-number required in photographing streamers leads to somewhat greater distortions, and it implies that greater care must be taken in choosing lenses and in making lens corrections.

It was found by means of optical bench measurements that up to 22.4° the distortion of the four lenses purchased for use with the two-meter streamer chamber could be approximated by a radial (barrel) displacement of

$$\Delta R = -0.0084 \sin^3 \theta \quad \text{for} \quad \sin^3 \theta < 0.055 (\theta < 22.4^\circ) \quad (19a)$$

where ΔR is in meters in the focal plane. The rms variation from lens to lens is 5 microns and is equal to the error obtained on repeated measurements on one lens at 20° . The latter error indicates that the azimuthal dependence of the distortion is unimportant. Above 22.4° the following relation holds with errors from lens to lens and for repeated measurements on one lens of about 10 microns:

$$\Delta R = -0.004 \sin^3 \theta - 0.00024 \quad \text{for} \quad 0.055 < \sin^3 \theta (\theta > 22.4^\circ). \quad (19b)$$

This formula is valid up to 25° . Its accuracy above 25° is unknown.

We have seen in this section that the two-meter streamer chamber has advantages and disadvantages when compared with a hydrogen bubble chamber of comparable size. While the vertex is not seen and while the overall error in determining the center of a streamer is of order ± 0.5 mm in space, there is no multiple

scattering, and the entire track can be used in making momentum measurements. Suffice it to say that if a 10-GeV photon produces a rho meson in our chamber, the mass can be determined to about $\pm 1/2$ % assuming a spatial resolution of ± 0.5 mm. The momentum resolution for a single 10-GeV/c track is expected to be about ± 2 % with a 15 kG field.

IV. CHAMBER TECHNOLOGY

In this section we hope to answer the question: What is it we are trying to drive? We have already seen that given certain conditions--an ionizing track, a neon-helium gas mixture containing impurities of $\approx 0.5\%$, and a pulse of about 10-nsec duration and 15 - 20-kV/cm amplitude arriving within 1 μ sec after the track is made--streamers will form. Furthermore, these will be bright enough so that they can be photographed by an optical system of suitable light sensitivity. The immediate problem is then to select a practical chamber design. Since this will largely determine the requirements which must be met by the drive system, we will anticipate the following chapter on high voltage technology in an effort to minimize the difficulties which arise later in generating and in shaping suitable high voltage pulses.

A. Single versus Double Gap

In the most obvious chamber design, the high voltage appears across the single gap separating parallel high voltage and ground plates. For most applications the useful volume can be effectively doubled (or the required voltage halved) by adding a second ground plate on the opposite side of the high voltage plate from the first. The impedance (and reciprocal capacity) of the double-gap chamber is reduced by half, and correspondingly more energy is required. In practice, however, high voltage usually presents a more serious limitation than low impedance; for most applications requiring a sensitive chamber depth of 20 cm or more, the double gap is preferable.

The problem of shielding the counters and the electronics from the severe rf radiation emitted when the chamber is pulsed is more difficult for the single-gap design. Not only is the "quadrupole radiation" from the double gap subject to a much faster fall-off with distance than the "dipole radiation" from the single

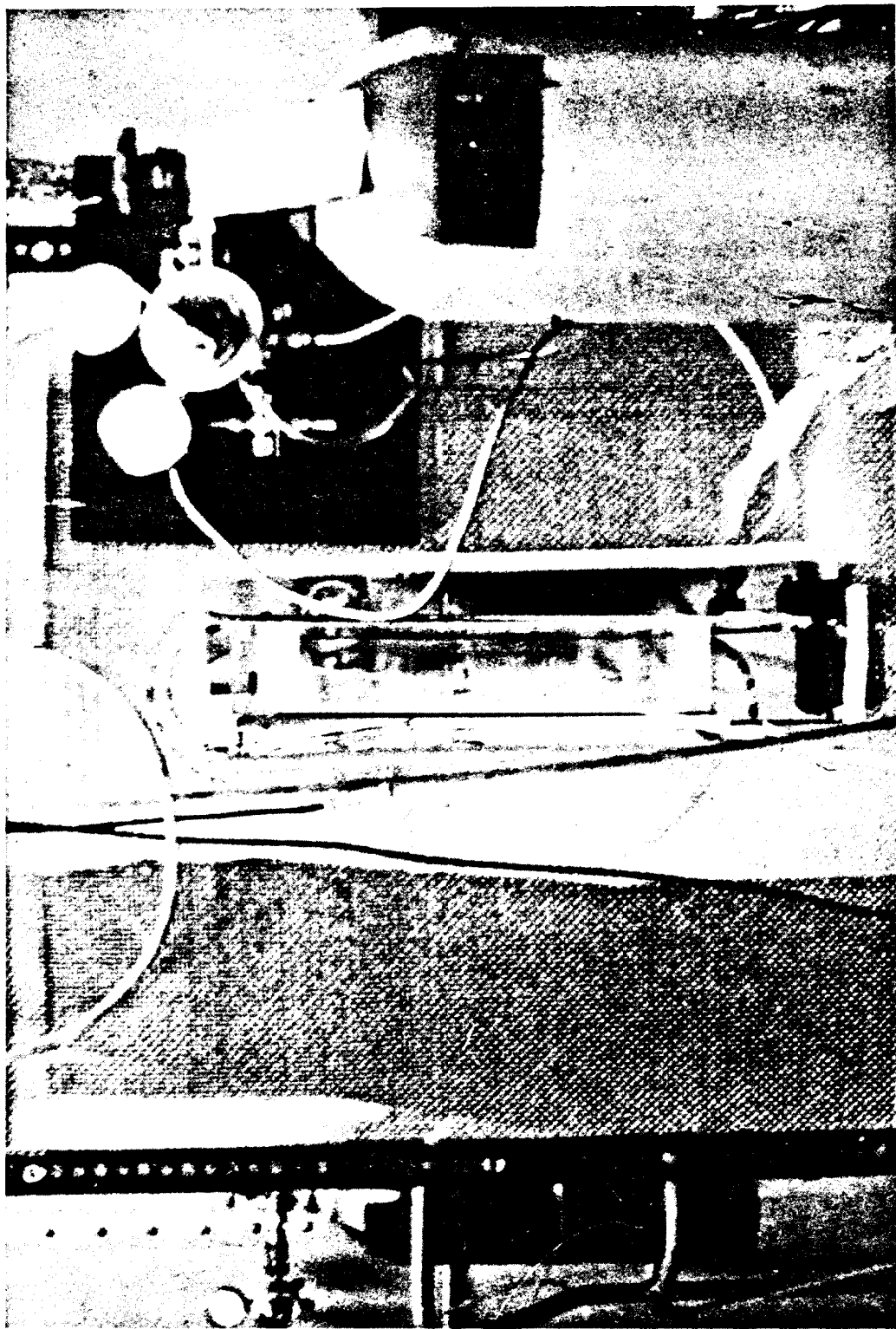
gap ($1/r^4$ versus $1/r^3$), but in addition, the ground plates in the double gap design can be extended and joined together beyond the edges of the high voltage plate, thereby resulting in a completely closed chamber. The high voltage plate in the single-gap chamber can also be enclosed, but the necessity of preventing breakdowns to an rf shield indicates an enclosure at least as large as would be required by an additional gap of the same dimensions as the first.

The necessary interruption in sensitivity caused by the central high voltage plate of the double chamber can be kept small (< 1 cm). In addition, the chamber can, if necessary, be viewed from the sides as well as from the top. This requires that the conducting sides be defined by relatively transparent conductors such as wires or screen or conducting glass, lucite, or mylar. In one sense, the double gap is preferable as a tool for doing physics: The small track displacements due to the electric field are opposite in the two gaps, and the absolute position of the original event in space can therefore be determined. Photographs of early single-gap and double-gap chambers developed at SLAC are shown in Figs. 15 and 16.

B. Small versus Large Chambers

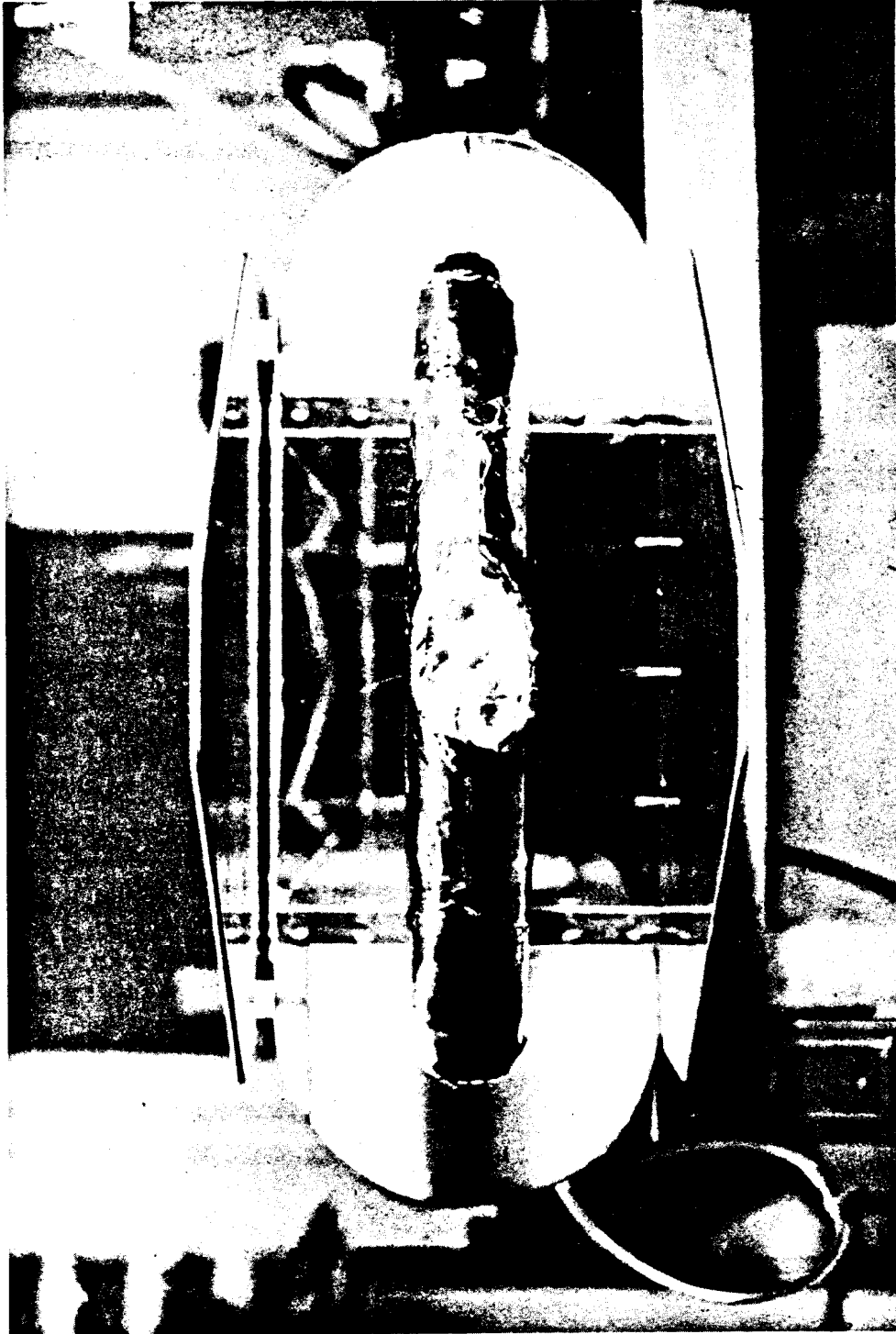
It is important to distinguish "small" chambers, which can be treated as capacitors, from "large" chambers, which act as transmission lines. Streamer chambers for which the duration of the applied pulse is long compared to the transit time from edge to edge need not be terminated in their characteristic impedance. A larger value of source impedance is then permitted, and, as discussed in the next chapter, simplified pulse generating and pulse shaping techniques are possible.

When the dimensions of the chamber are such that the transit time is comparable with or longer than the pulse width, reflections at the edges of the



757A46

FIG. 15--An early single-gap streamer chamber developed at SLAC. The dimensions of the sensitive volume are length 50 cm, width 50 cm, and gap 10 cm.



757A43

FIG. 16--An early double-gap chamber developed at SLAC. The dimensions of the sensitive volume are length 150 cm, width 45 cm, and double gap 30 cm; the view is from the input end. The outer, ground electrodes have been joined to enclose completely the central high voltage electrode.

chamber distort the pulse shape and produce tracks of non-uniform brightness. To correct this, the chamber must be terminated in such a way that the entire sensitive volume of the chamber experiences the same pulse.

C. Electrodes

When a streamer chamber is operated in a magnetic field, the electric and magnetic field lines are normally parallel. The streamers appear as small dots when viewed along the field lines perpendicular to the electrodes, and in this view the track curvature and track momentum are displayed to maximum advantage. The first condition that the electrodes must satisfy in this geometry is that they be relatively transparent.

Two classes of transparent electrodes have been used: wires including screen, and conducting films such as those commercially available on glass, lucite, and mylar. For large terminated chambers operated as transmission lines, the resistivity of the electrodes measured in ohms per square must be small compared to the characteristic impedance; otherwise, the driving pulse is severely attenuated as it propagates through the chamber. This practically precludes the sole use of conducting films in the case of large chambers, because the resistivities of available films of high transparency are typically much more than 100 ohms/square. With many wires in parallel, high-frequency resistances of < 0.1 ohm are easily obtained, but one should check that the skin depth in the wire is sufficient so that the effective resistance for fast pulses is not well above this value. The skin depth in cm is equal to $5 \times 10^3 (\rho/f)^{\frac{1}{2}}$, where ρ is the resistivity in ohm/cm and where the frequency f is roughly $1/(4\tau)$ where τ is the rise time of the driving pulse in seconds.

The only advantage of the conducting films is that the field very near the electrodes is uniform. When wires are used, the field in the region within about

one wire spacing of the electrodes is distorted; tracks formed in this region may flare or may not be visible. Furthermore, the wires cannot be in direct contact with the chamber gas, because spontaneous breakdown of the neon around the wires will occur when the chamber is pulsed. For reasonable wire diameters and wire separation (e.g., 0.25 mm and 1 cm), photographable breakdown does not occur in air. (The field near the wires is about $E_0 s/d$ where E_0 is the average field in the chamber, s is the wire separation, and d is the wire diameter.) It is, therefore, sufficient to separate the neon volume from the wires by a few wire diameters, leaving the wires themselves surrounded by air.

Another alternative is to use both wires and conducting film, with correspondingly greater light loss. To obtain a uniform field in either the single-gap or the double-gap configuration, the electrodes should extend at least one gap width beyond the boundaries of the sensitive volume. If wires are used to carry the electric field, they need cover only the sensitive volume; they can be conveniently stretched and supported on a rigid metal frame which extends the necessary one gap width beyond. In the pseudo-coaxial design used to minimize rf radiation, the enclosing side walls which join the top and bottom ground plates electrically should be everywhere at least one gap width away from the central plate to prevent breakdown. An even larger spacing is useful in maintaining as high a characteristic impedance as possible. This also reduces the chance of breakdown along the dielectric supports for the high voltage plate when these are mounted on the walls. Breakdown at the edges of the electrodes can be eliminated by attaching a "corona guard" consisting of conducting tubing having a radius of about 1/10 of the spacing between electrodes.

D. Cells and Targets

When wire electrodes are used, the boundaries of the sensitive volume must be defined near the electrodes by additional transparent windows or membranes

and not by the electrodes themselves. These membranes can be supported by the electrodes, but it is convenient in large chambers to contain the gas within independent cells which can be removed, repaired, and replaced without disturbing the electrode structure. From the wide variety of containers imaginable, we must find at least one type which satisfies all of the conditions which follow. It must be relatively impermeable to gases, highly transparent, and mechanically stable; it must not cause breakdowns or flaring when the chamber is pulsed. Furthermore, in many applications, it is important that the wall thickness measured in gm/cm² be small.

Although we have constructed cells entirely of mylar, a more convenient and durable cell design consists of a non-conducting walled frame which is inserted between the electrodes and which is sealed above and below by mylar windows stretched and glued to the edges of the frame. Mylar is preferable to glass or lucite in this application because the optical distortions which occur in these thick windows are eliminated. Laminated mylar* of 0.0015-inch thickness is available relatively free of pin holes, and the rate of diffusion of impurities into the cells through windows of this material (typically of order $\sim 10^{-4}$ cc per cm² per hour) is small. The resulting chamber cannot be pumped out, and, in fact, it must be kept at ambient pressure within a few mm of water to prevent significant outward or inward bowing of the membranes. This problem is also present with flat lucite or glass windows of any reasonable thickness when the window areas are large, and in this respect the thermally-stretched mylar is actually more convenient than lucite or glass because it does not sag appreciably under its own weight.

The mylar windows would permit a breakdown to occur in the adjacent neon if they were allowed to touch the wires. This is easily eliminated either by wrapping

*Dupont Bulletin M-3B, E. I. Dupont de Nemours & Co., Film Department, Wilmington, Delaware.

the completely sealed unit with nylon fishline of about 0.040-inch diameter or by placing 1/8-inch lucite spacer rods between the wires and mylar. The windings or spacer rods should run perpendicular to the wires in the electrodes and can be separated by spaces of about 2 inches in the first case and about 6 inches in the second, so that they do not interfere significantly with the light collection efficiency.

The choice of material for the cell walls will depend, among other things, upon whether the chamber is small or large. The most obvious material, lucite, has serious drawbacks for large chambers, not the least of which is the problem of constructing a continuous wall which is capable of supporting stretched mylar windows and which does not flex or warp under its own weight. If there are no sharp discontinuities in the walls for gas feedthroughs, etc., and if the wall thickness is not too large, lucite provides an acceptable solution. We have sometimes had difficulty, however, in pulsing large cells with thick lucite walls due to breakdowns between electrodes, particularly along the inner surface of the walls in contact with the neon. These breakdowns can cause pin-holes in the mylar at the edge of the walls, and they produce spurious sources of light within the chamber. This seems to be due to the sharp discontinuity in the dielectric constant of the lucite-gas interface and possibly to non-uniform surface resistivity. The problem is particularly severe in neon with its low breakdown voltage, but it may also occur in air.

In our more recent chambers, we have used cell walls made of polyurethane foam* and having a dielectric constant relative to air of 1.05 as compared with 2 to 3 for typical plastics. The foam walls are sealed with resin to produce lightweight, sturdy, and relatively airtight cells, in which breakdown does not

*The foam cells for the 2-meter streamer chamber were manufactured by Aquanautics, Inc., Sunnyvale, California.

occur. The foam walls, because of their low density, (0.03 gm/cm^2) are much thinner than their lucite counterparts; this is important in reducing backgrounds which originate in the chamber walls. The foam is, of course, opaque; but the large chamber is viewed in 18° stereo through the mylar windows and the upper pole face of the magnet, and this is not a problem.

Practically any nonconducting target, radiator, or absorber material can be installed within the sensitive volume of the streamer chamber, provided that it is not so large or of so high a dielectric constant that breakdown or distortions occur. For the photoproduction experiments planned at SLAC, a hydrogen gas target of small diameter will be mounted inside the upper cell. For this purpose, we have obtained mylar tubes* in 8-foot lengths having 0.002 and 0.004-inch wall thicknesses and diameters of $3/4$, $1/2$, $1/4$, and $1/8$ inch. The ends of a particular tube are mounted in the entrance and exit walls of a foam cell and are stretched under tension to achieve the necessary axial alignment. The interaction rate can be increased by raising the target pressure to 4 atm or more, as well as by increasing the photon intensity, but the former leads to an improved signal-to-background ratio for backgrounds originating in the neon or in the walls of the target and foam cells. The lucite fixtures which support the ends of the target are small enough compared to the gap spacing that breakdown does not occur. We believe that a liquid hydrogen target could be installed within the chamber to increase the interaction rate; however, the interaction rate is not a problem with the photon beam, and the small diameter gas tubes minimize the uncertainties in locating the unseen vertices. Drawings and photographs of the two-meter chamber and the foam cells are included in Chapter VI.

*The mylar tubes used for targets were manufactured by the Stone Paper Tube Co., College Park, Maryland.

E. Purifier

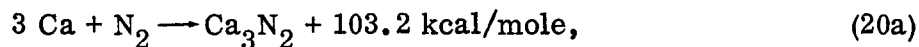
For bright streamers it is essential that the impurities in the neon-helium gas mixture be less than about 0.5%. In our case, a continuous purging of the chamber is required because of small gas leaks, because of the relatively high diffusion rate of gases through the mylar windows, and because of outgassing from the cell walls. In addition, since the cells operate essentially at atmospheric pressure (i.e., at a positive pressure of 0.1 to 0.4 cm of water), gas must be continuously added or taken out of the system to maintain the pressure equilibrium. Because of the large chamber volume and high flow rate required, we have developed a purifier which recirculates the chamber gas and which regulates the chamber gas pressure.

The major components of the original purifier are shown in Fig. 17. Initially this system was connected to the foam cells of the streamer chamber by 1-cm i.d. pipe. The flow rate of about 500 liters/hour and the input partial vacuum at the purifier of about 1.5 cm of water were controlled by the input regulating valve (1). This valve was followed by a pump of the reciprocating piston type sealed in a leak-tight box, necessary because all of the pumps we have tried leaked. A flow switch following the pump turned the pump off if there was no flow. The pump was also turned off if the vacuum prior to the pump was more than 7 cm of the water, since a larger pressure differential would cause the windows of the foam cells to collapse.

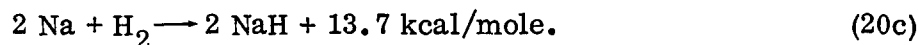
A second regulating valve (18) was used to adjust the pressure of the gas in the calcium and sodium reactors. The first solenoid valve SV-2 was open only when the pump was running, and it insured that no outside gas or air would enter the reactors. Both reactors had thermostats to control the operating temperatures, as well as thermostats to shut off the entire system if the reaction rate increased due to excessive gas contamination.

A second solenoid valve SV-1 was opened by a pressure-sensitive switch when the pressure in the foam cells became too high. A third solenoid valve SV-3 opened when the cell pressure was too low and allowed additional neon-helium gas to enter the system. The pressure of the gas leaving the purifier was controlled by another regulator and was typically about 2 cm of water above atmospheric pressure when the flow rate was 500 liters/hour. Various gas lines branched off from the purifier and were used to bypass the reactors and to permit gas sampling by a mass spectrometer either before or after the purifier.

A molecular sieve (dryer) operated at room temperature was the first active element* in the purification process, and it was expected to reduce the water content to a vapor pressure of 0.001 torr. Other impurities, principally nitrogen, oxygen, and hydrogen, were removed in the hot calcium and liquid sodium reactors. Calcium reacts with oxygen and nitrogen as follows:



Calcium does not react effectively with hydrogen, and for this we depend upon the sodium:



On the basis of gas purity data obtained with the mass spectrometer, we chose operating temperatures (near the minimum partial pressures given by the Nernst equation) of 570° C for the calcium and 150° C for the sodium reactors. The pressure was 40 psi in each reactor instead of 1 atm since the purity of the gas leaving the reactors increased with increasing pressure.

*The molecular sieve material for both the dryer and the auxiliary sieve in LN₂ is Type 13X. It consists of 1/16-inch pellets of alkali metal alumino-silicate from Union Carbide, Linde Division, New York, New York.

When the chemicals were fresh, the impurities (mostly nitrogen) leaving the purifier amounted to less than about 0.2%. After 50% of the calcium had reacted with nitrogen and oxygen, the impurities increased to about 1.0%. Streamers may still be visible with about 1.0% impurities, but bright streamers are usually obtained only with less than 0.5% nitrogen and less than 0.25% additional contaminants.

In preliminary tests, only a few percent of the impurities that entered the 1800-liter total volume of the two chamber cells could be accounted for by diffusion through the 12-meter² mylar windows. While pinholes cause at least 90% of the leakage in ordinary mylar, we had hoped that this would not be the case when laminated mylar was used. Small leaks seem to have been created during the assembly and installation of the foam cells, and there may have been some contamination from the polyurethane cell walls and from leaks in the purifier.

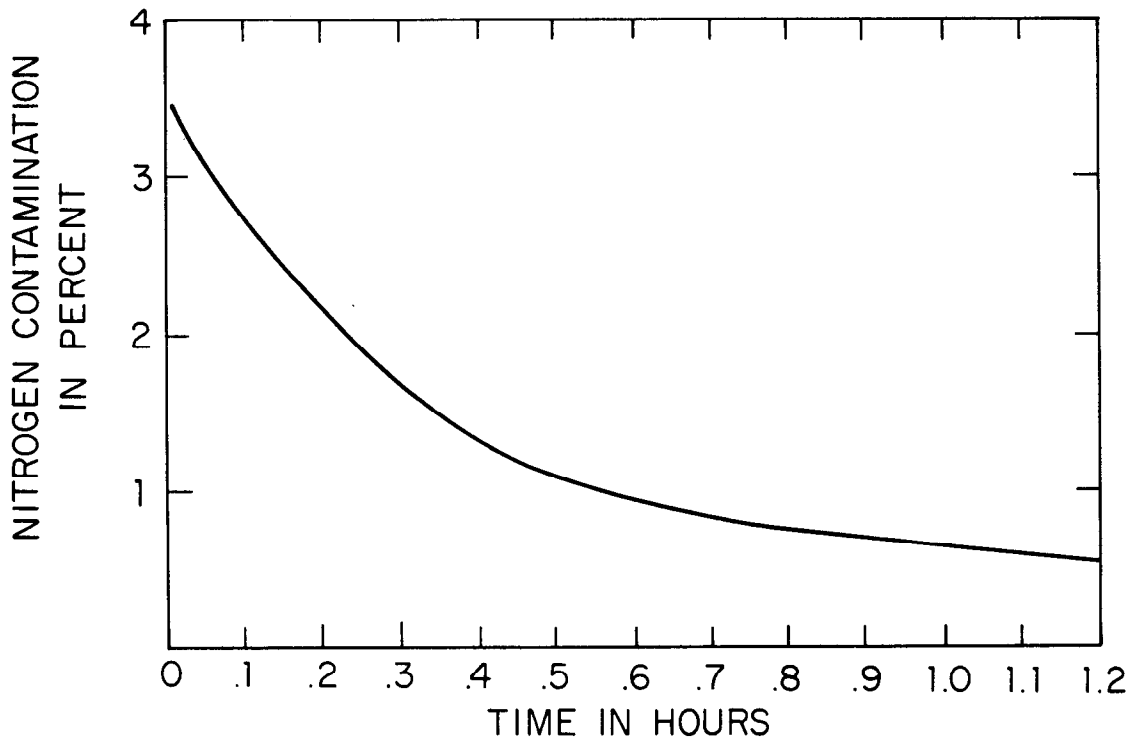
Originally the reactors contained respectively 2.5 kg calcium and 1.0 kg sodium. Due to the high leakage rate during the preliminary tests, the reactors absorbed the equivalent of about 250 liters of air after only 1000 hours of operation. This amounts to about 250 liters/1800 liters $\approx 14\%$ of the total volume of the two cells and would require that at least 4.25 volumes or 7600 liters of uncontaminated gas be flowed through the cells to maintain a purity of 0.2% ($e^{-4.25} \approx 0.2\%/14\%$). The reactants were about 50% used up after the 1000 hours, and impurities in the chamber had risen to about 1%. We have since increased the capacity of the calcium reactor to about 50 kg and have installed 2-cm i.d. gas lines to the chamber to permit an increase in flow rate from about 500 liters/hour to about 2400 liters/hour. In addition, we have repaired a number of small leaks and have constructed an auxiliary molecular sieve which can replace

the Ca and Na reactors. The sieve has a capacity of 50 kg and is submerged in liquid N_2 .

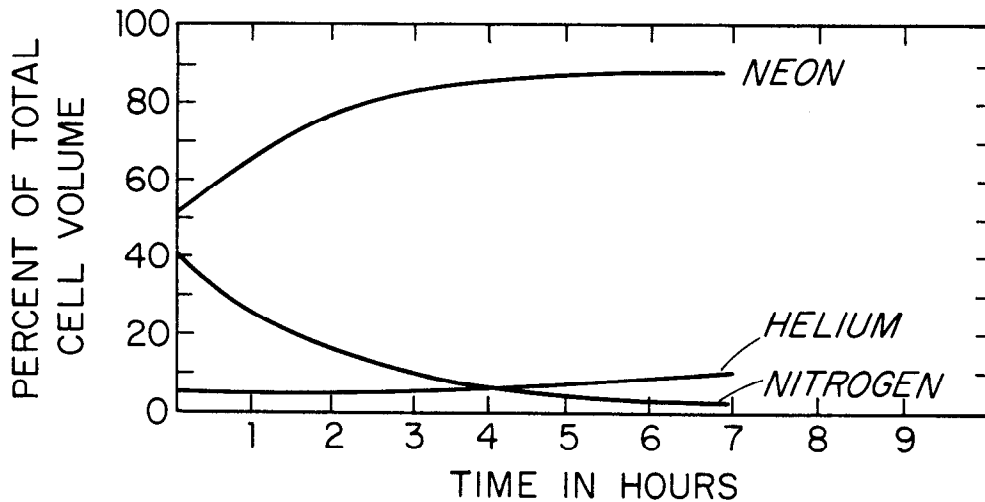
Because it is much cheaper than neon-helium, CO_2 is flowed through each cell initially to replace the air. The CO_2 is substituted for the Ne-He in Fig. 17, valve 2 is closed, and valve OUT-1 (3) is opened to air. After about 5 cell volumes of this gas have passed through each cell, the CO_2 bottle is replaced by Ne-He, and the gas leaving the cell is forced through 6-kg KOH dissolved in water. This solution, which is connected into the purifier between OUT-1 and OUT-5, absorbs the CO_2 which is immediately replaced by neon-helium. After about 4 hours at a flow rate of 2400 liters/hour/cell, the remaining gas consists of about 4% N_2 and less than 1% additional impurities. Another hour at 2400 liters/hour/cell is then required for either the auxiliary molecular sieve in LN_2 or the calcium and sodium reactors to reduce the nitrogen contamination to about 0.6%. This is illustrated in Fig. 18a.

Figure 18b indicates the effectiveness of the molecular sieve at LN_2 temperature when used with a cell which contained initially about 50% air and 50% neon-helium. The flow rate was 250 liters/hour in one 900-liter cell. About 50 kg of molecular sieve is required to remove 900 liters (one cell volume) of air. Thus the molecular sieve has about the same capacity as the 50-kg Ca and 5-kg Na reactors it replaces, and it can be baked out and can be reactivated more easily and more quickly. The principal disadvantages of the molecular sieve are the LN_2 required and the fact that H_2 is not absorbed.

Since it is perfectly feasible to maintain the desired gas purity and cell pressure simply by flowing the neon-helium mixture through the cells, one must weigh the possible economic advantages of a purifier against the effort required in development and operation. In Fig. 19, we have plotted the percent impurity



(a)



757A15

(b)

FIG. 18--Nitrogen contamination as a function of time. In (a) the flow rate was 2400 liters/hour through a single 900-liter foam cell with the Ca-Na reactors providing the active unit. In (b) the 50-kg molecular sieve at LN₂ temperature was used to purify a cell containing initially about 50% air (40% nitrogen). The flow rate was 250 liters/hour into one 900-liter cell.

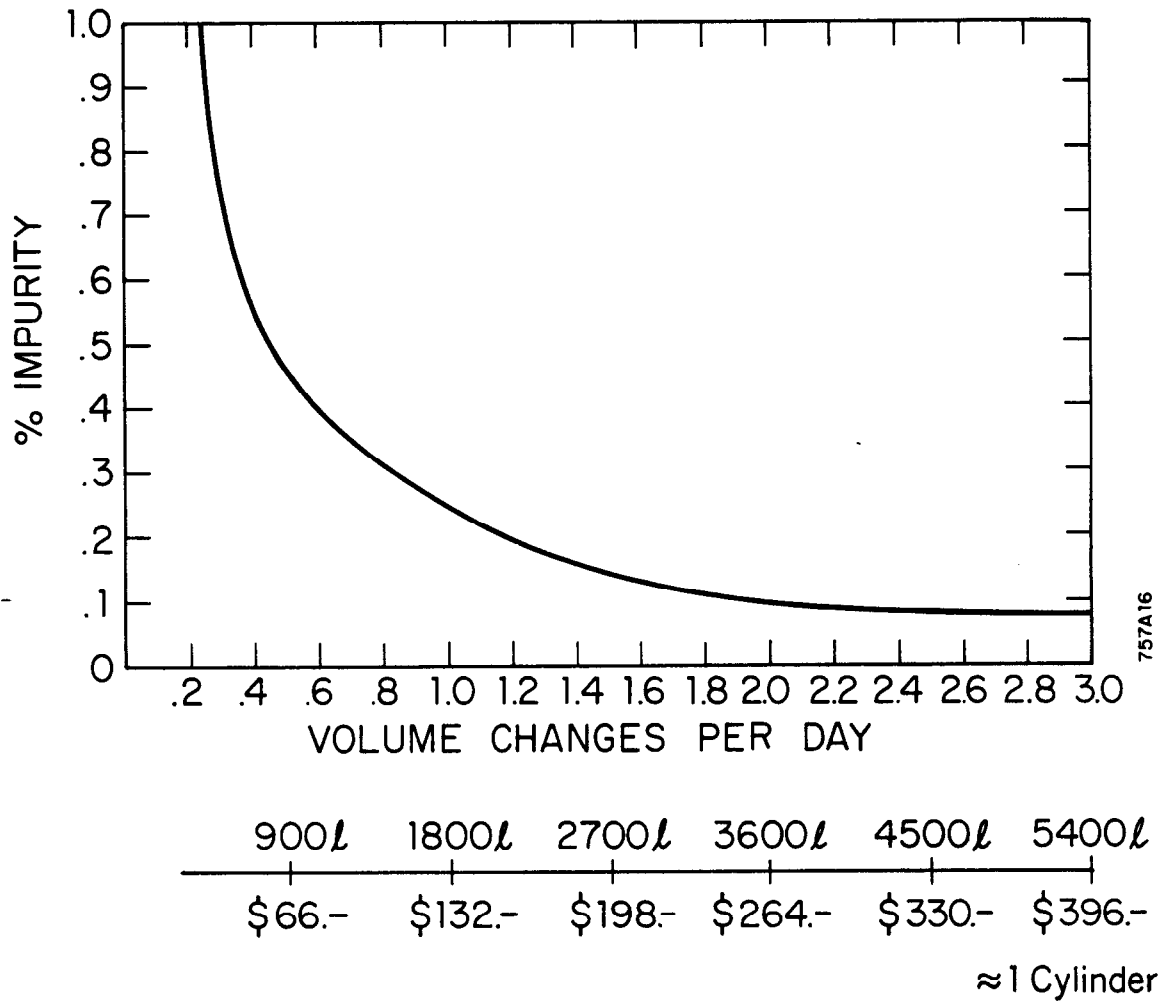


FIG. 19--Gas impurities versus the equilibrium flow rate, versus the neon volume flowed per day, and versus the neon cost. A leak rate of 0.01% per hour into two 900-liter foam cells is assumed here and is similar to the actual leak rates observed during tests, including a preliminary run in the photon beam.

in the 1800-liter total cell volume as a function of the equilibrium flow rate. We have assumed a leak rate for impurities of 0.01% per hour, which is similar to the rates observed in preliminary tests and also during the check-out runs in the photon beam. The cost of operating the purifier with the molecular sieve is about \$40 per day, not counting development and construction. The operating cost with the Ca-Na reactors is slightly less. If this sum were spent for neon-helium to be flowed through the cells, the impurities could be maintained at less than 0.6%, as indicated in Fig. 19. The purifier becomes economically feasible in our case only when we require that impurities be somewhat less than this value. The break-even point depends upon such things as the developmental costs, the number of hours of operation per year, etc. In retrospect, we can say that it is economical to operate the existing purifier and that it would be possible to pay off the construction costs of a similar purifier with about three months of continuous operation. It remains to be seen whether the developmental costs can be justified during the next several years.

V. HIGH VOLTAGE TECHNOLOGY

A. Introduction

As in the chapter on streamer theory and experiment, we are considering here a subject about which many articles and even entire books have been written.⁴³ Some readers may find this summary too brief, while others may find it too long and too detailed. We have tried, however, to produce something that will be helpful to other groups who may wish to build streamer chambers and who enter this field with as little initial experience as we had. As a consequence, the discussion is rather detailed where it pertains to problems we have run into and to solutions we ourselves have tried in the course of developing the two-meter streamer chamber. The discussion is brief in the cases of several alternate solutions which are, nevertheless, quite promising. The subject matter on the high voltage properties of materials and on high voltage switch technology is quite important, but we have put it into Appendix A and Appendix B rather than interrupt the continuity of the discussion with long digressions. Similarly, the material on autotransformers is interesting for its own sake, but it is not really relevant here because we have chosen to use Marx generators instead. Autotransformers are, therefore, considered in Appendix C.

In discussing streamer chambers, we have separated the complete system into two major parts: the high voltage pulse source of this chapter and the actual streamer chamber of Chapter IV. A further separation of the pulse source into pulse generating and pulse shaping elements is of more than academic interest, at least in the case of large chambers. The point is that the internal impedance of most generators increases with increasing voltage, a fact which is inconsistent with the required fast rise time and short pulse duration. An intermediate pulse shaping network frees the generator from restrictions of this kind and permits a

straightforward extrapolation of small generators to higher voltages. It is important to note, however, that since the voltage appears across the generator and charging elements of the pulse shaping network for a much longer time than it appears across the plates of the chamber, special care must be taken to prevent breakdown in these charging elements. The complete three-element system is shown in block form in Fig. 20a.

Our central problem is to produce a high voltage pulse of 15 - 20-kV/cm amplitude and of about 10-nsec duration and to apply this pulse to the electrodes of a streamer chamber with a delay of less than 1 μ sec. For the two-meter chamber with two 30-cm gaps between three electrodes, the required voltage is 450 - 600 kV across 23 ohms and the required energy is about 100 joules.

In designing a drive system, it is important to determine in the beginning whether the load, shown schematically in Fig. 20b, is resistive or capacitive. Electrically the chamber is equivalent to two rectangular conducting electrodes each having dimensions in meters of length L and width W separated by a gap G. If the condition $2L < \tau c$ is satisfied, where τ is the pulse duration and c the velocity of light, then the chamber is a pure capacity whose value is given by

$$C \approx \frac{8.85}{\sqrt{\epsilon_{\text{rel}}}} \frac{WL}{G} \text{ pF} . \quad (21)$$

If $2L \gtrsim \tau c$, the two plates behave as a transmission line whose characteristic impedance is approximately

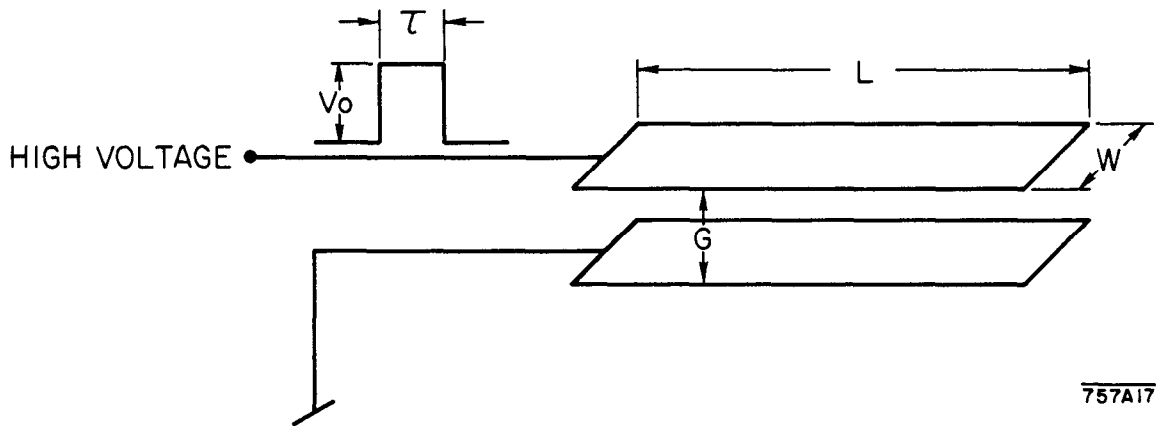
$$Z \approx \frac{377}{\sqrt{\epsilon_{\text{rel}}}} \frac{G}{G+W} \text{ ohms} . \quad (22)$$

This formula is somewhat different from that found in most books in that there is a factor G in the denominator to take into account edge effects.

We should mention here that the Handbook of Chemistry and Physics⁴⁴ gives a number of formulae (the so-called radio formulae) for the capacitance, inductance,



a.



b.

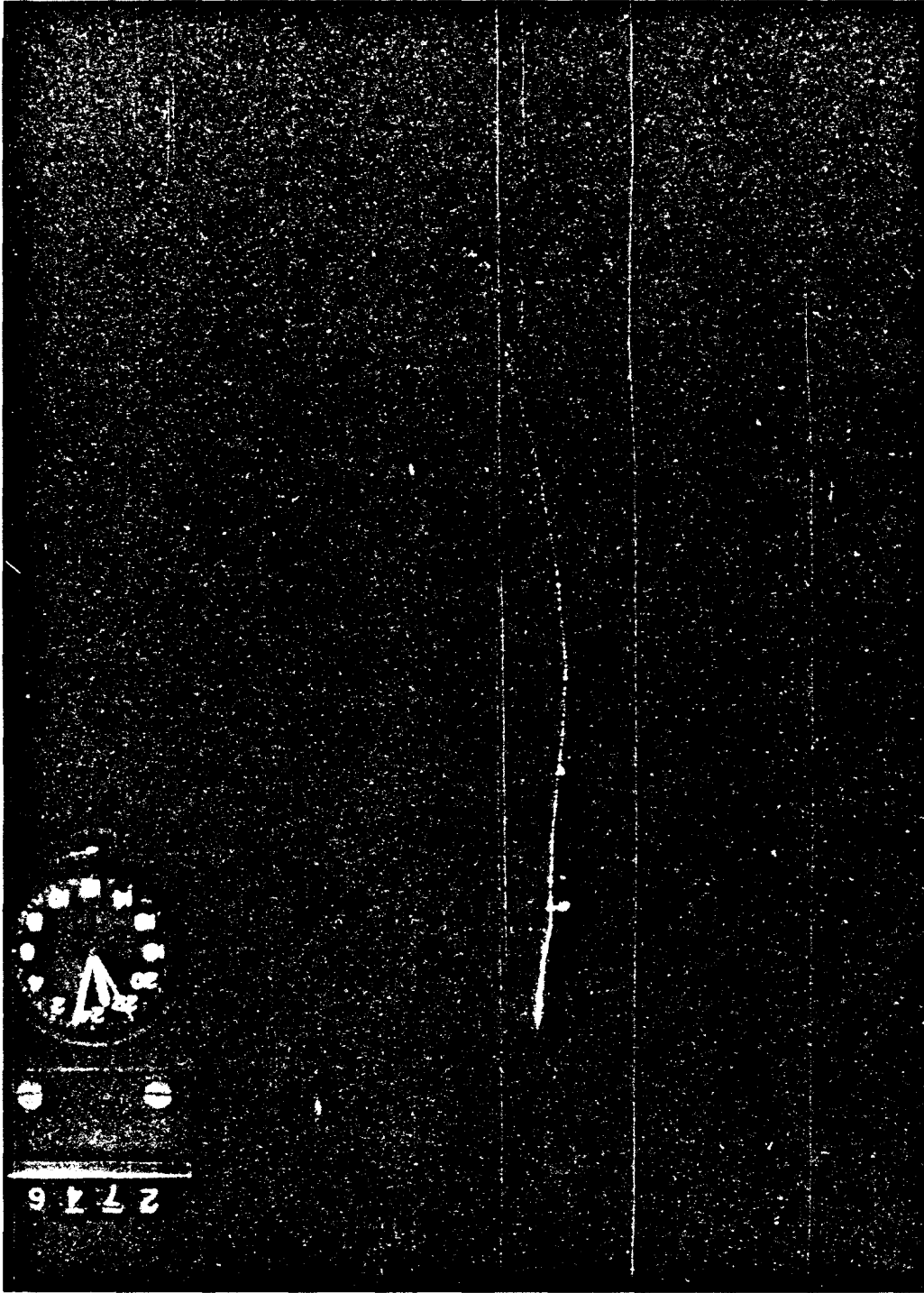
757A17

FIG. 20--Block diagram illustrating the principal elements of the streamer chamber system (a) and a chamber layout to be considered either as a capacitor or as a transmission line (b).

and impedance of various configurations. In addition, there is a convenient and widely used technique for determining the characteristic impedance of a transmission line of arbitrary cross section. One simply images the electrode cross section with highly conducting paint upon paper of somewhat lower conductivity. Impedances between electrodes are then measured with an ohmmeter relative to a standard impedance, the imaged cross section of a 60-ohm cable (i.e., a cable for which the ratio of the radii of outer and inner conductors is $r_1/r_2 = 2.718$). There are, of course, variations such as the use of metallic electrodes immersed in conducting solutions. We have found such techniques extremely helpful, particularly in matching Blumlein and streamer chamber impedances.

Equation (22) also applies if $2L \ll \tau c$. The pulse in this case reaches the far end of the chamber, which is not terminated, and it reflects back with the same polarity before the original pulse ends. The pulse seen at the input of the chamber resembles a staircase in which the steps are separated by $2L/c$, twice the propagation time for the chamber. The rising "staircase function" is superimposed on the non-zero rise time of the applied pulse, and its effect is to increase the final rise time on the chamber. If $2L \gtrsim \tau c$ (e.g., $L = 4.0$ meters and $\tau = 10$ nsec) and if the chamber is not terminated in its characteristic impedance, then the input will see the superposition of the original and the reflected pulse, which is delayed, while the far end will see twice the original pulse height. The effect on a streamer track of a terminating impedance 35% lower than the characteristic impedance is shown in Fig. 21.

For a 50 to 80-cm-long chamber, i.e., for a size in between a capacitive and a resistive load, the light uniformity and streamer brightness as compared to an unterminated chamber, can be improved by terminating the chamber in an impedance several times the characteristic value. In this mode of operation, the energy



757A47

FIG. 21 -- Streamer track photograph with the 2-meter chamber terminated by an impedance 35% lower than the characteristic value. The ionizing particle was incident from the input end of the chamber where the track is brightest.

required to drive the chamber is somewhat greater than for an open circuit and somewhat less than for a matched impedance.

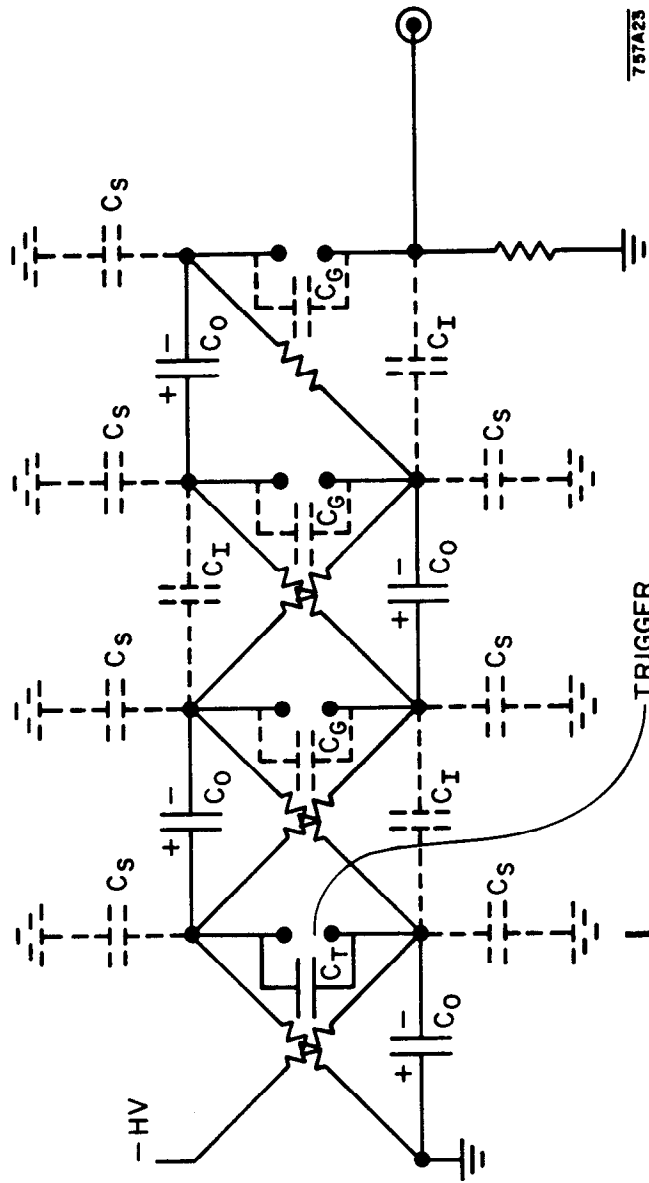
By this point in the discussion, the performance specifications for the pulse generator and pulse shaping network should be clear. In the next two sections of this chapter, we consider various types of generators and pulse shaping networks and give our reasons for choosing a Marx generator and Blumlein for the final system. The final section of this chapter is devoted to high voltage probes and pulse monitoring techniques.

B. High Voltage Generators

It is possible, of course, to charge a pulse shaping network such as a Blumlein or a capacitor with series and shorting gaps simply by connecting it to a dc high voltage supply. In practice, dc supplies in the megavolt range exist but are quite large and relatively expensive. Furthermore, several other methods are available for generating high voltage pulses which begin with dc voltages at a modest level (e. g. , ± 50 kV) and which can, therefore, make use of commercially available dc supplies.

A special high power dc supply operating at ± 50 kV was developed at SLAC to permit rapid generator charging and thus a high repetition rate for the two-meter streamer chamber. This supply, described in the final chapter, is still of quite modest size and cost compared to a megavolt dc generator.

A Marx generator^{43,45} consists essentially of a bank of capacitor stages charged in parallel and discharged in series by means of spark gaps. A single-polarity, four-stage, four-gap Marx generator is shown in Fig. 22. In this example, the output is across a final isolating gap, and the load is grounded during the charging period. If the charging voltage is V_{in} across N stages, then the output voltage, to first approximation, is $V_{out} = NV_{in}$.



757A23

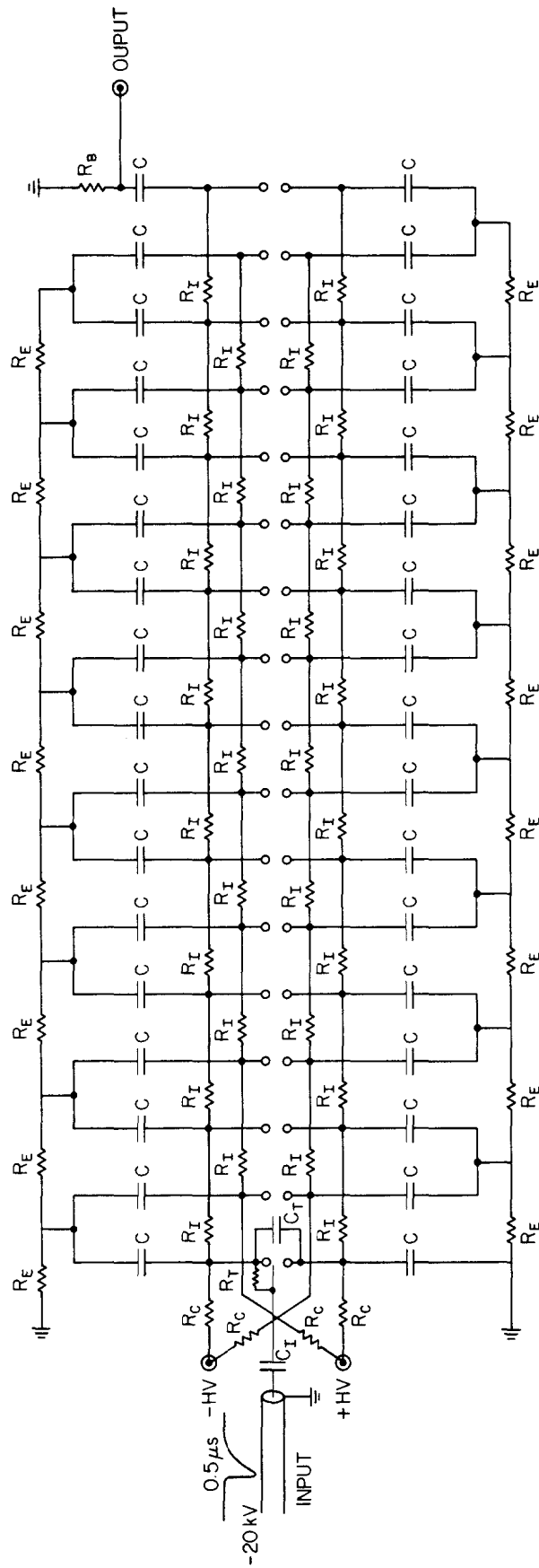
FIG. 22--A four-stage, single-polarity Marx generator. The spark gap capacity C_G , the stray capacity to ground C_S , and the interelectrode capacity C_I are shown with dashed lines and should satisfy the condition $C_G \ll C_S$, C_I for reliable triggering. The trigger capacitor C_T is added to the trigger gap to increase the energy discharged by this gap and thus to increase the light output.

The operation and the triggering of Marx generators are discussed in detail in Refs. 43, 45, and 46. We should mention, however, that the basic process, in which the first spark gap is triggered externally and in which successive gaps break down because of the subsequent and increasing overvoltage, is influenced strongly by the stray capacity across the gaps C_G , the interelectrode capacity C_I , and the stray capacity to ground C_S . In particular, for reliable triggering, C_I and C_S should be large compared to C_G so that the overvoltage does, in fact, appear across the next gap. The charging resistors, if small, also aid in triggering. A special trigger capacitor C_T placed across the first gap increases the light output from this gap and reduces the time jitter. The triggering range can also be enhanced with suitable gas mixtures, e.g., 90% CO_2 - 10% A. As usual, the breakdown voltage can be adjusted by changing the pressure in the gaps or by changing the electrode spacing.

A circuit diagram of the double-polarity, 34-stage, 17-gap Marx generator designed for the two-meter streamer chamber is shown in Fig. 23. The use of both positive and negative charging voltages reduces by a factor of two the number of spark gaps or the maximum dc voltage required, and it simplifies the design. The first gap is triggered by a third electrode as indicated.

A simplified equivalent circuit for the Marx generator is shown in Fig. 24. C_o is the capacity of each stage, N is the number of stages, L and R are the internal inductance and resistance of the generator, and C_p is the parasitic capacity from the output to ground. The switch S_M represents the last spark gap.

While the nominal value of C_o is probably known, the capacity in the case of barium titanate is a function of the charging voltage V_{in} as well as of the age. With zero charging voltage, the capacitance of the individual components can be measured with standard laboratory instruments. The variation with voltage can



R_C = CHARGING RESISTOR = 30 k, 400 W.

R_T = TRIGGER RESISTOR = 2 k, 4 W.

R_E = EXTERNAL RESISTOR = 5 k, 30 W.

R_I = INTERNAL RESISTOR = 3 k, 30 W.

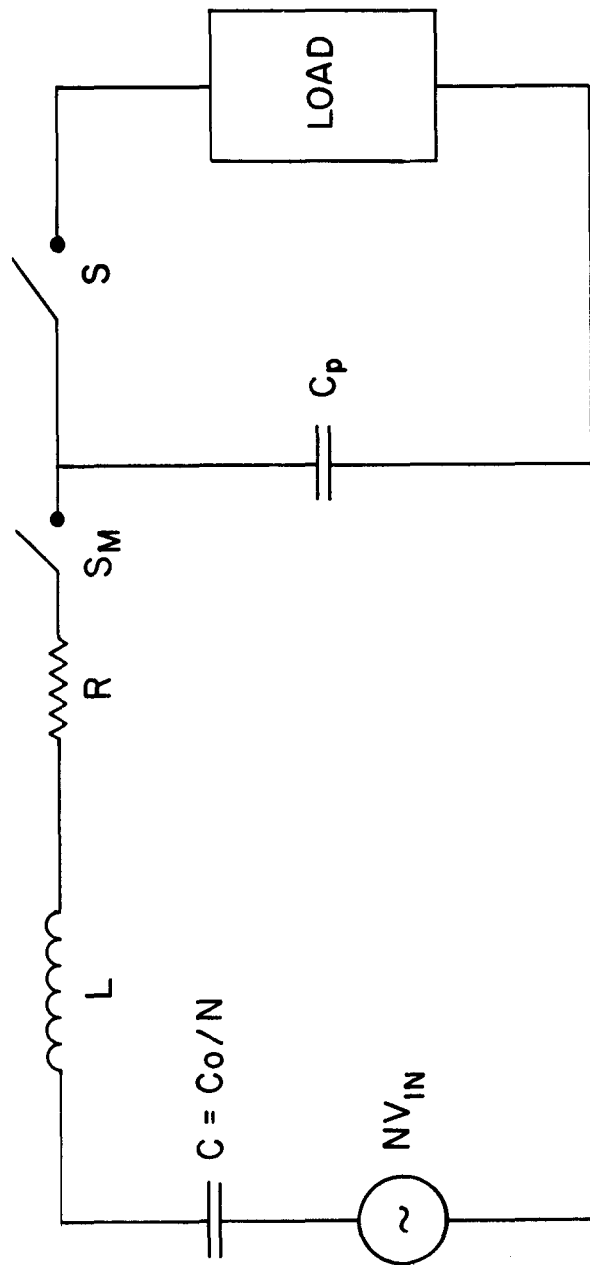
R_B = BLEEDER RESISTOR = 4 k, 1.2 kW.

C_I = INPUT CAPACITOR = 600 pf, 120 kV.

C = CAPACITY/STAGE = 34,000 pf, 40 kV.

C_T = LIGHT PRODUCING CAPACITOR = 1000 pf, 80 kV.

FIG. 23--Circuit diagram for the 17-gap, 34-stage Marx generator used to drive the 2-meter streamer chamber. A photograph of this generator is shown in Fig. 38.



757A31

FIG. 24--Marx generator equivalent circuit. The procedures by which one can determine the capacitance and the internal inductance and resistance of a Marx generator are described in the text.

then be determined by measuring the characteristic frequency across an arbitrary inductance with various bias voltages across the capacitor. An arrangement which we have used is shown in Fig. 25a, and a typical voltage dependence for our barium titanate capacitors is shown in Fig. 25b for a 40-kV capacitor.

By shorting the output with $R_{load} \sim 0$ ohms and by measuring the waveform across R_{load} , the internal resistance and inductance of the Marx generator can be determined. The output is essentially a ringing pulse with exponentially decaying amplitude. From the ringing frequency f cycles/sec and the known capacitance $C = C_0/N$, the inductance L can easily be calculated:

$$L = 1/C\omega^2 \quad (23a)$$

where $\omega = 2\pi f$. The Q-value for the Marx generator is defined as

$$Q = \pi \tau / T \quad (23b)$$

where $T = 1/f$ is the ringing period and τ is the exponential decay constant in the ringing amplitude,

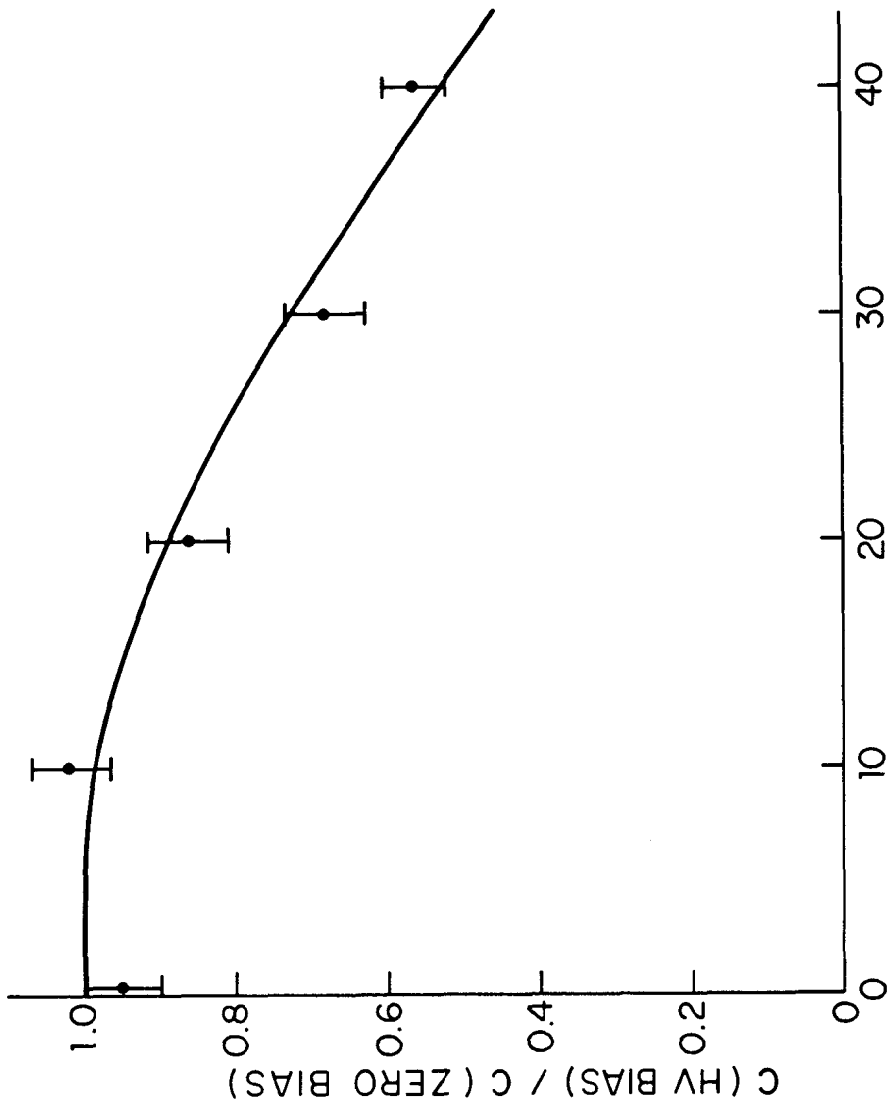
$$A = A_0 e^{-t/\tau} . \quad (23c)$$

The internal resistance is then given by

$$R = \sqrt{\frac{L}{C}} / Q . \quad (23d)$$

The parameter values for the 34-stage, 17-gap Marx generator of Fig. 23 are: $C = 34,000 \text{ pF}/34 \sim 1000 \text{ pF}$, $L = 3 \mu\text{H}$, and $R < 0.3 \text{ ohm}$. At a charging voltage of 40 kV/stage, this generator is capable of storing 800 joules and of producing an output pulse in excess of 1.3 MV.

J. C. Martin and I. Smith⁴⁷ have developed an elegant and quite inexpensive air-core autotransformer for generating high voltage pulses. The autotransformer is driven by a high voltage capacitor which is switched across the primary by means of a spark gap. These devices, described in detail in Appendix C, are physically



HV BIAS IN kV

(b.)

(a.)

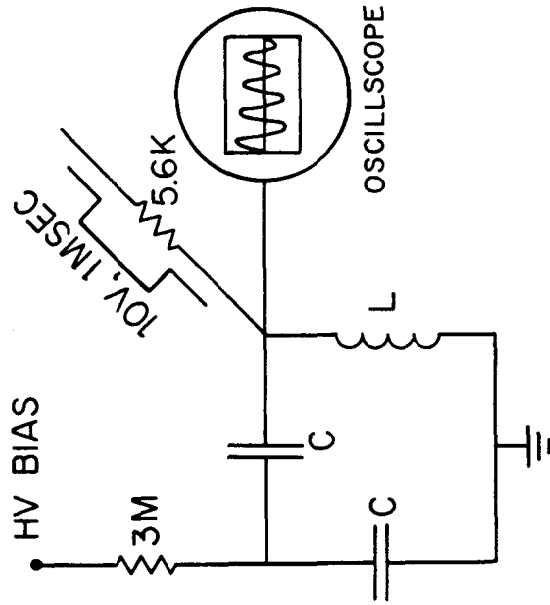


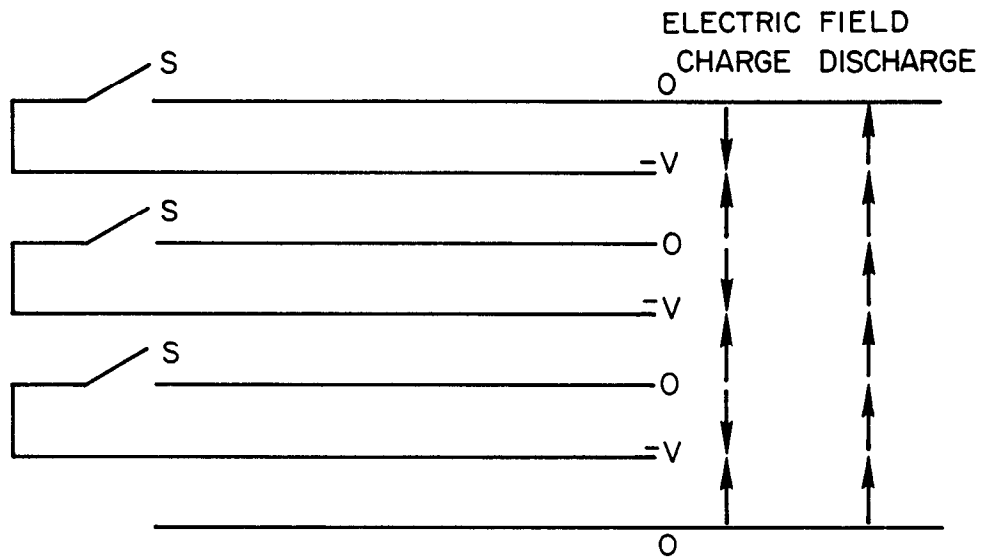
FIG. 25--Circuit for measuring the capacity at a given high voltage (a) and the results of such a measurement (b) made with a barium-titanate capacitor similar to those used in the 17-gap, 34-stage Marx generator.

757A32

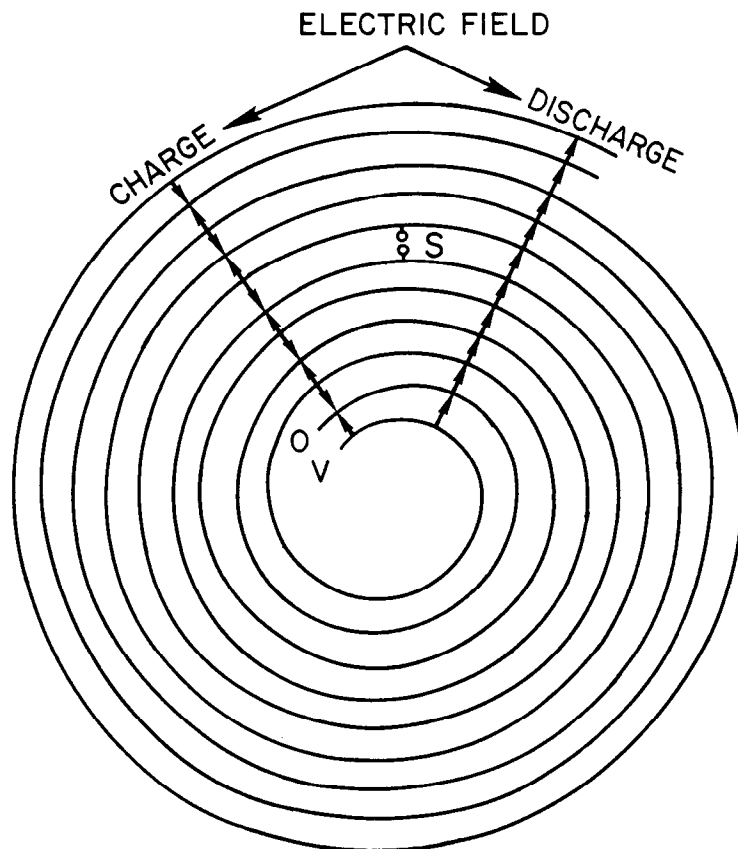
small and easy to construct; yet some have produced pulses of greater than 5 MV. High-power, iron-core transformers do not have sufficiently fast charging times for reasonable turn ratios; moreover, their energy transfer efficiency is low.

The principal disadvantages of the autotransformer from our point of view are the unproven reliability (e. g., for 10^6 pulses) and the necessity of keeping the primary spark gap inductance small. Low inductance spark gaps can easily be made with solid dielectrics; if only a few shots are required, the dielectric material can easily be replaced after each shot. Liquids might also work, but at 10 triggers/sec, it would probably be necessary to circulate the liquid to remove the gas bubbles formed between the electrodes. Gas gaps with an inductance $L_{\text{gap}} \lesssim 4 \text{ nH}$ should be feasible, but their reliability in this application is also questionable. Finally, we have had rather less experience with transformers than with Marx generators, and this may have been the principal factor in our choice of a Marx generator for the two-meter chamber. We feel, however, that the autotransformer is very suitable for testing breakdown in pulse forming networks, for switch tests, etc., where the number of pulses is small and where the repetition rate is of no importance.

For completeness we should mention two of the many transient high voltage generators described by Fitch and Howell.⁴⁸ The first, known as a "stacked strip-line generator," is shown schematically in Fig. 26a. Like the Marx generator, this is an example of a device in which a number of stages are charged in parallel and in which the electric field vectors are realigned so that the discharge is in series. The output voltage can be as high as $V_{\text{out}} = NV_{\text{in}}$, while the output impedance is $Z_{\text{out}} = N^2 Z_{\text{in}}$, just as in the case of the autotransformer with a turns ratio N . The impedance transfer equation again puts quite severe limitations upon the inductance of the spark gap when N is large and when the load is of low impedance.



(a)



(b)

757A33

FIG. 26-- Schematic drawings of a stacked stripline generator (a) and a spiral generator (b). These and several other generators are discussed in detail in the article by R. A. Fitch and V. T. S. Howell, Ref. 48.

A "spiral" or "toilet-roll" generator, shown schematically in Fig. 26b, is still another application of the parallel charge, series-discharge principal. The pulse generated when the spark gap fires follows the helical winding and realigns the electric field vectors until the output voltage $V_{out} = 2NV_{in}$ is reached, where N is the number of revolutions of the double winding. The input impedance problems of the autotransformer and stacked strip-line generator apply here as well. It is perhaps worth noting, however, that spiral generators are available commercially* which may be useful (with pulse shaping networks) in driving certain types of streamer chambers.

C. Pulse Shaping Networks

Let us return now to the equivalent circuit for a Marx generator given in Fig. 24 and determine the pulse shape that appears across the load. The net capacitance of the charging circuit (i.e., the circuit with S open) is given by:

$$\frac{1}{C_{net}} = \frac{1}{C} + \frac{1}{C_p} \quad (24a)$$

where $C = C_o/N$ as before. The Q value is now a factor of $(C/C_{net})^{\frac{1}{2}}$ larger than the value measured with the output shorted, and the ringing period T is decreased by $(C_{net}/C)^{\frac{1}{2}}$. The maximum voltage appears across C_p at approximately one-half the ringing period after the Marx is triggered, and its value is

$$V_{p-max} = 2V_{out} \left(\frac{C}{C_p + C} \right) \quad (24b)$$

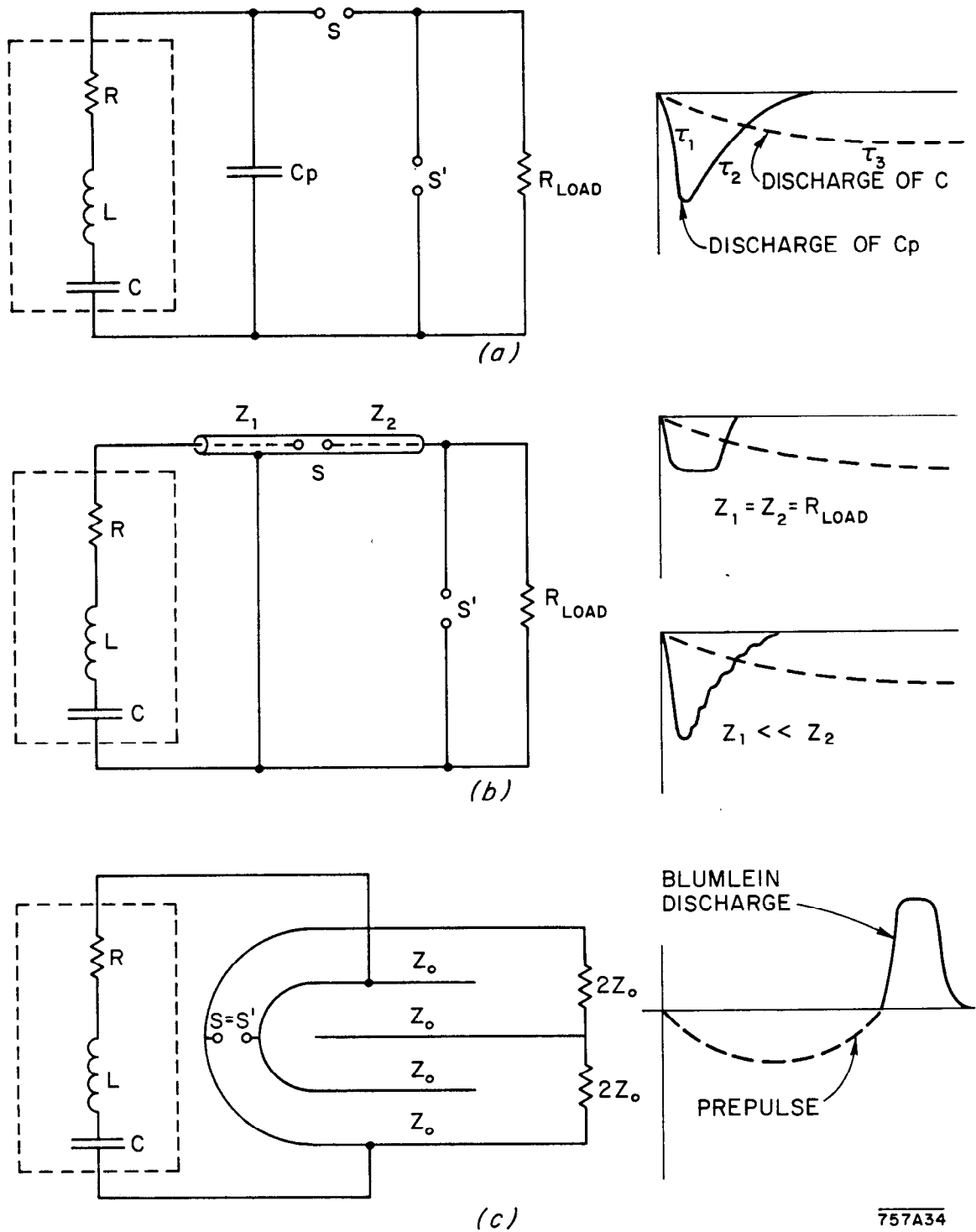
where $V_{out} = NV_{in}$ for the Marx generator. Thus by making $C_p \ll C$, it is possible to "ring" to a voltage that is nearly twice the normal output voltage of the Marx. (As discussed in Appendix C, a similar factor appears in the expression for V_{out}/V_{in} for transformers.)

*Tobe Deutschmann Laboratories, Canton, Massachusetts; Maxwell Capacitors, San Diego, California.

The pulse breakdown voltage of the output gap S can be adjusted by varying the electrode spacing or the pressure in the gap. In practice, it is usually convenient to adjust the spacing only at the beginning and to use a variable gap pressure for subsequent control of the breakdown voltage. Once the spark gap has fired, both the generator and the parasitic capacitors discharge into the load.

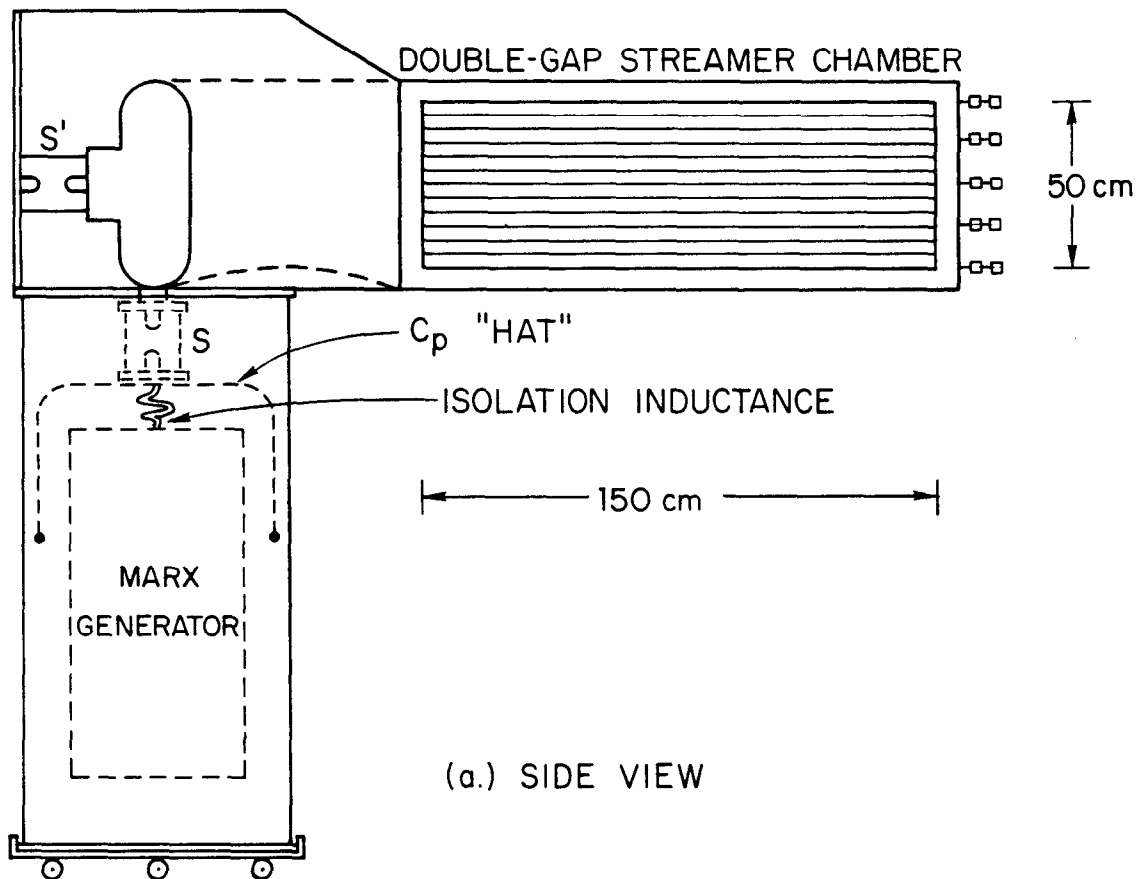
The discharge of C_p leads to an output pulse whose rise time τ_1 is determined primarily by the inductance of the spark gap and may be as short as 1 nsec. For a resistive load, the duration of the parasitic discharge is determined by the time constant, $\tau_2 \approx C_p R_{load}$, which can be of the order of 10 nsec. If $C_p \ll C$, the generator is still highly charged at $T/2$ when V_{p-max} is reached; the generator capacitance will discharge into the load with a time constant τ_3 which is longer than T and therefore much longer than the discharge time for the parasitic capacitance. The circuit diagram and the waveform seen at the load are shown schematically in Fig. 27a.

The parasitic capacitance is, of course, a rudimentary pulse shaping network. The value of C_p can be supplemented in various ways, one of which is shown schematically in Figs. 28a and 28b. Here we have added a metal "hat" to the output of a Marx generator contained in a cylindrical aluminum pressure vessel. By placing both the generator and the hat within the pressure vessel, we have avoided the breakdown problems which tend to occur in the slow, charging elements of the system, where the high voltage pulse is of much longer duration than the pulse finally appearing across the plates of the chamber. The capacitance between the hat and the generator pressure vessel discharges into the load when the spark gap S is closed. The first part of the output pulse is essentially independent of the internal inductance and resistance of the generator and can be quite short, as we have seen. Provided that $\tau_1 \ll \tau_2$ and $C \gg C_p \gg C_{load}$, the amplitude of

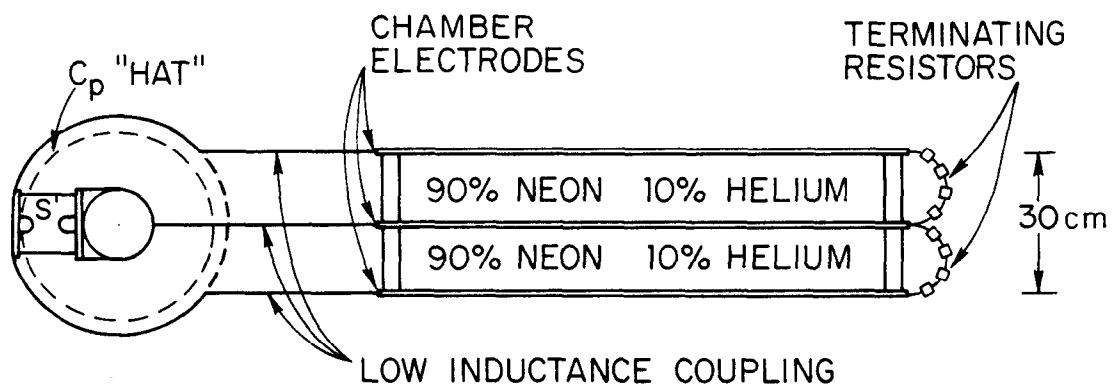


757A34

FIG. 27--Three pulse shaping networks driven by Marx generators. These are the capacitor with series (S) and shunting gaps (S') shown in (a), the dielectrically loaded line shown in (b), and the Blumlein line shown in (c). Also sketched are the characteristic output pulses for each type of pulse shaping network.



(a.) SIDE VIEW



(b.) TOP VIEW

757A35

FIG. 28--Two views of a system in which the parasitic capacitance C_p has been enhanced and in which series and shorting gaps have been added to a Marx generator to form a pulse shaping network. A photograph of this system is shown in Fig. 32.

the parasitic pulse on a small chamber can approach V_{p-max} and thus $2V_{out}$. A photograph of the system illustrated in Figs. 28a and 28b is given in the next chapter (Fig. 32).

When the circuit parameters have been properly chosen, there remains only the elimination of the generator pulse, which is too long to be useful in producing short streamers. This can be accomplished by adding a "shorting gap" or "crow-bar gap" (S' in Figs. 27 and 28) across the load and by adjusting this gap to fire after the peak voltage is reached. Such an adjustment is possible in a gas or a liquid gap due to the relatively long formative time for breakdowns in gases and liquids. (See Appendix A.) While we have discussed the capacitor plus series and shorting gaps only in connection with Marx generators, the various pulse shaping networks can also be used with any of the other generators mentioned in the previous section.

In Fig. 27b, a transmission line (e. g., a coaxial cable) is charged by the generator in place of the parasitic capacitance C_p . When the spark gap S fires, the first section of the cable Z_1 discharges into the second Z_2 producing a pulse that is $Z_2/(Z_1 + Z_2)$ times the charging voltage of Z_1 . This charging voltage can, of course, be made nearly twice the output of the generator by a suitable choice of cable and generator capacitances. If $Z_1 = Z_2$, as in the case of the "mercury switch pulser," the output pulse has a sharply defined rise and fall, but half the amplitude is lost. For $Z_2 \gg Z_1$ (the case of a dielectrically loaded line), the amplitude approaches that for the parasitic capacitance, and the pulse fall-off is a staircase function modulating the exponential discharge of a pure capacitance. The discharge of the generator also appears across the load as before, and a shorting gap S' is again required.

In designing a dielectrically loaded line, one normally treats the first section of the cable in Fig. 27b as a low inductance capacitor C_1 which discharges

into the line or the load Z_2 . C_1 and Z_2 are then chosen such that the product $C_1 Z_2$ is much greater than the required pulse duration $\tau \sim 10$ nsec. The output pulse is then cut off with the shorting gap as required. The capacitance of a coaxial, dielectrically loaded line is given by

$$C_1 \approx \frac{56 \epsilon_{rel}}{\ln \frac{r_2}{r_1}} \text{ pF/meter} \quad (25)$$

where r_1 is the inner radius and r_2 the outer radius. Water is probably the best choice for the dielectric, but we have also used ethylene glycol and glycerine. (See Appendix A for the breakdown properties of various liquids.) To reduce pulse jitter, the shorting gap is usually "prepared" by pretriggering with a pulse derived from the first stage of the Marx generator.

In Fig. 27c, the Marx generator has been connected to a Blumlein (strictly speaking, a Blumlein line).⁴⁹ As indicated in Figs. 29a, b, and c, the five-element Blumlein (a) is equivalent to a pair of three-element Blumleins (b), each of which can be decomposed for the sake of analysis into an open-ended line with one element interrupted by the load (c). We will assume initially an impedance of Z_0 per stage and a terminal impedance of NZ_0 for the three-element Blumlein. (As we shall show, $N = 2$ for impedance matching.)

At time τ after the Blumlein spark gap has fired, the transient voltage reaches the load, which now appears as NZ_0 in series with Z_0 . The transmitted pulse is

$$\begin{aligned} T &= V_0 \frac{2 [NZ_0 + Z_0]}{Z_0 + [NZ_0 + Z_0]} \\ &= V_0 \left[\frac{2N}{N+2} + \frac{2}{N+2} \right] \end{aligned} \quad (26)$$

where V_0 is the charging voltage, where $V_0 \frac{2N}{N+2}$ is the voltage across the

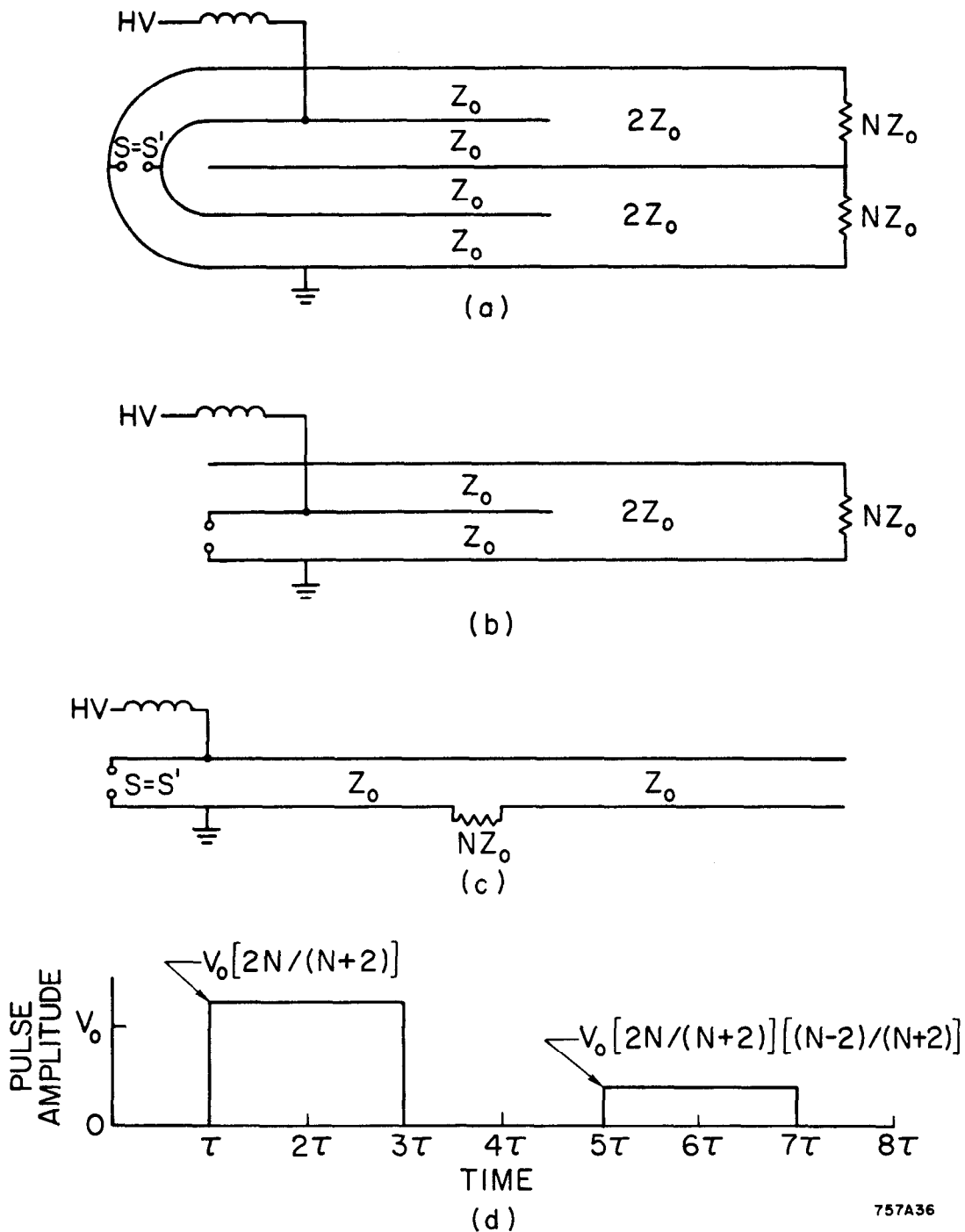


FIG. 29--Analysis of the operation of a Blumlein line. The five-electrode Blumlein (a) is equivalent to two three-electrode Blumleins (b) each of which can be considered as a constant impedance line interrupted at the center by the load NZ . The first Blumlein pulse begins at time τ after the spark gap fires and continues until time 3τ where τ is the time required for a wave to travel from the spark gap to the end of the charged electrode. When the impedances of the Blumlein and load are properly matched ($N=2$), the amplitude of the first pulse is equal to the charging voltage, and all succeeding pulses are zero.

load, and where $V_o 2/(N + 2)$ is the voltage of the wave which continues toward the open end of the line. The reflected pulse is of amplitude $-V_o N/(N + 2)$. The reflected and transmitted pulses are reflected again at the opposite ends of the line and arrive back at the load at time $2\tau + \tau = 3\tau$ after the spark gap has fired. Their sum is

$$\left\{ -V_o \left[\frac{N}{N+2} \right] \left[\frac{2N}{N+2} \right] - V_o \left[\frac{2}{N+2} \right] \left[\frac{2N}{N+2} \right] \right\} = -V_o \frac{2N}{N+2},$$

which exactly cancels the original pulse on the load and gives an output of zero starting at time 3τ . This continues from 3τ to 5τ , at which point further reflections lead to a second pulse of amplitude

$$V_o \left[\frac{2N}{N+2} \right] \left[\frac{(N-2)}{N+2} \right] .$$

The output as a function of time is indicated schematically in Fig. 29d.

If the Blumlein impedance is properly matched to the load (i.e., if $N = 2$), then the amplitude of the first pulse across the load is V_o , while all successive pulses are zero. The duration of the output pulse is 2τ , as we have already seen. There is, of course, no after pulse from the generator, which was immediately shorted to ground by the Blumlein spark gap ($S = S'$).

The Blumlein combines the desirable rectangular pulse shape of a uniform transmission line ($Z_1 = Z_2$) with the high voltage efficiency ($V_{out} = V_o$) of the dielectrically loaded line ($Z_2 \gg Z_1$). Furthermore, the output is automatically in the form of a pulse which can be transmitted to a large streamer chamber with complete impedance matching throughout. In the five-element Blumlein, the central element becomes the center electrode of the chamber, while the outside elements are extended to form the enclosing ground. Similarly, a three-element Blumlein is well suited to driving single-gap chambers.

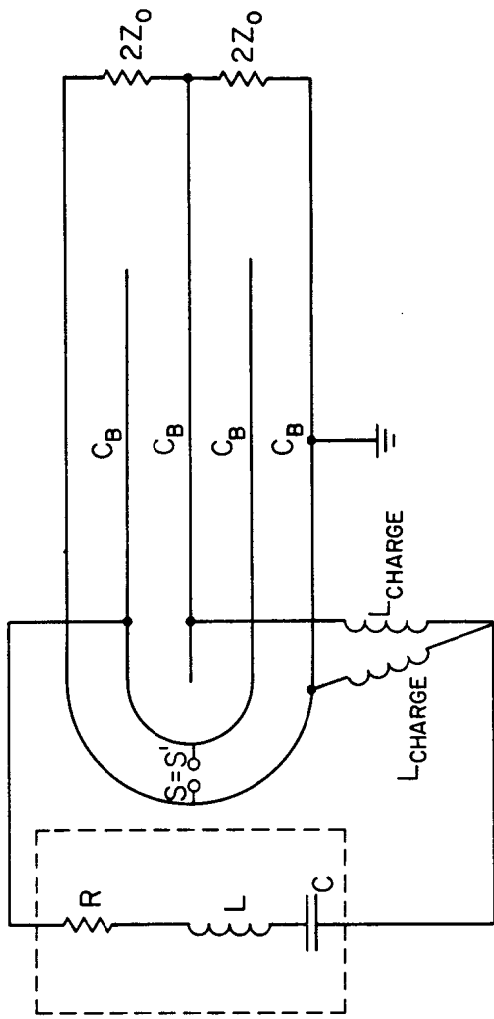
When we first considered using Blumleins as pulse shaping networks for large streamer chambers, we were quite concerned about the prepulse which

occurs across the load while the active element is being charged. The sign of this pulse is opposite that of the Blumlein discharge, while the areas of the two pulses are equal. Thus the amplitude of the prepulse is typically $V_{out} \cdot \left(\tau_{Blumlein} / \tau_{charge} \right)$ where V_{out} is the amplitude of the Blumlein pulse and $\tau_{Blumlein}$ and τ_{charge} are the respective pulse durations. By using the bridge charging circuit of Figs. 30a and b, it is possible to control the amplitude of the prepulse and even to reverse the sign to the same polarity as the output pulse. More importantly, the amplitude can be adjusted empirically until the displacement of the streamer origins is zero--something which, as far as we know, has not yet been achieved with other pulse shaping networks.

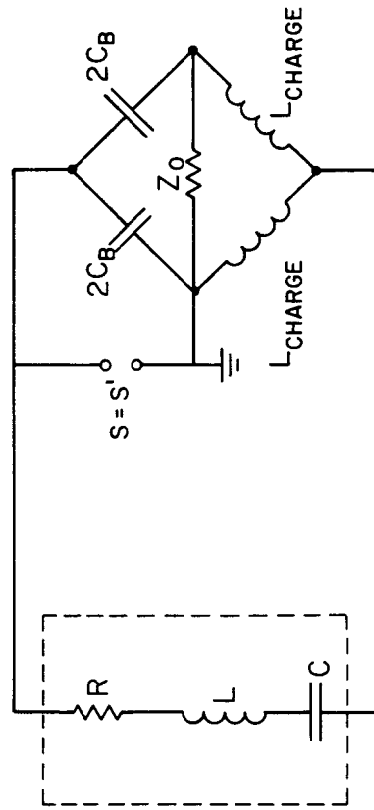
D. Pulse Monitoring

We have used both resistive and capacitive probes in monitoring fast high voltage pulses. An example of a resistive probe is shown schematically in Fig. 31a. Its attenuation factor is about 53. The input resistance of about 1000 ohms is distributed along a string of 10 internal carbon resistors, and the impedance looking back into the output is 50 ohms to match 50-ohm coaxial cable. The probe shown has been used to monitor pulses of up to 25 kV and has an intrinsic rise time of about 1 nsec. For higher voltages, the probe can be connected across one or two carbon resistors near the grounded end of a resistor string. A low inductance groundstrap then completes the circuit. Normally a Tektronix 519 oscilloscope with attenuators and impedance adaptors is used to display the signal from the probe.

A capacitive probe is shown in Fig. 31b. Such probes can be mounted just inside the groundplate of a transmission line and are not portable. Capacitive probes tend to ring unless great care is taken in the design. An important source of the ringing of a probe built into a transmission line is the difference in wave velocity in the dielectric of the probe and the dielectric of the transmission line.



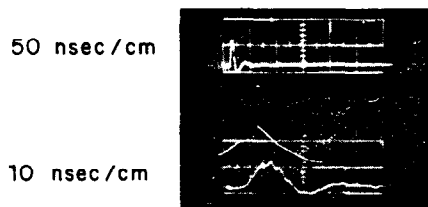
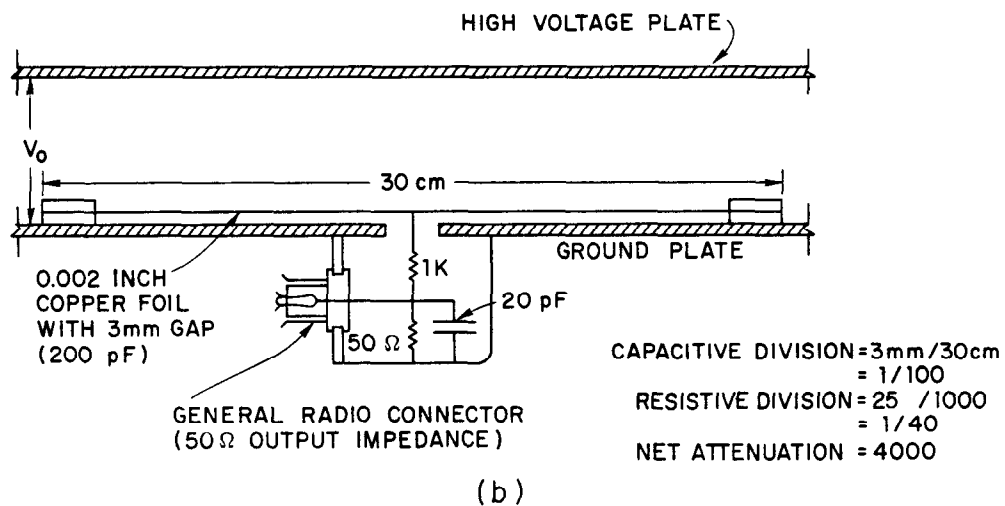
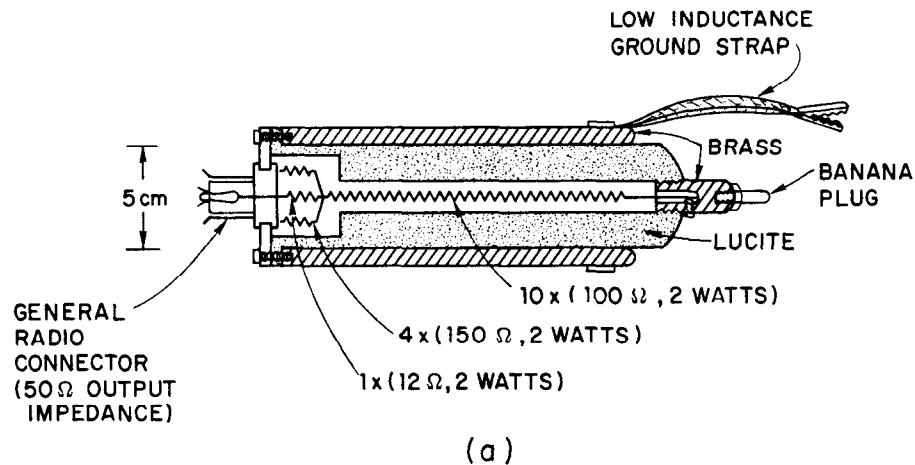
(a.)



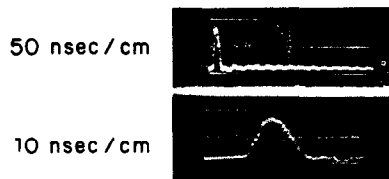
(b.)

757A37

FIG. 30--Charging the Blumlein with a bridge circuit to control the Blumlein prepulse which appears across the chamber. By adjusting the prepulse properly, one can cancel the displacement of the streamer origins which normally occur when a driving pulse of only one polarity is used.



RESISTIVE PROBE
(c)



CAPACITIVE PROBE
(d) 757B45

FIG. 31--A resistive probe (a), a capacitive probe (b), and the pulses (c and d) obtained on the 2-meter streamer chamber with each. The pulses are similar for the two probes except for the small amplitude, high frequency ringing in the capacitive case. The pulse amplitude for streamers is nearly 600 kV across the 30-cm chamber gaps. The rise time is 4 nsec and the pulse duration about 12 nsec at half the peak voltage. The characteristic rise time for each probe is about 1 nsec.

This problem can be solved either by using the same dielectric in the probe and the line or by making the thickness of the metallic conductor of the probe less than the skin depth, as suggested by Schneider.⁵⁰ In the capacitive probe shown, we have mounted a copper foil between two lucite rings so that the dielectric is air in the probe as well as in the line. A 1000-ohm resistor is installed in series with the output so that the pulse is not severely differentiated by the probe capacitor across the 50-ohm cable terminated at both ends. (The capacity is 200 pF, and the differentiating time with the 1000-ohm resistor is about 200 nsec.) The capacitive division in a typical case is $3 \text{ mm}/30 \text{ cm} \approx 1/100$ with an additional resistive division of $25 \text{ ohms}/1000 \text{ ohms} = 1/40$. Thus the total attenuation is 4000. With attenuations as high as this, care must be taken that pickup in the cable does not mask the attenuated pulse. Even with the pseudocoaxial geometry used in the Blumlein and two-meter streamer chamber, additional rf shielding of the signal cable is necessary to obtain clean pulses.

Typical pulses obtained with resistive and capacitive probes on the two-meter streamer chamber are shown in Figs. 31c and d.

VI. DEVELOPMENT OF THE TWO-METER STREAMER CHAMBER

It seems appropriate in this final chapter to bring together the essential points from the rather diverse subject matter already considered. This we hope to accomplish quite naturally by summarizing the major steps leading to the development of the two-meter chamber and by then describing the final system in which the various physical components are joined. In the third section we discuss the actual performance of the two-meter chamber during the preliminary stages of the photoproduction program, and in the final section we consider future developments and applications.

A. A Brief History

Work on streamer chambers at SLAC began near the end of 1963, shortly after the early Russian articles^{3, 4, 51} appeared. Originally, this effort was motivated by the considerable promise which these devices, as compact, isotropic detectors of high resolution, held for colliding beam experiments at energies well above 1 GeV. Within the next year, plans were also being made by a second group at SLAC to incorporate a streamer chamber of small dimensions into photoproduction experiments designed around conventional spark chambers. As the advantages and feasibility of the streamer chamber approach became more evident, the small streamer chamber grew in size from this modest beginning until it filled entirely the large magnet volume reserved originally for the conventional chamber. By mid-1965, the photoproduction group was so strongly committed to the development of a large streamer chamber that a chamber of a smaller size, then known to be feasible, was considered preferable to ordinary spark chambers in the event that a two-meter chamber could not be achieved before a beam was available from the new accelerator.

In the first attempts at SLAC, a Marx generator was used directly to drive a small single-gap chamber, and a chain of resistors was connected across the chamber plates to shape the driving pulse via an exponential RC decay. The Marx generator had 10 spark gaps, 10 capacitive stages, and a single 30-kV, 1800-pF capacitor per stage. Because of breakdown problems, it proved necessary to enclose the generator within a pressurized vessel before the full 300-kV, 180-pF output capability was realized.

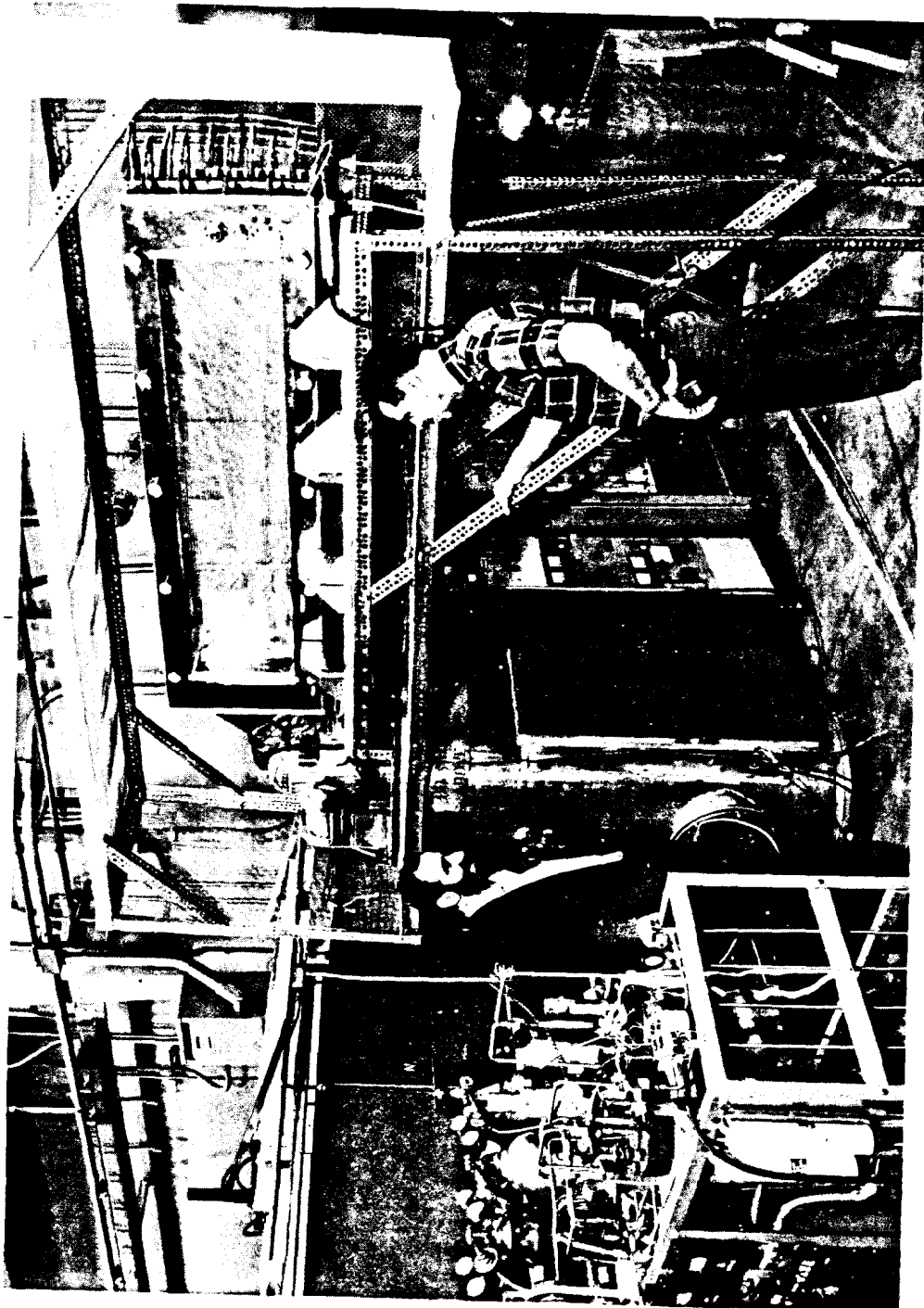
Toward the end of 1964, attempts were made to reduce the duration of the driving pulse from the Marx by decreasing the resistance across the chamber. The result was a drop in the peak voltage, due not to the internal resistance of the Marx as originally believed, but rather to the internal inductance. It was at this point that we first measured the internal inductance of the Marx by putting a low inductance short across the output and by measuring the waveform across this short.

At about the same time we learned of the Soviet successes^{5, 12} using a Marx to charge a low inductance capacitor followed by series and shorting gaps as a pulse shaping network. The first piece of information on internal inductance indicated the fundamental limitations in using a Marx directly to drive large streamer chambers; the Soviet work pointed to the way out. The extrapolation of Marx generator designs to meet higher voltage requirements is really quite straightforward once the severe restrictions imposed upon the internal impedance by requirements of fast rise time and short pulse duration are relaxed.

Throughout 1965, the 300-kV Marx generator with capacitor and series and shorting spark gaps was used with a number of chambers to study basic streamer properties such as brightness, length, and memory time, as well as the related problems of photography and the effectiveness of various gas mixtures. A typical chamber from this period had 50-cm \times 50-cm plates separated by a single 10-cm

gap (Fig. 15). One plate was of solid aluminum and the other either of conducting glass or of stretched wires. The gas was contained within a lucite box capable of being evacuated before it was filled with the neon-helium gas mixture.

Beginning around February 1965, effort was concentrated on obtaining high voltages across low impedances. "Mercury switch" type transmission lines were tested as well as intermediate capacitors with series and shorting gaps. A Marx generator with 5 spark gaps, 10 capacitive stages and a single 40-kV, 2000-pF capacitor per stage was developed about March 1965, and with a mercury switch transmission line produced a 200-kV pulse across a 40-ohm load. This generator was used by D. Benaksas and R. Morrison at Stanford in triplet production experiments involving an incident photon beam. Meanwhile, work was beginning on two larger generators having 10 spark gaps, 20 capacitive stages, and two 30-kV, 3000 pF capacitors per stage. In December 1965, one of these produced pulses of 560 kV and was used successfully to drive a 40-ohm terminated chamber whose dimensions were 50 cm \times 150 cm with two gaps of 15 cm each. The pulse shaping network was of the capacitive type with series and shorting gaps, and both lucite and eventually polyurethane cells were used. These cells had 0.0015-inch laminated mylar windows and were wrapped with nylon fishline to prevent breakdown in the chamber gas near the wire electrodes. A photograph of this system is shown in Fig. 32. The second generator, with a coaxial, glycerine dielectric capacitor followed by series and shorting gaps, was used successfully in May 1966 to drive another chamber terminated with 100 ohms and having 100-cm \times 125-cm plates and a single 30-cm gap. The intense rf radiation emitted from the single-gap chamber reinforced our decision to use a "coaxial" double-gap geometry in the two-meter design. A copy of this second drive system is now being used by B. Hughes, et al., at Princeton University to pulse a chamber roughly 30 cm \times 50 cm with double 15-cm gaps.



757A39

FIG. 32--Photograph of a double-gap streamer chamber driven by a Marx generator with an intermediate capacitor and with series and shorting spark gaps used as a pulse shaping network. The chamber, with electrodes in the vertical plane, has a sensitive volume 50 cm wide and 150 cm long with two gaps of 15 cm each. Drawings of this system are shown in Figs. 28 a and b.

While tests of these two large chambers were going on, other members of the photoproduction group were experimenting with Blumleins of cylindrical, parallel-plate, and tapered geometries in an effort to determine whether or not this device would ultimately serve as a satisfactory pulse shaping network for the two-meter streamer chamber. Our principal sources of information on the proper use of Blumleins as well as on the use of oil and water as insulators and on the process of spark formation and high voltage breakdown were J. C. Martin and I. Smith of AWRE, both of whom visited our laboratory and worked with us during this period.

As a result of the successful tests of the 20-stage Marx generators, the various Blumleins, and the prototype streamer chambers, we began designing a still larger generator, a suitable Blumlein, and the two-meter streamer chamber. The new system was assembled by August 1966, and streamers were first observed in the two-meter chamber on September 1. In the period from September 1966 to March 1967, a still larger Marx generator was built and a more conservative Blumlein constructed to provide the highly reliable and easily repairable drive system required for the photoproduction program.

The important landmarks in the development of the two-meter streamer chamber are summarized below.

November 1963	First work on streamer chambers at SLAC begins.
November 1963 - January 1966	Studies of streamer properties undertaken.
February 1965	Decision made to try for high voltages across low impedances.
April 1965	200-kV across a 40-ohm load achieved.
December 1965	Streamers observed in a 40-ohm, double 15-cm gap chamber 50 cm wide and 150 cm long.

May 1965	Streamers observed in a 100-ohm, single 30-cm gap chamber, 100 cm wide and 125 cm long.
August 1966	Two-meter chamber assembled.
September 1, 1966	First streamers observed in two-meter chamber.
March 28, 1967	First tests of the two-meter chamber and magnet in the photon beam performed.

We will conclude this section with some advice based upon our numerous mistakes.

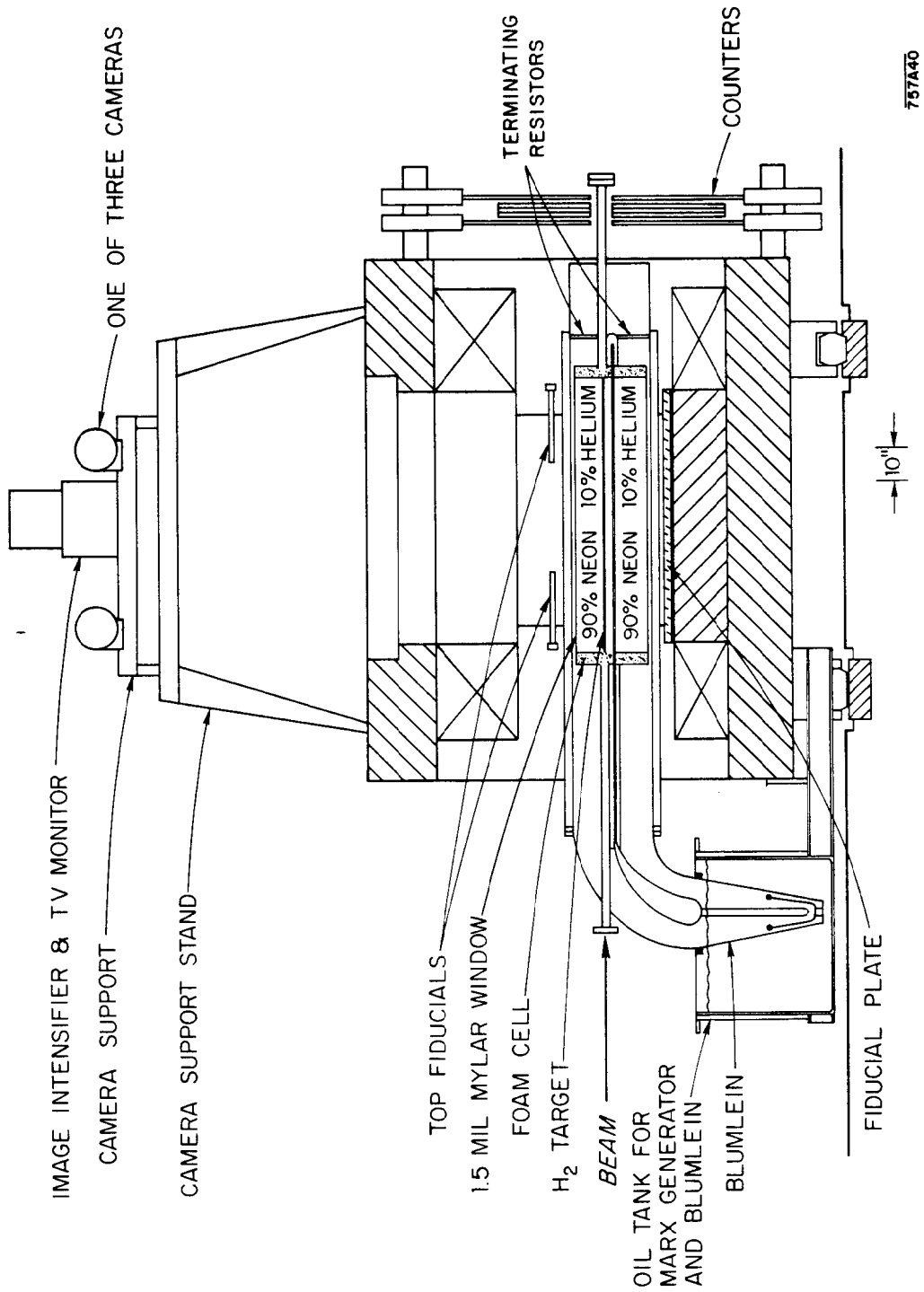
1. Don't worry about the rise time of the Marx, i. e., plan to use a pulse shaping network unless the chamber is small.
2. Don't try to use fancy pulse shapes such as damped oscillation pulses, positive followed by negative pulses, etc., to try to reduce the required voltage. As far as the streamers are concerned, practically any pulse can be reduced to an equivalent pulse of the same absolute voltage.
3. Don't be afraid of large Marx generators. Design for roughly twice the required voltage and roughly 50% more than the capacity of the pulse shaping network.
4. Choose a design such that all components are readily accessible. Among other things, this means putting the Marx in a large tank and using oil, not compressed gasses, to prevent breakdowns. Don't worry about oil purity.
5. Don't use transmission lines in place of capacitors in the Marx generator to avoid an intermediate pulse shaping network. The inductance in the generator spark gaps will spoil the pulse rise time on a low impedance load.

6. Use inexpensive capacitors in the Marx. Don't try to minimize the internal impedance by purchasing special low impedance, high voltage capacitors.
7. Make sure that the power supply has sufficient current capacity to charge the Marx in the time allowed by the design repetition rate, and check the power dissipated in the charging resistors.
8. Check that enough energy ($1/2 CV^2$) is stored in Marx generator and pulse shaping network to drive the chamber with a suitable margin of safety.
9. Don't worry about dielectric losses.
10. In general, use a capacitor with series and shorting gaps to drive chambers of medium size; use Blumleins to drive chambers of large size. Remember that since the charging pulse is of much longer duration than the discharge which appears across the plates of the chamber, special care must be taken to prevent breakdown in the charging elements.
11. Don't worry about depth of field. This is easily solved by choosing a high demagnification.
12. Don't be enamored with 90° stereo. The 18° stereo used here permits longer streamers and more light, and it reduces the depth of field problem.
13. Gas impurities should be below $1/2\%$ within the sensitive chamber volume. It is convenient in the case of large chambers to have available some means of testing the gas purity.
14. For large chambers the chamber gas should be contained within cells which are removable and independent of the electrode structure.
15. Don't try to use pulsed pressurized spark gaps with fields greater than 600 kV/cm . Recall that SF_6 has a breakdown voltage of 90 kV/cm/atm .

B. Summary of the Final System

The experimental arrangement used in the photoproduction experiment is shown schematically in Figs. 33, 34, and 35. Photographs of the installation are shown in Figs. 36 and 37. A highly collimated, hardened bremsstrahlung beam is incident from the left in Fig. 33. The first part of the 4 atm hydrogen gas target is of 2-inch i.d. lucite pipe which passes through the ground electrode of the "elbow" connecting the Blumlein and the streamer chamber. From here the target pipe is suspended just above the central high voltage plate and extends essentially to the wall of the upper foam cell. After passing through the cell wall, the beam enters the 1/2-inch diameter, 0.002-inch wall thickness, mylar tube which crosses the chamber.

Events which occur in the target produce charged particles which are detected by counters located downstream of the streamer chamber. The beam itself passes through a 4-inch-high slot at the center of the counter array, enters another vacuum pipe, and is monitored 40 meters beyond the streamer chamber with a quantameter.⁵² When the counters indicate that an event has occurred, a signal is sent from the counter electronics to a 20-kV pulse generator which then triggers the Marx generator. The energy stored in the Marx is used to charge a Blumlein contained within the same oil tank. The oil is used in this case to prevent breakdowns which tend to occur in the slower charging elements of the system where the pulse duration is much longer than the pulse which appears finally on the plates of the chamber. The Blumlein spark gap fires when the charging voltage is near its maximum value; some 500 nsec after the original event, a 10-nsec, 600-kV pulse reaches the chamber. The streamer tracks are photographed by the open-shuttered cameras, the fiducials are flashed, and finally the cameras are advanced and the Marx generator recharged in preparation for the next event.



757A40

FIG. 33--Side view of the experimental arrangement for the photoproduction program. A highly collimated, hardened bremsstrahlung beam is incident from the left and passes through a 1/2-inch-diameter hydrogen gas target in the upper of two foam cells.

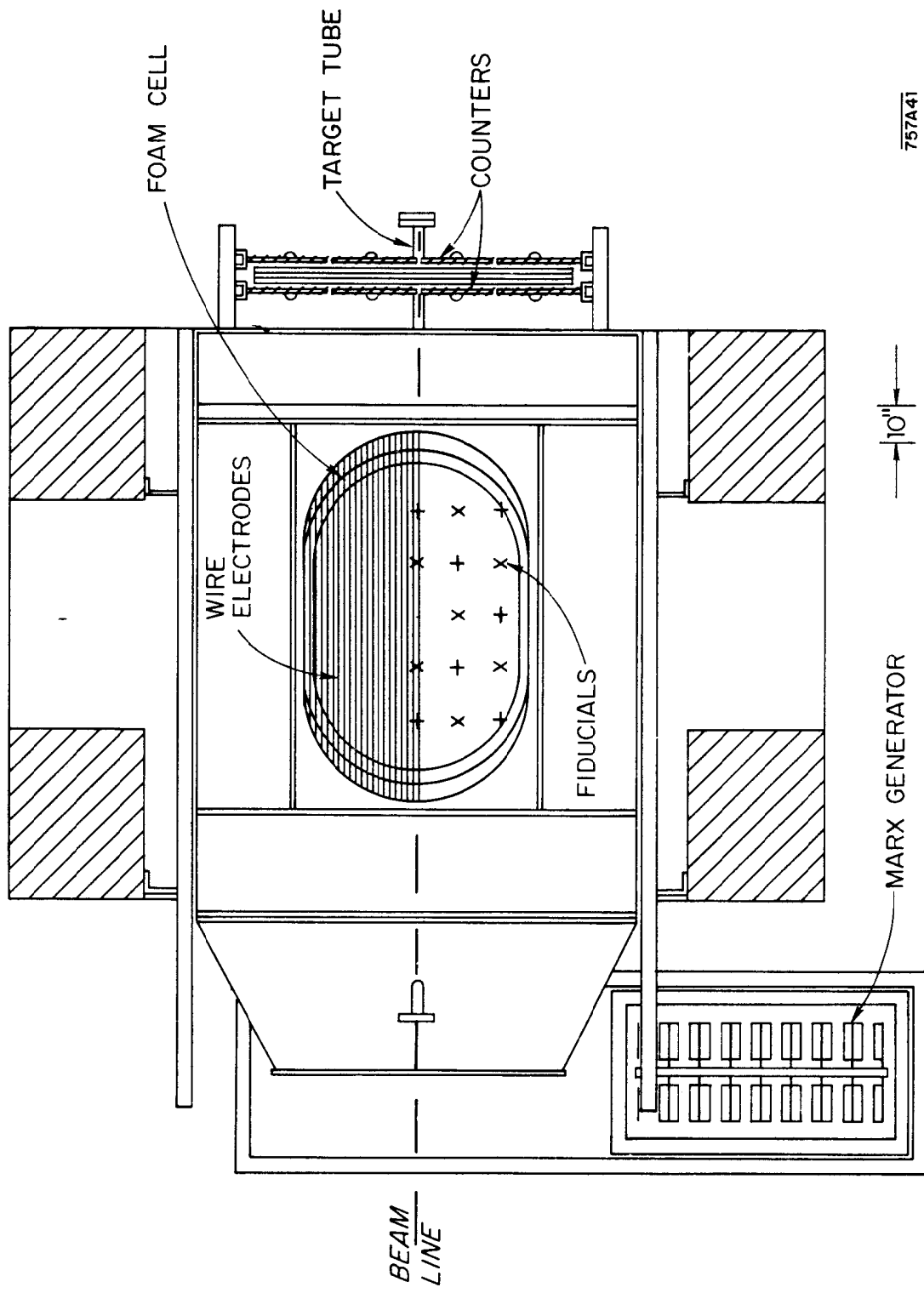
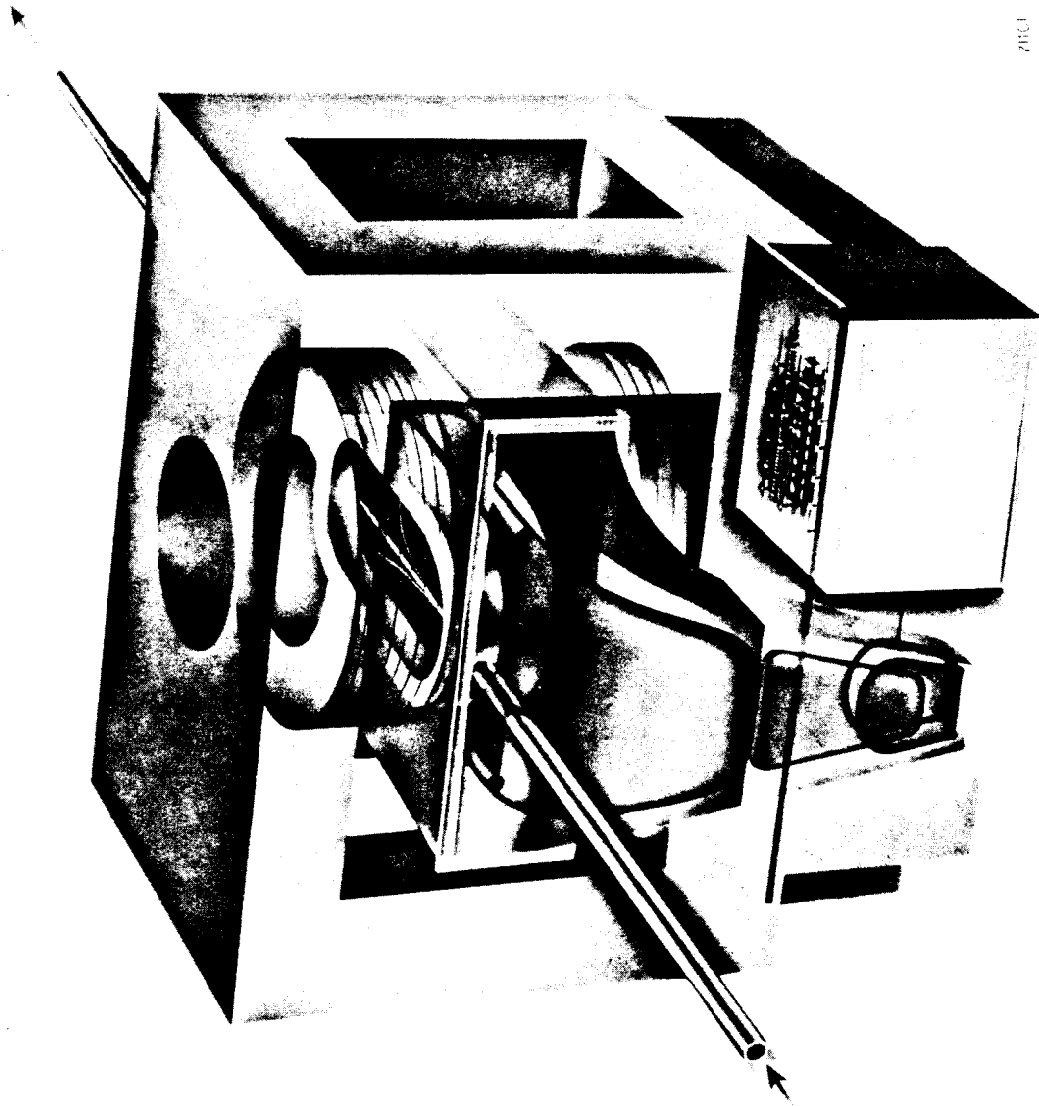
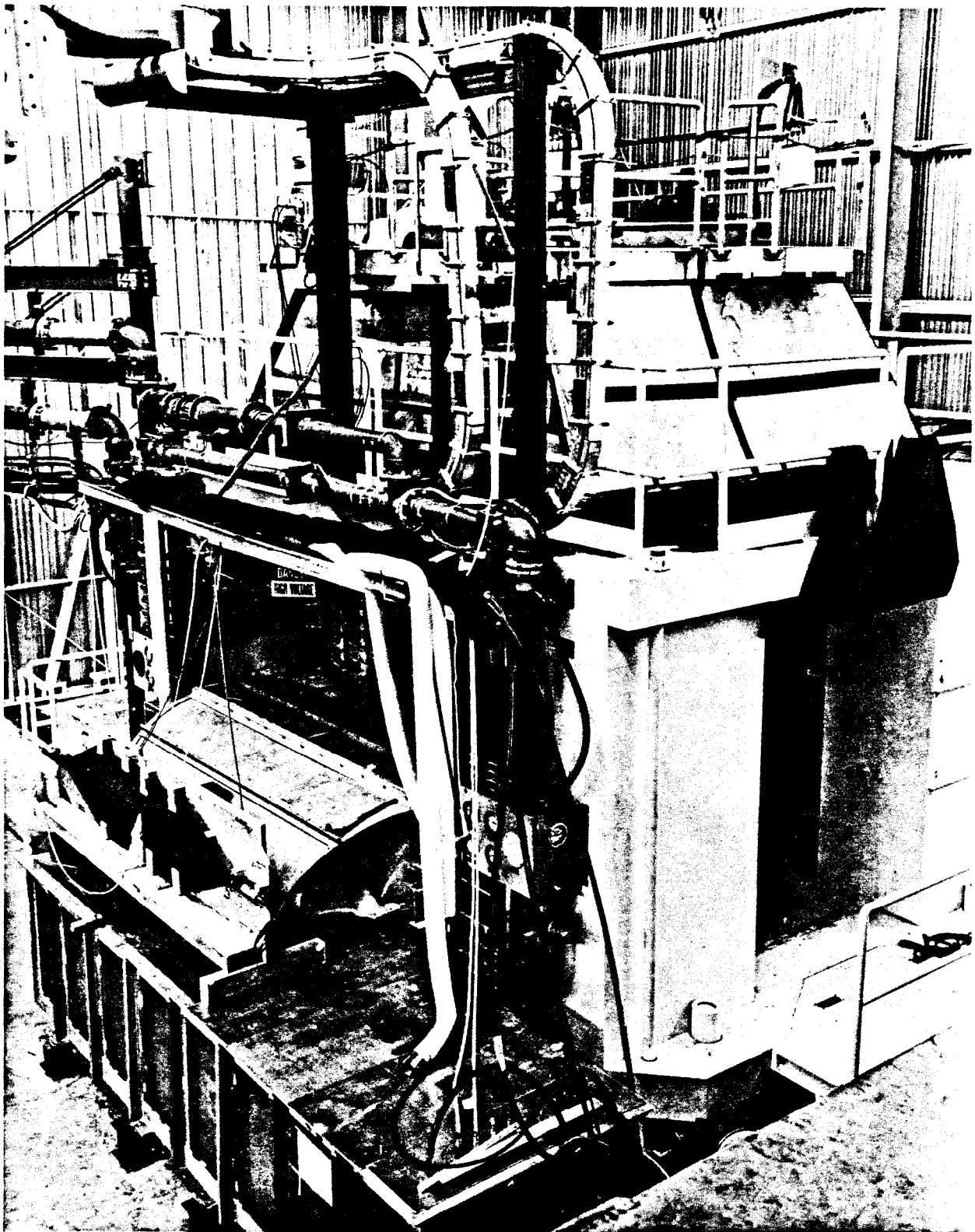


FIG. 34--Top view of the experimental arrangement for the photoproduction experiment. Events which occur in the chamber are photographed stereoscopically by three cameras through the hole left by the absent upper pole piece. The magnet windings, three below and seven above, are unbalanced to compensate for the missing pole piece and to improve the field uniformity.



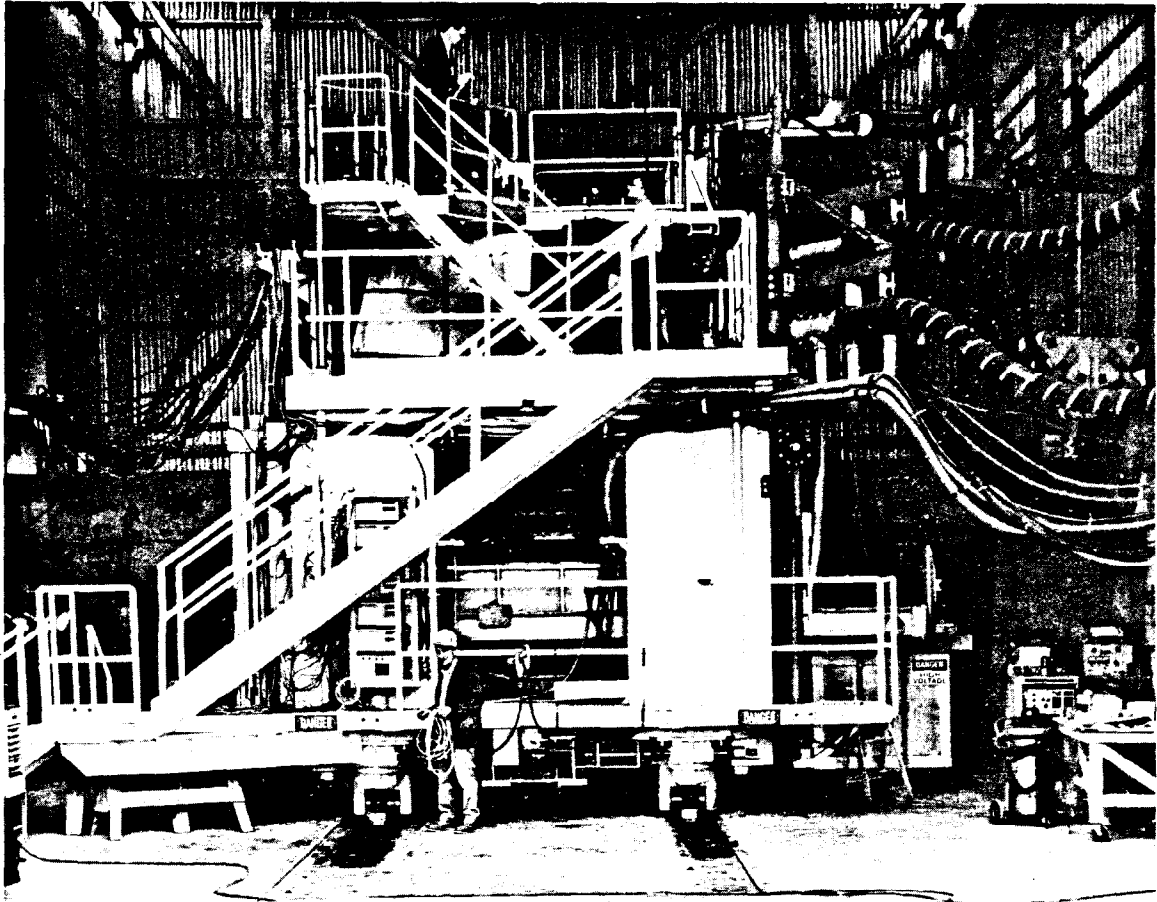
7101

FIG. 35--A three-dimensional, x-ray vision drawing of the experimental arrangement for the photoproduction program.



757A49

FIG. 36--A photograph of the experimental arrangement for the photoproduction program. The view is similar to that shown in Fig. 35, but the vacuum pipe for the photon beam is not in place.



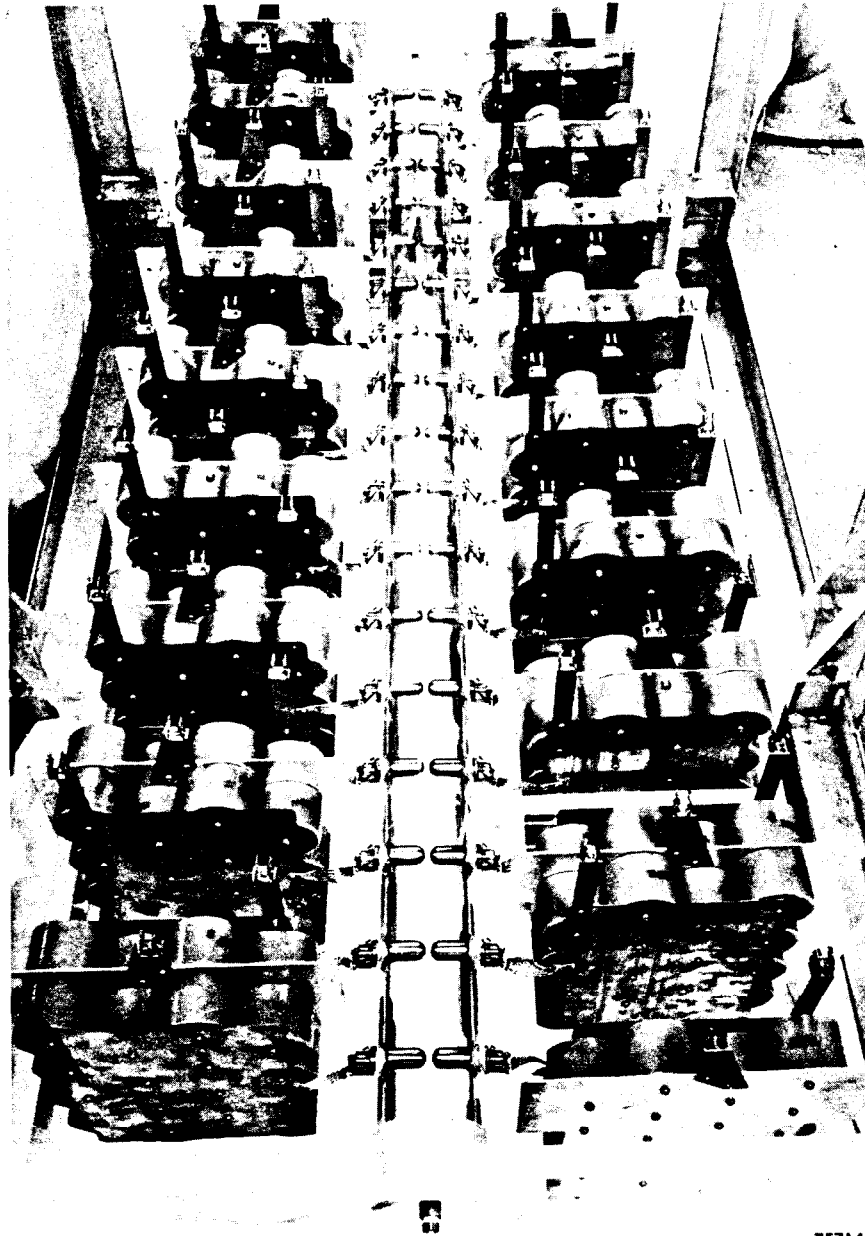
757A50

FIG. 37--Photograph of the experimental arrangement for the photoproduction program. In this figure, the beam is incident from the right. The "elbow" can be seen on the right arching from the Marx generator - Blumlein oil tank to the streamer chamber, which passes through the magnet between the visible upper and lower magnet coils. The vertical trigger-counter array, consisting in this case of 16 counters, is supported on the downstream side of the magnet. The trigger electronics is visible on the magnet column nearest the counters. The magnet, including the entire streamer chamber and drive system and the trigger counters, can be driven in and out of the photon beam along the tracks visible in the floor.

The coils of the 400-ton magnet are assembled 3 below center and 7 above to improve the field uniformity in the absence of the removable top poleface. The 16-kG field is then uniform to about 20% over the 1-meter gap and 2-meter diameter poleface. A marble fiducial plate is pinned to the lower poleface and supports an array of 25 fiducials. The two upper fiducials are supported on granite beams which are attached to the opposite columns of the magnet and which span the gap between the columns above the streamer chamber. The three cameras view the chamber in 18° stereo through the hole in the top of the magnet left by the absent polepiece.

The two 50-kV Marx generator power supplies have internal resistances of 25 kilohms, so that the peak charging current is limited to 2 amps. The charging resistors of the Marx contribute another 15 kilohms. Each supply then charges 0.5 μ F in series with 40 kilohms, and together the two charge the Marx to within 2% of the charging voltage in less than 0.1 sec. In practice the charging voltages are about \pm 20 kV, so that the energy stored is 100 joules and the output energy 200 joules per pulse for each supply. At 10 pulses per second, this is 2 kW per supply, well below the 12-kW level at which the supplies have been run continuously for two hours.

Figure 38 is a photograph of the Marx generator. The circuit diagram was shown previously in Fig. 23. This generator consists of 34 stages, has sixteen 40-kV, 2000-pF capacitors per stage, and is capable of storing 800 joules at 40 kV and of producing an output in excess of 1.3 MV with an output capacity of about 1000 pF. This is about twice the voltage required to drive the two-meter chamber. The elements of the Marx generator, including the capacitor stages and the spark gap manifold, are readily accessible and can be quickly disconnected and replaced in case of component failure during a run. The connections of the charging resistors and flexible ground straps to the capacitor stages and the spark gap



757A42

FIG. 38--Photograph of the 17-gap, 34-stage Marx generator used to drive the 2-meter streamer chamber. A circuit diagram of this generator appears in Fig. 23. The carbon rod resistors used in charging the capacitor stages are not shown in the photograph, but supporting fixtures can be clearly seen. The modular construction permits the rapid removal of any stage in case of capacitor failure, and the spark gap manifold can also be replaced in a matter of minutes. The arrangement of the capacitor stages is designed to enhance the inter-stage capacity C_I and the stray capacity C_S to ground, while the capacity of each spark gap C_G is minimal. Thus the design satisfies the condition $C_G \ll C_I, C_S$ as discussed in the text. In addition, light emitted from any one gap has an excellent chance to induce photoionization in the succeeding gaps and thus to insure the reliable triggering of all gaps.

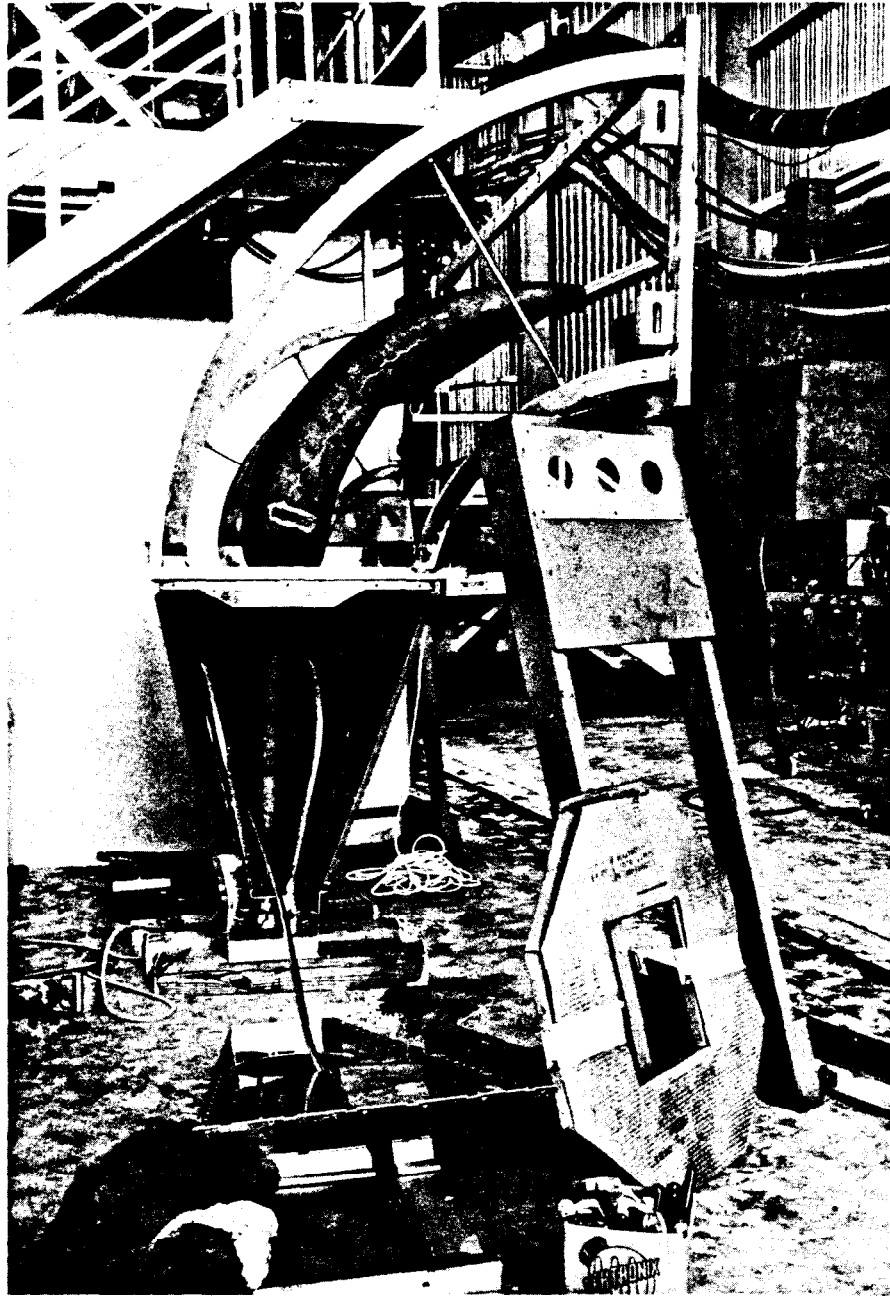
manifold are made with fuse clips.

The vertical Blumlein and the "elbow" which connects the Blumlein to the horizontal chamber are shown separately in Fig. 39. The Blumlein itself is contained within the same oil tank as the Marx generator. The Blumlein spark gap, which is located between the outermost or ground electrode and the charging electrode and which is the Blumlein component most subject to failure, is bolted to the bottom of the charging electrode. It is clamped to the grounded electrode in such a way that the spark gap and charging electrode can easily be removed without disturbing the rest of the structure. The electrode spacing of the pressurized spark gap is not adjustable, and the breakdown voltage is controlled by adjusting the SF₆ gap pressure instead. A tapered, constant impedance transmission line carries the pulse from the Blumlein to the chamber and matches the larger chamber dimensions to the final dimensions of the Blumlein.

A photograph of the streamer chamber as viewed from the downstream end is shown in Fig. 40. The total sensitive volume defined by the two polyurethane foam cells is approximately 2.3 meters long, 1.5 meters wide, and 60 cm high. The electrode structure is about 4 meters long, 3 meters wide, and 70 cm high. The gap spacing could be increased by substituting taller side walls and foam cells while retaining the same electrodes. However, the lower fiducials already take up about 10 cm of the 15-cm space left below the chamber, and only a small increase in chamber depth is possible with the existing magnet. As indicated in Fig. 40, the chamber is terminated above and below the central high voltage plate by a series of carbon rod resistors. A photograph of a completed foam cell containing a 1/2-inch-diameter target is shown in Fig. 41.

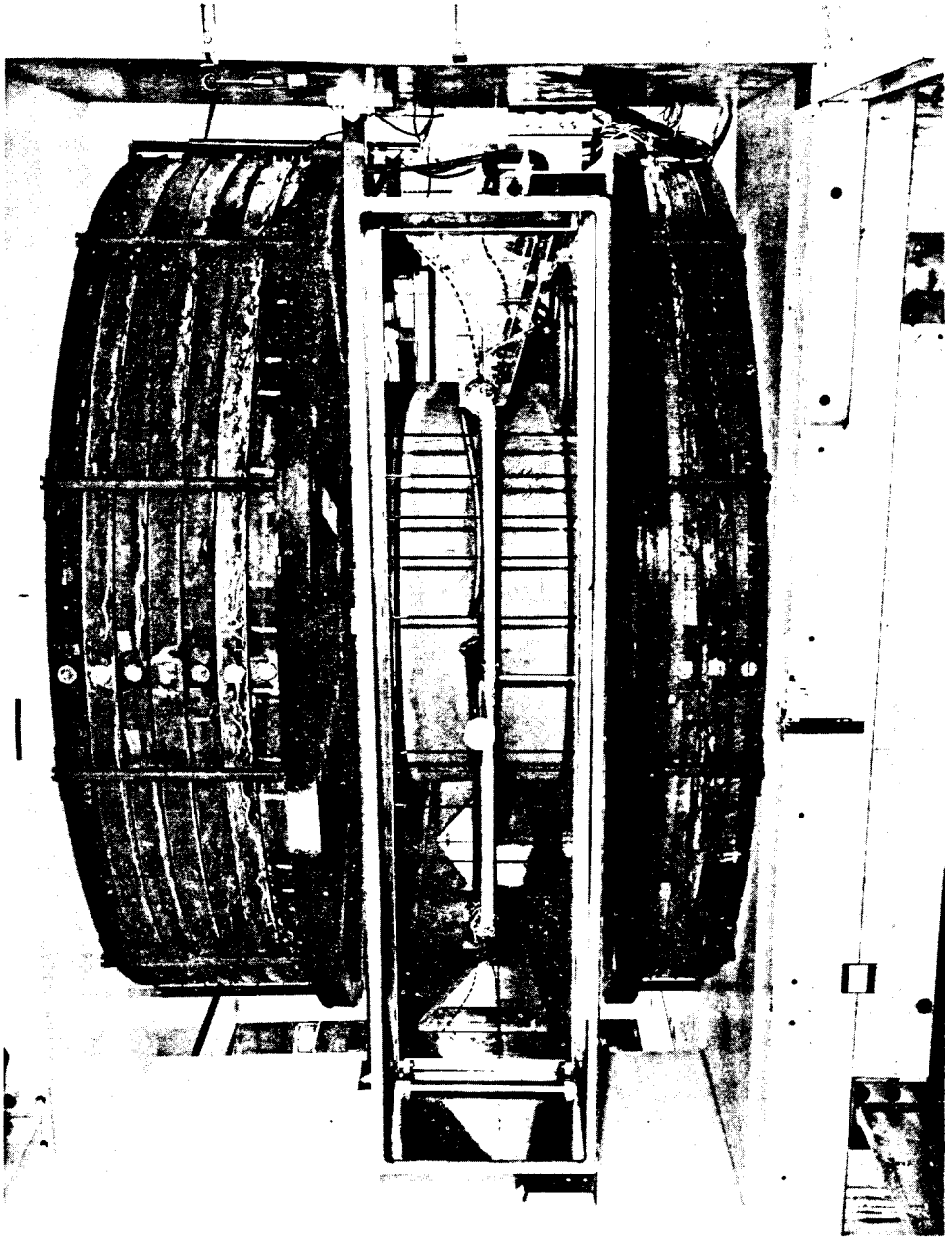
C. Initial Performance of the Two-Meter Streamer Chamber

While it is much too early to judge the ultimate worth of the two-meter streamer chamber as a tool for doing physics, we can say without hesitation



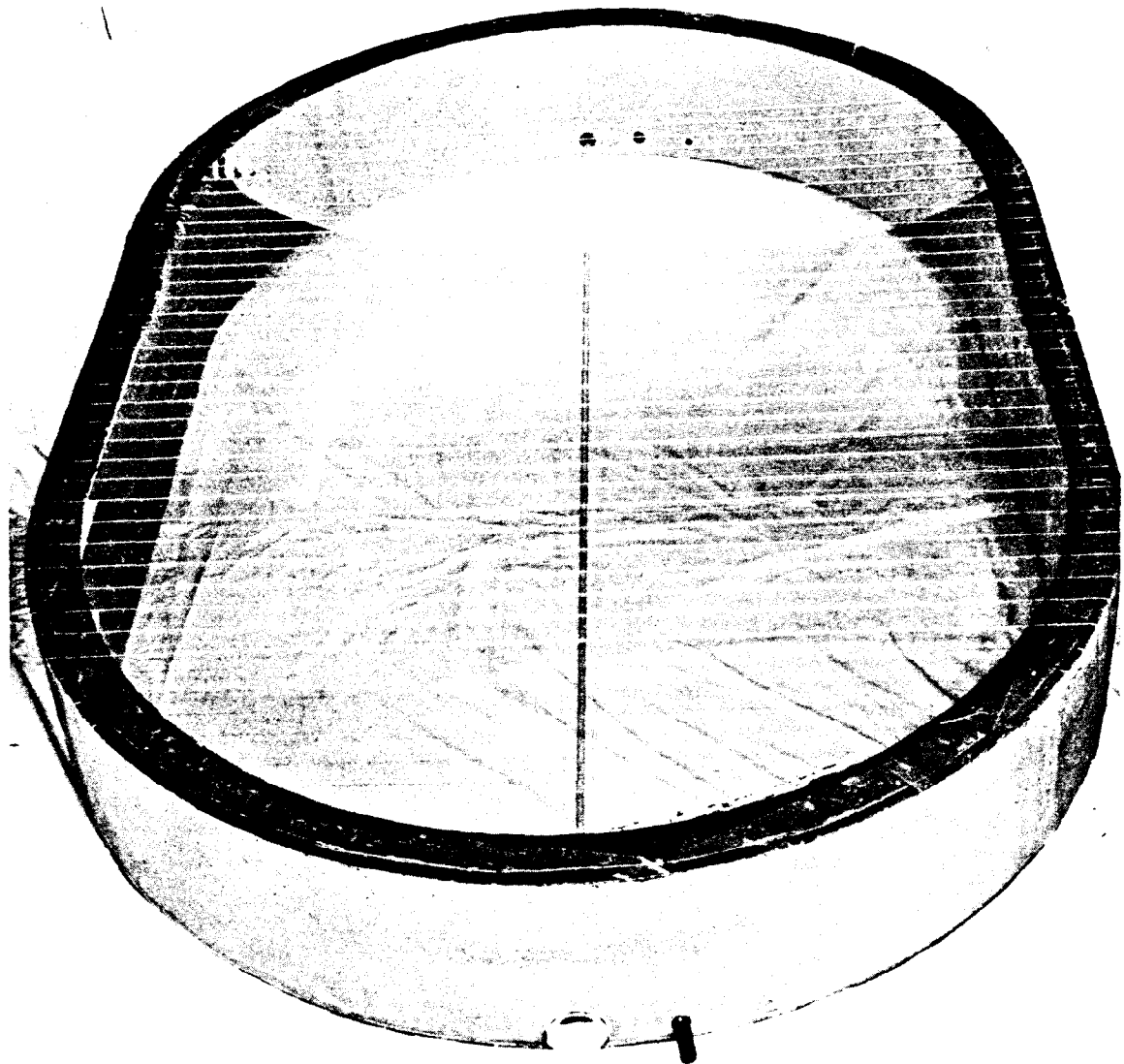
757A44

FIG. 39--The Blumlein and "elbow" used in shaping the 10-nsec, 600-kV pulse which drives the streamer chamber. The sheet metal which normally encloses the Blumlein and elbow has been largely removed for viewing. The vertical elements of the Blumlein taper outward and upward from the spark gap in such a way that the 23-ohm chamber impedance is everywhere matched and that the electrical paths leading from the gap to the chamber are as nearly equal in length as possible. When mounted in the oil tank with the Marx generator, the Blumlein is emersed in oil up to the point where the Blumlein and elbow are joined. At this point there is a large bulge in the center electrode of the elbow to compensate for the impedance change at the air-oil interface.



757A51

FIG. 40--Photograph of the streamer chamber installed in the magnet. The sheet metal rf enclosure at the downstream end of the chamber has been removed for viewing. The lucite supports for the central electrode as well as the carbon-rod terminating resistors are clearly visible. A corona guard encircles the central electrode to prevent breakdown at the edges. The electrode itself consists of 0.25-mm wires spaced 1 cm apart and supported on a 1/4-inch-thick aluminum window frame.



757A52

FIG. 41--Photograph of a foam cell used in the 2-meter streamer chamber. Each cell is 30 cm deep, 150 cm wide and about 230 cm long at the location of the target. Nylon fishline is used here to space the mylar windows away from individual electrode wires so that breakdown does not occur. In later models, 1/8-inch-diameter lucite rods are used in place of the nylon, and the spacing between the rods is increased to 6 inches. The hydrogen gas target is supported under tension by the lucite fixtures at each end. The target can be pressurized to about 60 psig to enhance the signal-to-background ratio for backgrounds not originating in the target.

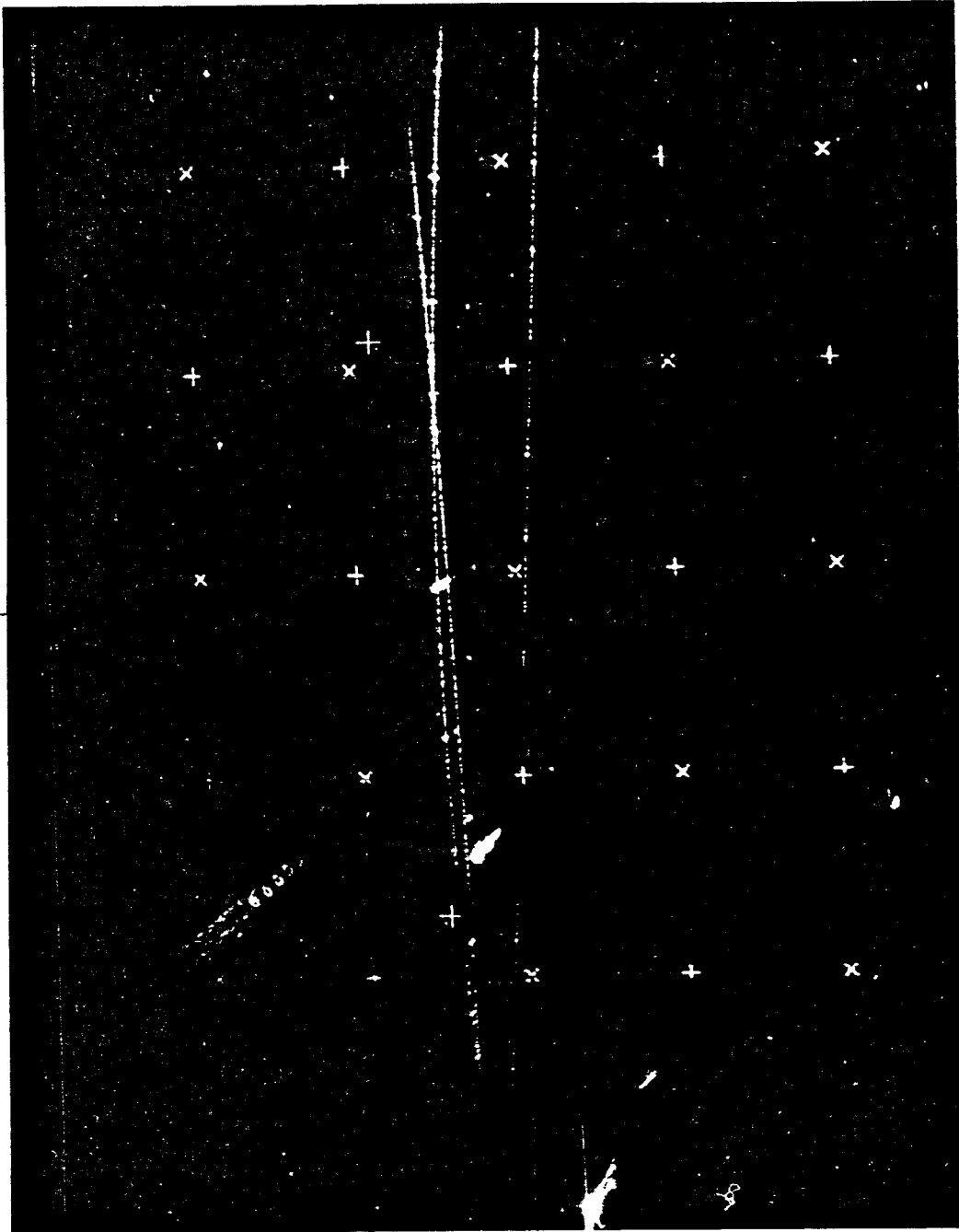
that its performance on our first preliminary run was excellent. Figures 42 and 43 give some indication of this.

Figure 42 shows a neutral particle, which we have identified kinematically as a K^0 , decaying within the sensitive volume of the chamber. A satisfactory χ^2 per degree of freedom was obtained when spatial errors of ± 0.4 mm in the horizontal streamer coordinates and ± 3 mm in the vertical streamer coordinate were assumed. Since the preliminary run was taken with the magnet powered to only 1/4 of its nominal current rating and since a precise mapping of the field was not carried out at this setting, the track reconstruction errors include uncertainties in the shape of the magnetic field. In this sense, the spatial errors assumed here represent upper limits on the ultimate resolution.

Figure 43 shows a nuclear interaction occurring within the hydrogen gas target. Five charged prongs can be seen leaving the vertex region, and a small-angle, neutral "V" decay, confirmed in two other views, is visible in the neon somewhat later. Four tracks can also be seen from an event (or events) occurring upstream of the sensitive volume. Under our operating conditions, the number of spurious tracks is generally small; in this respect our pictures will be rather cleaner than those usually obtained with bubble chambers. There is, of course, no obvious limit to the number of simultaneous tracks that can be observed. The bright flares which appear in Fig. 43 are due to breakdown where the mylar windows and neon-helium chamber gas are too close to the electrode wires. We hope to eliminate this problem completely before the photoproduction data runs begin.

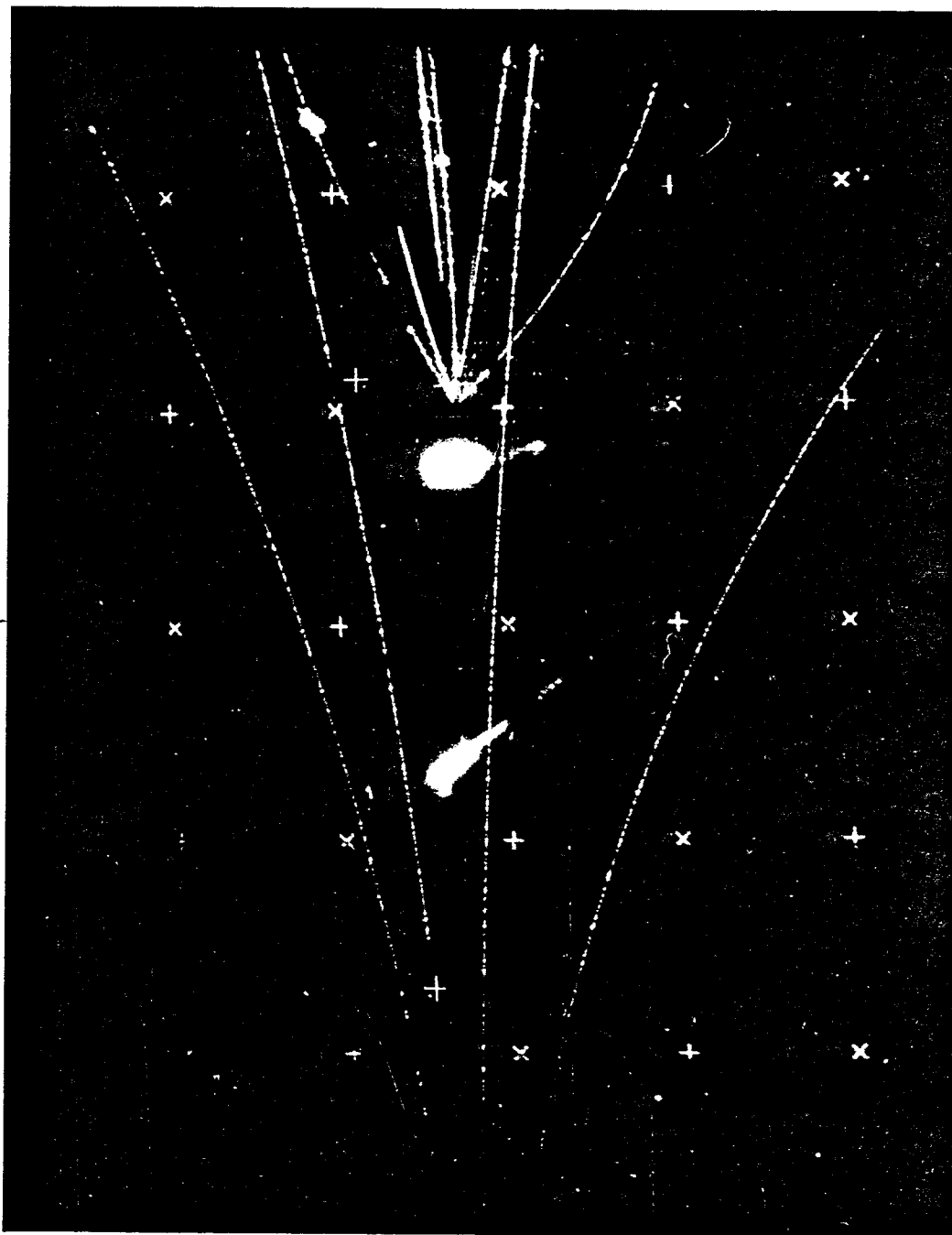
D. Speculation

In this section we have collected together various notes relating to possible future developments of streamer chambers. One point, which is clear immediately,



757A53

FIG. 42--A K^0 decay which occurred in the 2-meter streamer chamber during the first preliminary run in the photon beam.



757A54

FIG. 43--A nuclear interaction event which occurred in the streamer chamber during the first preliminary run in the photon beam.

is that there is no obvious limit to the dimensions which future chambers might have. The 1.3-MV, 800-joule Marx generator and Blumlein developed for the two-meter streamer chamber are by no means unusual in the field of high voltage engineering; in fact, quite the reverse is true. There is, for example, a commercial group* working in the field of flash x-rays, which has built a 10-MV Marx generator with a 0.35 MJ capacitor bank and a 10-MV Blumlein with a 50-ohm characteristic impedance.

Higher voltage ranges could also be used to drive large streamer chambers filled with hydrogen gas instead of with the neon-helium mixture or pure helium used normally. Streamers have been observed in hydrogen¹⁴ using image intensifiers and a 100-nsec pulse of 20 kV/cm ($E^2 \tau \approx 4 \times 10^4 \text{ (kV/cm)}^2 \text{ nsec}$). With a pulse of 10-nsec duration and about 65 kV/cm, direct photography of short streamers in hydrogen may be possible. [Figure 3 indicates that $\alpha_{\text{H}_2} (45 \text{ kV/cm}) \sim \alpha_{\text{Ne}} (18 \text{ kV/cm})$; thus the required voltage may be less than 65 kV/cm.] The critical regions outside the hydrogen volume would probably have to be immersed in SF₆ or some other gas to prevent breakdowns, since the breakdown voltages in hydrogen are similar to those in air and not much lower as in the case of neon-helium, but this limitation is not serious.

Another application for higher voltages would be in increasing the available light, thereby permitting lower demagnifications and higher resolution. The difficulty of producing pulses much shorter than 10 nsec is, however, considerable. Furthermore, there is no assurance that one will continue to gain in brightness by using pulses of much shorter duration and of much greater amplitude than have so far been tried. On the other hand, faster films are continually being developed; these may prove more helpful than future advances in pulse technology.

*Physics International, San Leandro, California.

We have mentioned already that it should be feasible to locate liquid hydrogen targets within or quite near to streamer chambers. The practice is, in fact, rather common in the case of spark chambers; it will no doubt become so in streamer chamber experiments when it is not essential to see the vertex and when higher interaction rates are needed than can be obtained with hydrogen gas.

We should mention two more speculative ideas for future streamer chambers. The first uses resonance scattering of light from metastable atomic states to view the tracks left by ionizing particles. This scheme may eliminate the need to pulse streamer chambers, and should provide quite high resolution. The second idea, which again we have not tried, would be to use the difference in the pulse velocity and particle velocity in a long chamber to measure time-of-flight. The pulse would be put onto the chamber just after the particles arrive, and tracks would be observed up to the point in space where the pulse overtakes the particles. Such chambers, driven as transmission lines, could be quite long without imposing any problems for the drive system. In practice the main difficulty would be in pulsing the chamber precisely in synchronism with the particle bursts from the accelerator.

To conclude on a practical note, we shall point out once more that very inexpensive streamer chambers and drive systems are possible, particularly for chambers of modest size. Capacitor-transformer systems, "toilet-roll generators," and small Marx generators can all be obtained for a few thousand dollars and are capable of producing pulses in the megavolt range. The chambers themselves are quite simple, and direct photography is possible. Thus, we see no reason that streamer chambers should not become almost as common and as widely used as ordinary spark chambers.

REFERENCES

1. S. Fukui and S. Miyamoto, *Nuovo Cimento* **11**, 113 (1959).
2. G. Charpak and L. Massonnet, *Rev. Sci. Instr.* **34**, 664 (1963).
3. A. I. Alikhanian, T. L. Asatiani, É. M. Matevosyan, and R. O. Sharkhatunian, *Phys. Letters* **4**, 295 (1963).
4. A. I. Alikhanian, T. L. Asatiani, and É. M. Matevosyan, *Soviet Phys. JETP* **17**, 522 (1963).
5. A. I. Alikhanian, *Loeb Lecture Notes, Harvard University, Cambridge, Massachusetts* (1965) (unpublished).
6. J. P. Garron, D. Grossman, and K. Strauch, *Rev. Sci. Instr.* **36**, 264 (1965).
7. R. C. Catura and K. W. Chen, *Nucl. Instr. and Methods* **36**, 317 (1965).
8. L. P. Keller, R. A. Schluter, and T. O. White, *Nucl. Instr. and Methods* **41**, 309 (1966).
9. V. A. Mikhailov, V. N. Roinishvili, and G. E. Chikovani, *Soviet Phys. JETP* **18**, 561 (1964).
10. G. E. Chikovani, V. N. Roinishvili, and V. A. Mikhailov, *Soviet Phys. JETP* **19**, 833 (1964).
11. B. A. Dolgoshein and B. I. Luchkov, *Soviet Phys. JETP* **19**, 266 (1964).
12. G. E. Chikovani, V. N. Roinishvili, V. A. Mikhailov, and A. K. Javrishvili, *Preprint, Institute of Physics of the Academy of Science of Georgian SSR, Tbilisi* (1964).
13. B. A. Dolgoshein, B. I. Luchkov, and B. U. Rodionov, *Soviet Phys. JETP* **19**, 1315 (1964).
14. V. I. Komarov and O. V. Savchenko, *Nucl. Instr. and Methods* **34**, 289 (1965).

15. E. Gygi and F. Schneider, "A Spark Chamber of Three-Dimensional Resolution," Proceedings of the Informal Meeting on Film-Less Spark Chamber Techniques and Associated Computer Use, p. 351-60 (published as CERN-64-30); and S. Fukui, "On the Spark Formation in the Spark Chamber," 1963 NPA Seminar, the Neutrino Experiment, p. 145-162 (Published as CERN-63-37).
16. F. Bulos, "Streamer Wide Gap Spark Chamber," SLAC Internal Report TN-64-73, Stanford Linear Accelerator Center, Stanford, California (1964).
17. F. Bulos, A. Boyarski, R. Diebold, A. Odian, B. Richter, and F. Villa, IEEE Trans. Nucl. Sci. NS-12 (No. 4), 22 (1965).
18. F. Bulos, A. Boyarski, R. Diebold, A. Odian, B. Richter, and F. Villa, "Streamer Chamber Development," Proceedings of the 5th International Conference on High Energy Accelerators, Frascati, Italy, September 9-16, 1965, p. 675.
19. A. Odian, "Streamer Chamber Developments at SLAC," Proceedings of the 1966 International Conference on Instrumentation for High Energy Physics, Stanford Linear Accelerator Center, Stanford, California, September 9-10, 1966; p. 49.
20. J. S. Townsend, Electricity in Gases (Oxford University Press, Oxford, 1914).
21. L. B. Loeb, Fundamental Processes of Electrical Discharge in Gases (Wiley and Sons, New York, 1939).
22. L. B. Loeb and J. Meek, The Mechanism of the Electric Spark (Stanford University Press, Stanford, California, 1941).
23. R. C. Fletcher, Phys. Rev. 76, 1501 (1949).
24. F. R. Dickey, Jr., J. Appl. Phys. 23, 1336 (1952).
25. J. M. Meek and J. D. Craggs. Electrical Breakdown of Gases (Clarendon Press, Oxford, 1953).
26. L. B. Loeb, Basic Processes of Gaseous Electronics (University of California Press, Berkeley, 1955).
27. J. Fischer and G. T. Zorn, Rev. Sci. Instr. 32, 499 (1961).

28. J. K. Wright, Proc. Roy. Soc. 280A, 23 (1963).
29. H. Raether, Electron Avalanches and Breakdown in Gases (Butterworths, London, 1964).
30. H. Raether, Z. Physik 112, 464 (1939).
31. J. M. Meek, Phys. Rev. 57, 722 (1940).
32. H. Raether, Z. Physik 117, 375, 524 (1941); Arch. Elektrotech. 34, 49 (1940).
33. See, for example, Table 3.6 of Ref. 29.
34. Figure 2 is replotted from Fig. 2.34 of Ref. 29.
35. Figure 3 is plotted from Tables 8.6 and 8.8 of Ref. 26.
36. This is supported by the work of G. E. Chikovani, V. N. Roinishvili, and V. A. Mikhailov, Nucl. Instr. and Methods 29, 261 (1964).
37. T. L. Asatiani, K. A. Gazarian, V. N. Zhmirov, É. M. Matevosyan, A. A. Nazarian, and R. O. Sharkhatunian, "Ionization Measurement in a Streamer Chamber," Report JINR-E-2324, Joint Institute for Nuclear Research, Dubna (1965).
38. R. L. Gluckstern, Nucl. Instr. and Methods 24, 381 (1963).
39. G. Charpak, L. Massonnet, and J. Favier, Progress in Nuclear Techniques and Instrumentation (North Holland Publishing Co., Amsterdam) 1, 321 (1965).
40. Similar tests with delayed pulses were carried out by G. E. Chikovani, et al., who found an increase from 1.4 to 2.8 streamers/cm with delays up to 200 μ sec. A reference to this work is given by G. Charpak, et al., Ref. 39.
41. Similar tests at reduced pressure were carried out by B. A. Dolgoshein, et al., Ref. 13, who found that the number of streamers/cm decreased with decreasing pressure only at pressures below 300 torr. A reference to this work is also given by G. Charpak, et al., Ref. 39.

42. For a recent review of automatic scanning and measuring systems, see the Round Table Discussion on Data Analysis in the Proceedings of the 1966 International Conference on Instrumentation for High Energy Physics, Stanford Linear Accelerator Center, Stanford, California, September 9-10, 1966; pp. 269-362.
43. J. D. Craggs and J. M. Meek, High Voltage Laboratory Technique, (Butterworths, London, 1954).
44. Handbook of Chemistry and Physics, 44th Edition (Chemical Rubber Publishing Company, Cleveland, Ohio, 1962); pp. 3391-3401.
45. E. Marx, Deutsches Reichspatent No. 455933; E. Marx, *Elektrotech. Z.* 45, 652 (1924).
46. E. Gygi and F. Schneider, "A Nanosecond Pulse Generator of 200 kV Amplitude," CERN Report 64-46, CERN, Geneva (1964).
47. J. C. Martin and I. Smith, private communication.
48. R. A. Fitch and V. T. S. Howell, *Proc. Inst. Elect. Engrs.* 111, 849 (1964).
49. Blumlein "voltage-doubler circuits" are discussed by O. L. Ratsey, *J. Inst. Elect. Engrs.* 93, 245 (1946); by K. J. R. Wilkinson, *J. Inst. Elect. Engrs.* 93, 1090 (1946); and by Craggs and Meek, Ref. 43. See also J. L. Brewster, F. M. Charbonnier, L. F. Garrett, K. W. Riegelmann, and J. K. Trolan, "Design Studies for Ultra-Fast, Low-Impedance, High-Peak-Power Pulsed Systems," Technical Report No. AFWL-TR-65-21, Air Force Weapons Laboratory, Kirkland Air Force Base, N. M. (1965).
50. F. Schneider, private communication.
51. G. E. Chikovani, V. A. Mikhailov, and V. N. Roinishvili, *Phys. Letters* 6, 254 (1963).
52. D. Yount, "A High Precision Faraday Cup and Quantameter for SLAC," *Nucl. Instr. and Methods* 52, 1 (1967).

APPENDIX A

HIGH VOLTAGE PROPERTIES OF MATERIALS

The data on the high voltage properties of materials are scattered in a wide variety of publications. They consist usually of measurements of the so-called intrinsic breakdown, i. e. , of the maximum breakdown voltage of a highly selected small sample of material or of a given material with industrial specifications. Almost all of the data for materials of high dielectric strength are quoted without specifying the thickness of the sample tested; whenever the gap is specified, it is no larger than about 1 cm. Volume dependence is rarely even considered.

For liquids the situation is even more obscure, because the breakdown under dc conditions depends upon the purity of the sample, upon any prior outgassing of the sample, upon the nature of the electrodes, etc. Fortunately, the situation is somewhat better for gases than for liquids or solids, both from the experimental and the theoretical points of view.

The high voltage properties given in the following paragraphs of this Appendix provide only rather crude guidelines for designing high voltage systems. The best we can say about these data is that whenever we have used them we were never badly wrong. While solids, liquids, and gases can be used either as insulators or as switch materials, our discussion of the latter application is brief.

The conditions and mechanisms for breakdown in gases are discussed in some detail in the chapter on streamer theory and experiment, and a number of references are given there. For pure gases, clean electrodes, and reproducible laboratory conditions, the dc breakdown voltage can usually be predicted within a few percent. The data of Kusko^{1(*)} for a variety of gases and for a 0.5-inch uniform gap between both stainless steel and aluminum electrodes are shown in Fig. A. 1. The time

* Appendix references are listed at the end of each Appendix.

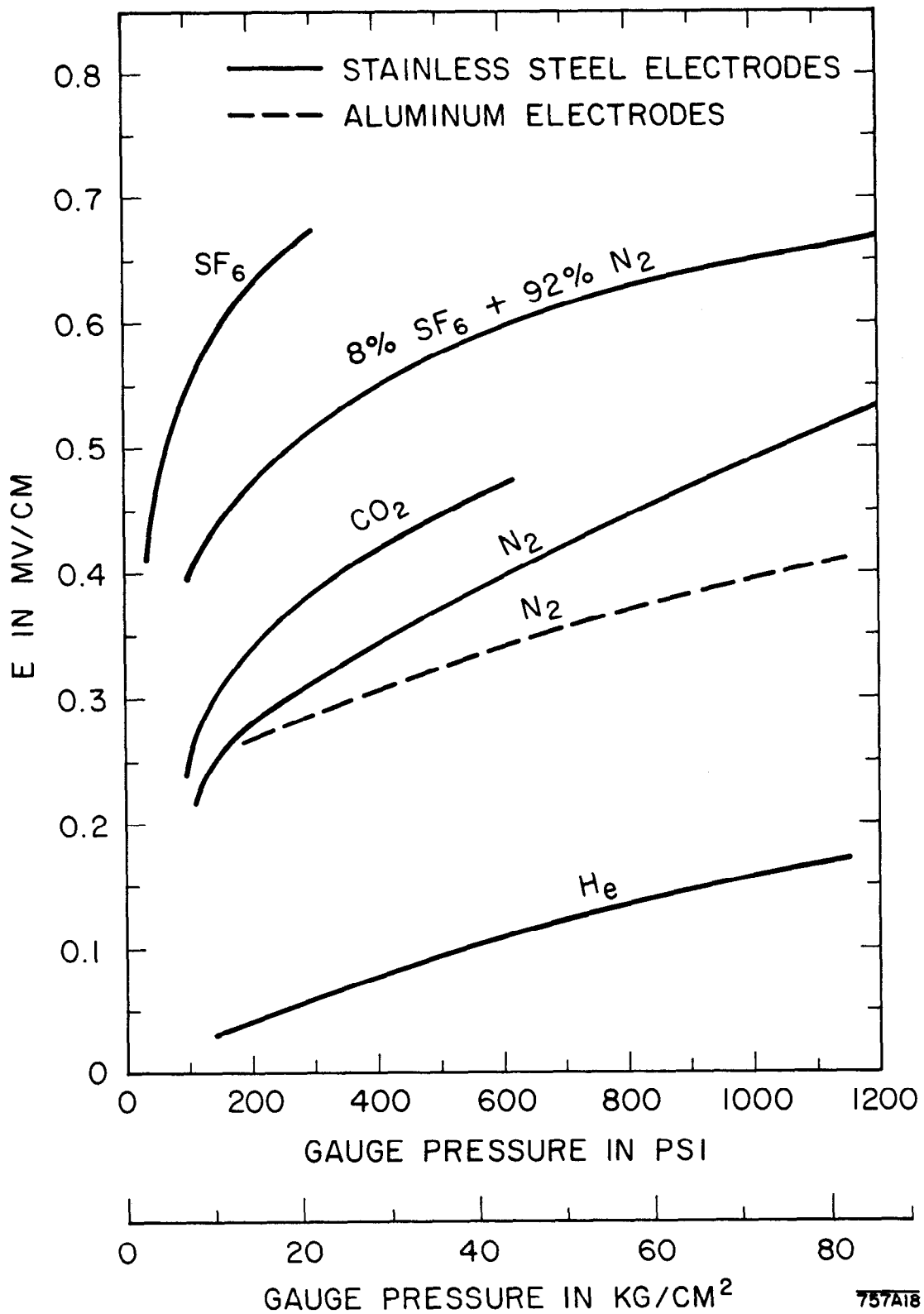


FIG. A.1--DC electric field for breakdown in several gases versus the gas pressure. This figure was obtained originally by A. Kusko and has been recopied from Fig. 2 of the article by J. G. Trump, Ref. 1.

dependence of the breakdown is also beginning to be understood, at least it is being measured with some accuracy. The data of Felsenthal and Proud² are shown in Fig. A.2 for several gases of interest here. The time dependence for gases is rapid only for very short times or for very low pressures. Fluctuations in the breakdown time are discussed by Ependiev³ and by Fletcher⁴ as well as by Felsenthal and Proud.

The most striking features of voltage breakdown in liquids are the rapid variation with time in the microsecond region and the fact that in this region the breakdown is practically independent of the concentration of impurities. These features are associated with the observation (e. g. , by means of high-speed photography) that the breakdown in a liquid does not occur until a gas channel connects the two electrodes. This channel is produced by an electrostatic shock wave similar to that at the tip of an avalanche in gases, but the speed of propagation is relatively slow. The exact mechanism that initiates the gas channel is not known.

The unpublished data of J. C. Martin and I. Smith⁵ on high voltage pulse breakdown in liquids can be summarized by means of the relationship

$$E^m t^n = k g^p \quad (A-1)$$

where E is the electric field in MV/cm, t is the effective time in μsec (i. e. , the time during which the pulse is greater than 63% of the peak voltage), g is the electrode gap in cm, and k is a slowly decreasing function of the area of the electrodes. The exponents m , n , and p are constants to be determined experimentally. The unpublished data of Martin and Smith with transformer oil have been fit reasonably well by the expression

$$E t^{1/2} = k g^{1/4} \quad (\text{transformer oil}) \quad (A-2)$$

where k is in the range from 0.4 to 0.2 for plate areas of from 6 to 1500 cm^2 .

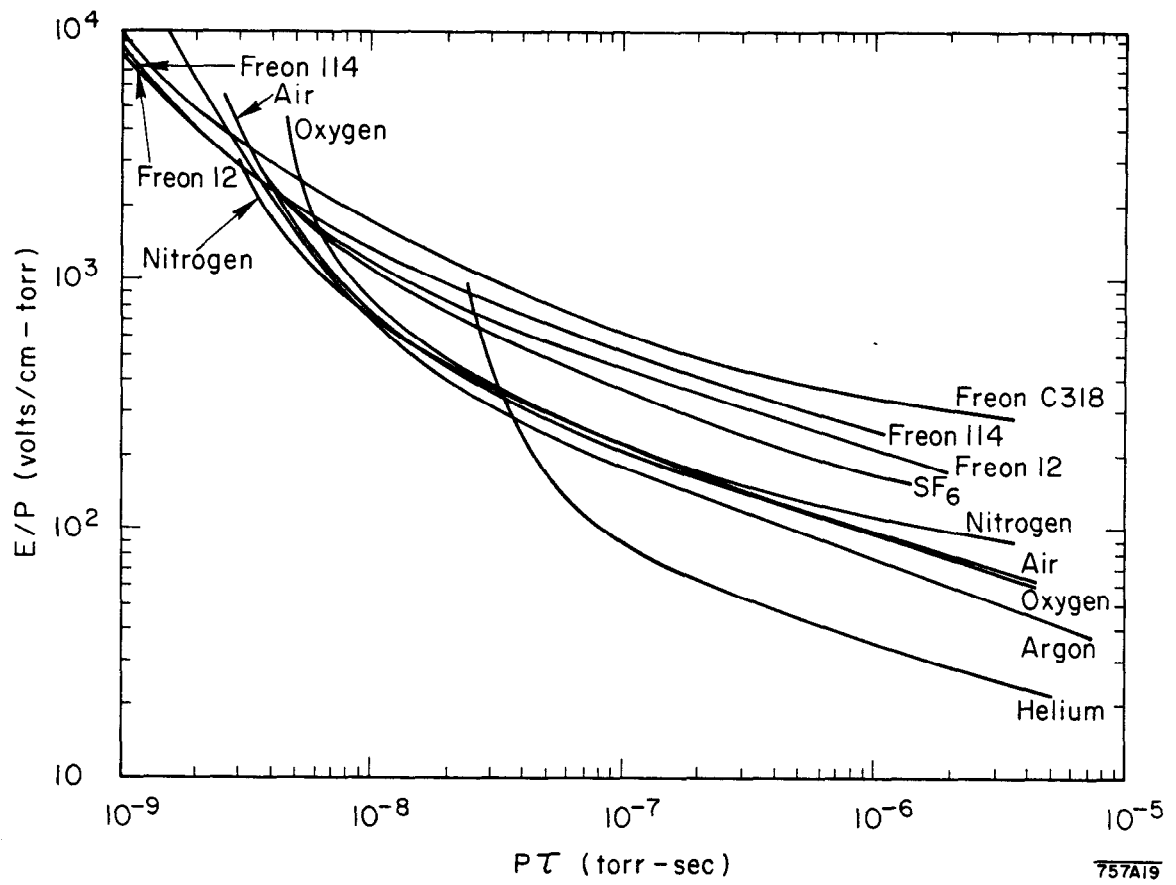


FIG. A. 2--Breakdown electric field versus pulse duration for several gases.
 This figure was recopied from the article by P. Felsenthal and
 J. M. Proud.

Their results for 0.2-, 0.5-, and 1.0-cm plate spacing in oil are plotted in Fig. A.3. Since $E = V/g$, where V is the total voltage, Eq. (A-2) indicates that the breakdown voltage increases as $g^{5/4}$, i. e., slightly faster than linearly. Notice that for pulses of less than 1- μ sec duration, the breakdown voltage is an order of magnitude higher than for dc. Liquids are therefore ideal insulators in pulsed high voltage systems.

The data of Martin and Smith for deionized water seem to satisfy the expression

$$Et^{1/3} = k. \quad (A-3)$$

Thus the exponent of g is negligible in this case, although the dependence of k upon the electrode area is still significant. As indicated in Fig. A.4, k decreases from about 0.3 at 0.1 cm^2 to about 0.15 at 1000 cm^2 . The typical scatter of these measurements is 10-20%. Systematic errors in pulse monitoring are believed to be of the same order.

The unpublished data of Martin and Smith⁵ for a number of liquids are summarized in Table A-I by means of the relationship

$$E^{3/2} t = k. \quad (A-4)$$

In addition to the value of k with errors of 10-15%, the table gives the dielectric constant ϵ relative to vacuum and the product $\epsilon k^{4/3} \propto \epsilon E^2$, which is proportional to the maximum electromagnetic energy density in the medium.

The breakdown in solids does not exhibit the strong time dependence observed in liquids, at least not in the region above about 10^{-8} sec. Data on the dc breakdown voltage are very erratic, and there are so many parameters influencing the result that we feel that the best way of choosing the thickness of a solid insulator is to try it. In some experiments, for example, the breakdown voltage observed in lucite is as high as 12 MV/inch with negligible volume dependence. On the other

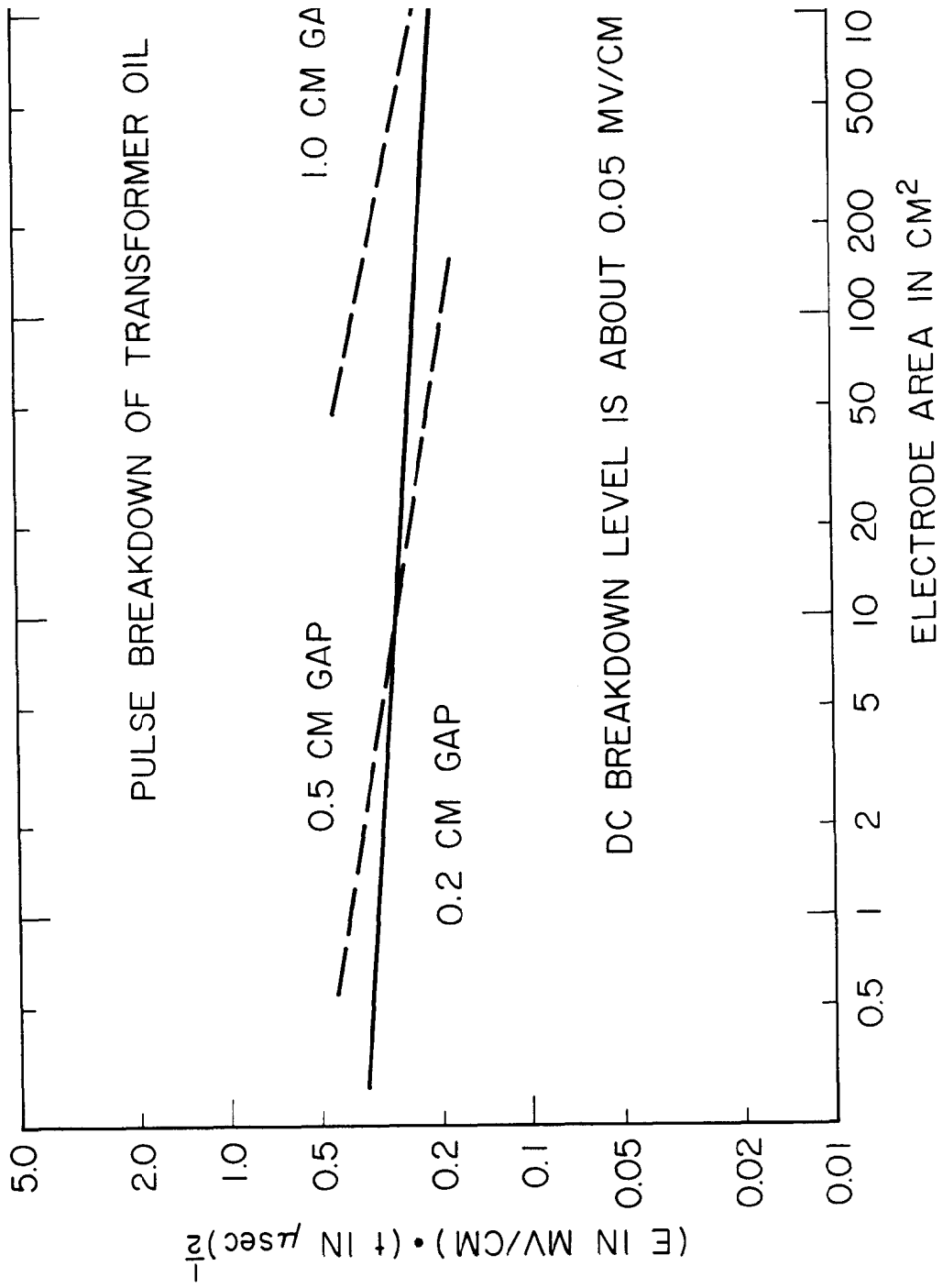


FIG. A. 3--Electric field for pulse breakdown in transformer oil versus the electrode area. The communicated to us by J. C. Martin and I. Smith of AWRE.

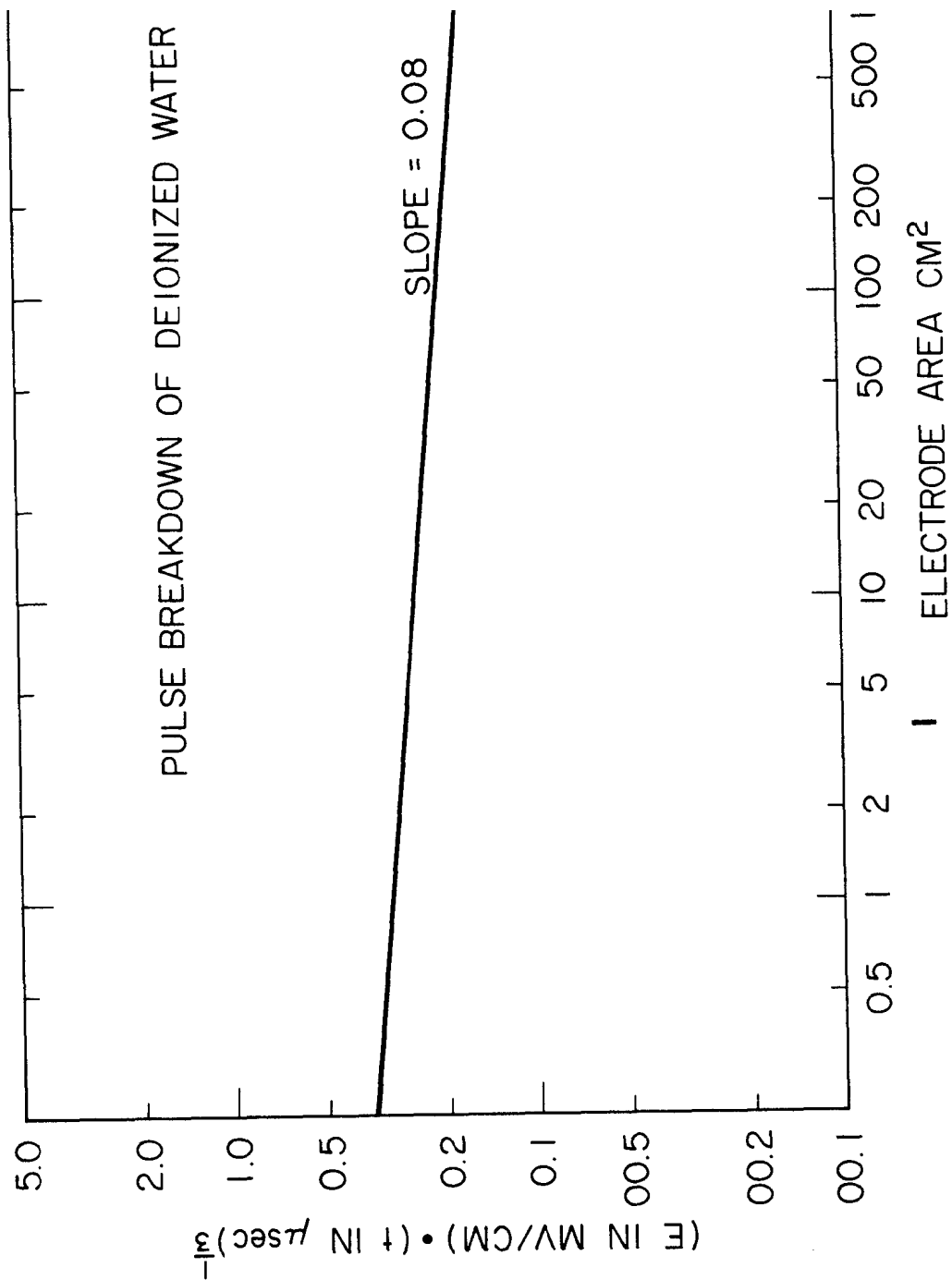


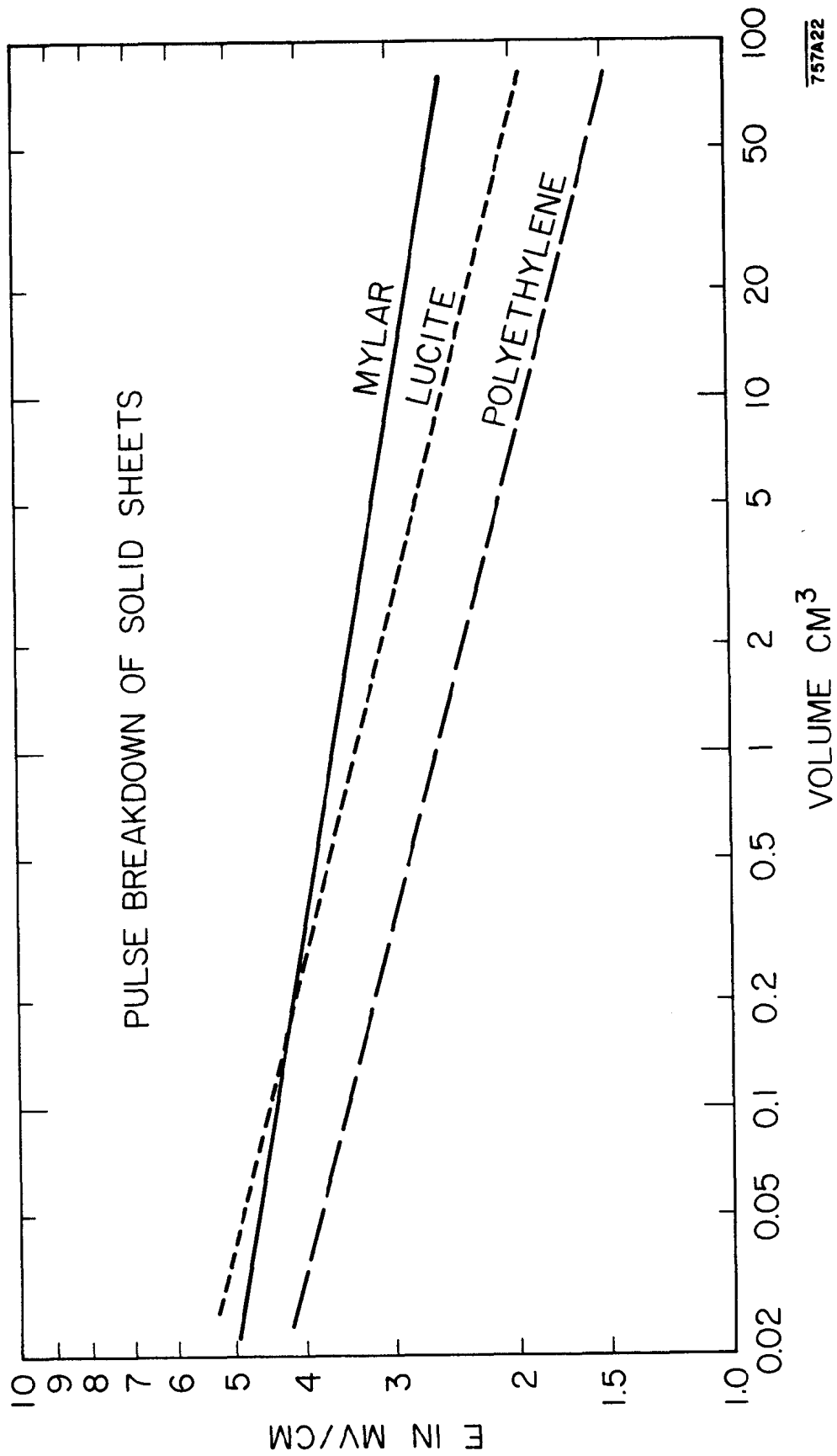
FIG. A. 4--Electric field for pulse breakdown in deionized water versus the electrode area. The data were communicated to us by J. C. Martin and I. Smith of AWRE.

hand, we have punctured through lucite 1.5 inches thick with a series of 200-nsec pulses of about 400 kV/inch, i. e. , with a field a factor of 30 smaller than 12 MV/inch. In addition, we have found other evidence of fatigue in solids under electric stress.

High-voltage, single-shot impulse breakdown through thin sheets of material has been studied by Martin and Smith⁵ and some of their unpublished results for mylar, lucite, and polyethylene are plotted in Fig. A.5 as a function of the sample volume. These data for solid dielectrics are equivalent to dc breakdown measurements.

TABLE A-I

Material	$k = E^{3/2} t$	ϵ	$\epsilon k^{4/3} \propto \epsilon E^2$
Ethyl alcohol	0.057	24	
Ethyl alcohol + 1% water	0.059	24.6	0.56
Ethyl alcohol + 10% water	0.052	29.6	
Methyl alcohol	0.052	33	0.65
Ethylene glycol	0.03	38	0.34
Glycerine	0.010	44	0.10
Castor oil	0.11	4.7	0.25
Transformer oil	0.08	2.4	0.09
Water	0.03	80	0.72



757A22

FIG. A. 5--Electric field for pulse breakdown in thin sheets of mylar, lucite, and polyethylene versus the sample volume in cm³. These are unpublished data communicated to us by J. C. Martin and I. Smith of AWRE.

REFERENCES

1. A.Kusko, "Electrical Behavior of Gases at High Pressure," Electrical Engineering Doctorate Thesis, Massachusetts Institute of Technology, Cambridge, Massachusetts (1951). Our figure is redrawn from Fig. 2 of the article by J. G. Trump, Proceedings of the International Conference held at the Central Electricity Research Laboratories, Leatherhead, Surrey, England, 7-11 May, 1962; pp 348-356.
2. P. Felsenthal and J. M. Proud, "Nanosecond Pulse Breakdown in Gases," Technical Report No. RADC-TR-65-142, Rome Air Development Center, Griffiss AFB, New York (1965).
3. E. Z. Ependiev, "An Investigation of Pulse Breakdown in Gases," Zh. Teekh. Fiz. 27, 1010 (1957).
4. R. C. Fletcher, Phys. Rev. 76, 1501 (1949).
5. J. C. Martin and I. Smith, private communication.

APPENDIX B

HIGH VOLTAGE SWITCH TECHNOLOGY

A real switch can be described as an ideal switch in series with a constant inductance and a time-dependent resistance and in parallel with a capacitance. This is illustrated in Fig. B.1a. Very fast, high voltage, high current switches are always based on some kind of disruptive discharge in an insulating material, be it solid, liquid or gas. The parasitic inductance and the resistance are usually due to two factors: the electrode structure, which is time-independent and calculable from the geometry; and the actual discharge mechanism, which develops with time.

Gas switches or spark gaps are better known and more widely used than solid or liquid switches, and probably they are more versatile. They can be triggered in many ways and at high repetition rates (rates of 1 kc have been reported), and their inductance and resistance can be kept at reasonably low values provided that sufficient care is devoted to the construction.

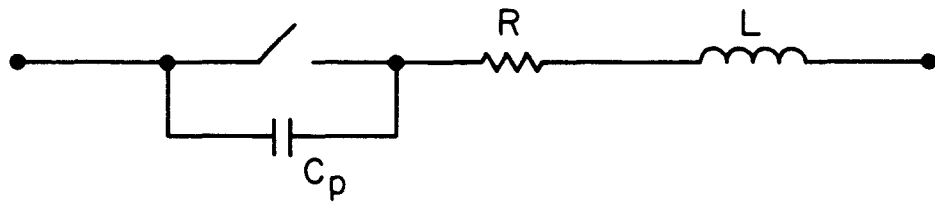
From calculations and experiments, Martin and Smith¹ of AWRE have obtained the following expression for the duration of the time-dependent resistance in gas spark gaps across striplines:

$$\tau_R = \frac{88}{Z^{1/3} E^{4/3}} \left(\frac{\rho}{\rho_0} \right)^{1/2} \text{ nsec} \quad (\text{B-1})$$

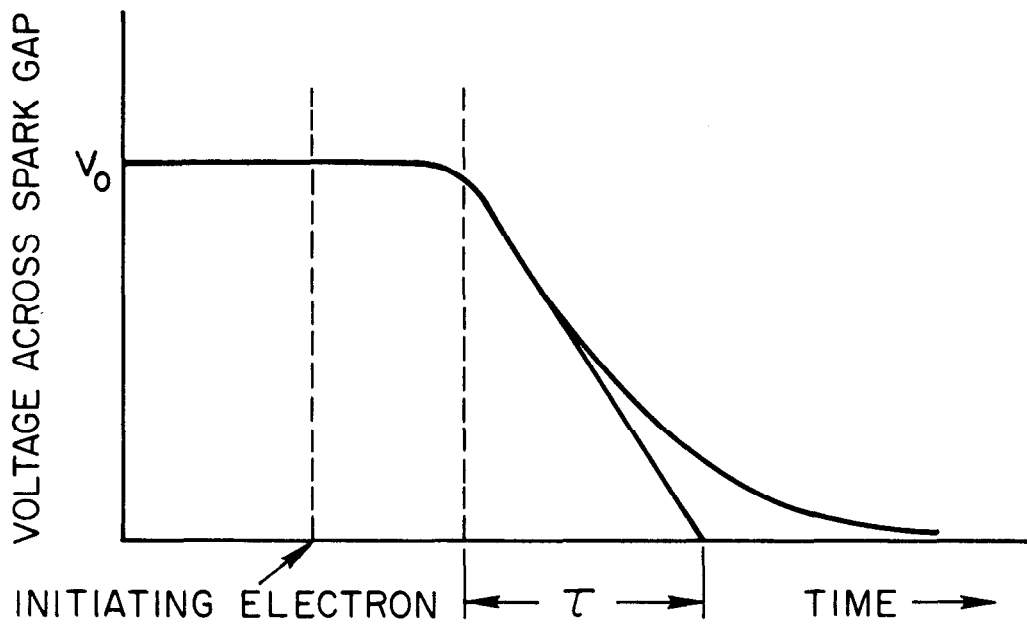
where Z is the impedance of the driving channel in ohms, E is the electric field in units of 10 kV/cm, ρ is the density of the gas, and ρ_0 is the density of air at normal temperature and pressure. This expression has been checked experimentally to an accuracy of about 10%, and the agreement is reasonable.

The characteristic time associated with the inductance in gas spark gaps is given by

$$\tau_L = L/Z \quad (\text{B-2})$$



a.



b.

757A24

FIG. B.1--Switch equivalent circuit (a) and the time dependence of the voltage across a triggered gap (b).

where L is the total inductance of the spark and the leads, and where Z is again the impedance of the source. The inductances of the spark and of the leads can be estimated from the formulas

$$L_{\text{spark}} = 2 l_{\text{spark}} \ln \frac{r_2}{r_1} \text{ nH} , \quad (\text{B-3a})$$

$$L_{\text{leads}} = 2 l_{\text{leads}} \ln \frac{r_2}{r_3} \text{ nH} \quad (\text{B-3b})$$

where l_{spark} and l_{leads} are the lengths in cm of the spark and the leads, where $r_1 \approx 0.05$ mm is the radius of the spark and r_3 the average radius of the leads, and where r_2 is roughly half the width of the stripline feeding the spark gap.

The complete time dependence τ , sketched in Fig. B. 1b, is the sum of τ_R and τ_L . (The rise time is 2.2τ .) Additional terms should be included to take into account the finite time required for a wave originating at the gap to reach the lateral boundaries of the stripline. (These last terms, as well as τ_L , dictate the tapered geometry chosen for the Blumlein which drives the two-meter streamer chamber.)

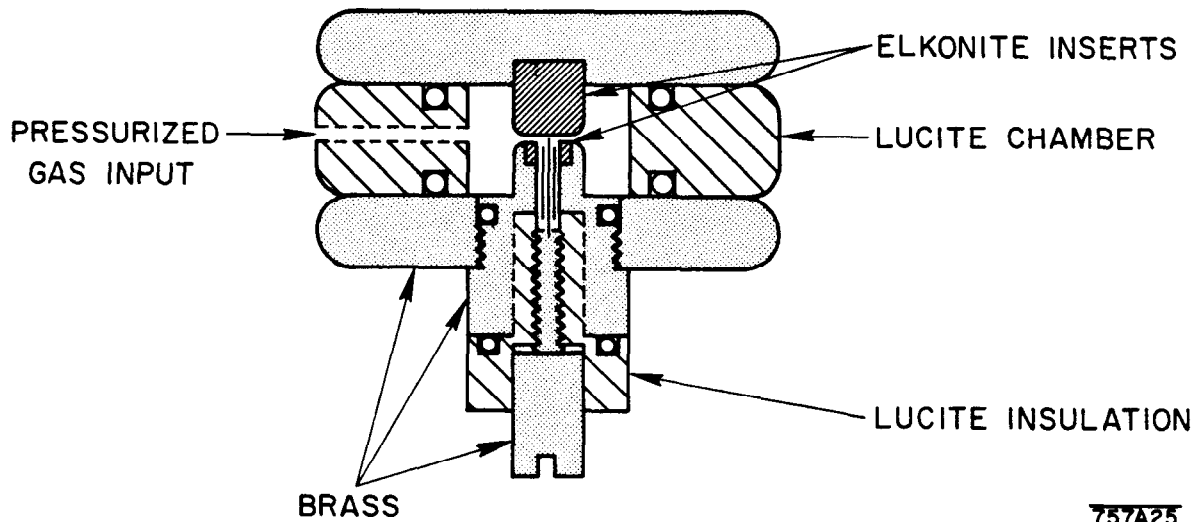
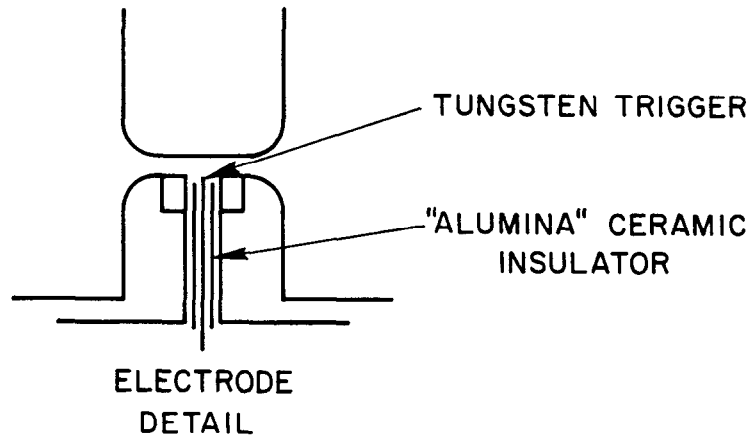
When the spark channel is formed across a transmission line, the voltage fall is more or less exponential until the value has dropped a decade or so at which point nearly all of the prompt energy has been delivered. The energy dissipated in the spark gap is $V^2 \tau_R / Z$, so that gaps having a fast rise time do not show much pitting. In pulse-forming applications, the expression for τ is particularly useful in estimating the contribution of the spark gap to the rise time of the output pulse. Additional data on spark gaps are reported in Refs. 2, 3 and 4.

In general we have used Elkonite (80% W - 20% Cu) electrodes or brass electrodes with Elkonite inserts where the discharge actually occurs. In the case of

triggered gaps, we have usually located the third electrode at the center of one of the discharge electrodes (trigatron), insulating it from the discharge electrode with a tubular alumina (a ceramic) insert. The electrode surface can either be flat with rounded edges or completely rounded and locally spherical. An example is shown in Fig. B.2.

In the 600-kV Blumlein spark gap, which fires because of overvoltage rather than a trigger pulse, the gap is 1.5 cm between locally spherical Elkonite electrodes of 5-cm cylindrical diameter. The electrode tips are cut on a 5-cm radius. The cylindrical lucite pressure vessel has an inside diameter and inside vertical clearance of about 8 cm, hollowed out from a single solid piece. Thus the inside height of the vessel is more than 5 times the gap separation, while the inside diameter clears the edges at the electrodes by 1.5 cm, or about one gap separation. The gas input is through the bottom electrode to avoid any discontinuities in the lucite dielectric of the pressure vessel. The electrode-to-lucite seals are made with O-Rings, and the operating pressure is typically 50 psig of SF₆.

The most commonly used gas in sealed spark gaps is nitrogen. We have found, however, that nitrogen gives a somewhat erratic dc breakdown characteristic in high current switches such as those in Marx generators; we believe this to be due to the formation of nitric oxides which have a different breakdown voltage than pure nitrogen. The effect can be eliminated by flowing the gas or by using a different gas such as CO₂. The breakdown voltage is about 25% lower for CO₂, so that a slightly higher pressure is required for the same operating voltage. For very high voltage switches, high dielectric strength gases are required; otherwise the pressures are prohibitive. We have found that SF₆ with a dielectric strength of about 90 kV/cm at normal temperature and pressure (e. g. , about 3 times larger than air and 4 times larger than N₂) is well suited for this purpose. It



757A25

FIG. B. 2--Schematic drawing of a triggered spark gap. The trigger needle is located at the center of the lower electrode, and its penetration into the gap can be adjusted by turning the larger threaded shaft to which the needle is attached. A cylindrical ceramic insulator is imbedded in the lucite which surrounds the threaded shaft, and it is used to isolate the trigger needle as it passes through the lower electrode.

does release fluorine under the action of the spark, but we have not observed any appreciable corrosion in our SF₆ switches, even after 20,000 or more pulses. In all gases we have tried (namely SF₆, N₂, and CO₂) we have found a breakdown voltage instability above about 600 kV/cm. The effect is to limit the use of high pressure in reducing the size of a spark gap.

The unpublished data of Martin and Smith¹ for the duration of the time-dependent resistance in a solid polyethylene spark gap are fit reasonably well by the expression

$$\tau_R = \frac{5}{Z^{1/3} E^{4/3}} \text{ nsec} \quad (\text{B-2})$$

where E is now in MV/cm and Z is again the impedance of the driving channel in ohms. This expression agrees surprisingly well with the observations for gas gaps when the value of ρ for polyethylene is inserted, and it indicates, along with the high dielectric strength and small electrode spacing, that the resistance and inductance of solid gaps can be quite low. Similarly, the parasitic capacity of solid dielectric gaps is normally relatively high.

Solid dielectric switches can be triggered mechanically (by puncturing the insulator), electrically, or by overvoltage. The overvoltage and mechanical triggers have long delays and large jitter, while the electrical trigger requires a voltage of as much as 50% of the holding voltage. The repetition rate is low in all cases since the dielectric has to be changed after each pulse. We have used the solid dielectric switches in the primary of high voltage autotransformers, a single-shot application in which the repetition rate was not important but in which a low input inductance was required. (Autotransformers are discussed in Appendix C.)

Liquid and solid dielectric switches are similar in that both have low resistance and inductance. They differ in that liquid switches can be used reliably only

under pulse conditions where the firing voltage is stable. We have sometimes used liquid switches to trigger Blumleins or to short the outputs of Marx generators, but our experience is meager. We have not used them in the final system since the noise and shock are ear-shattering, and since liquid switches exhibit serious electrode wear which might limit the reliability in our application. A detailed study of different liquids suitable for switches has been reported by Felsenthal and Proud.⁵

REFERENCES

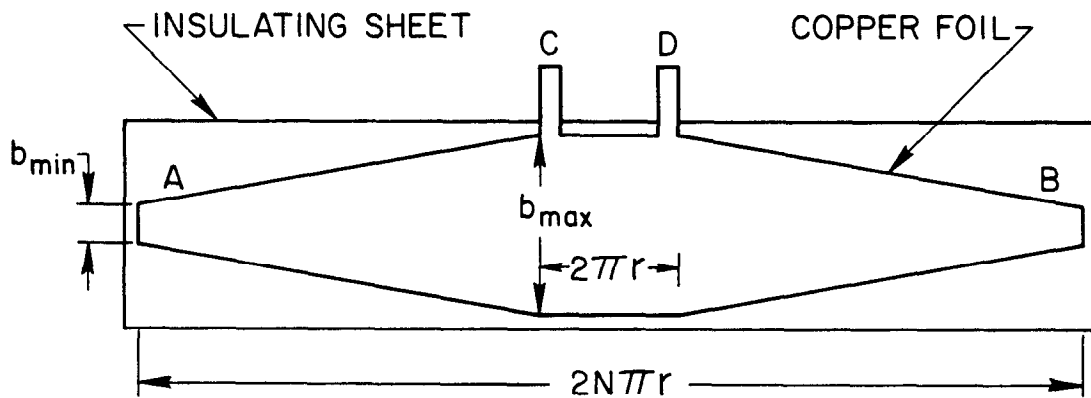
1. J. C. Martin and I. Smith, private communication.
2. V. V. Kremnev and G. A. Mesyats, "Effect of Interelectrode Capacity in a Spark Gap on the Slope of the Pulse Front," *Instruments and Experimental Techniques* 1, 120 (1966).
3. W. Weizel and R. Rompe, *Zeit. F. Phys.* 122, 9-12, 636 (1944).
4. B. J. Elliot, M. L. Report No. 1059, Microwave Laboratory, Stanford University, Stanford, California (1963).
5. P. Felsenthal and J. M. Proud, "Nanosecond Switch Development," Technical Report No. AFWL-TR-65-119 AD 474653 Air Force Weapons Laboratory, Kirkland AFB, New Mexico (1965).

APPENDIX C
AUTOTRANSFORMERS

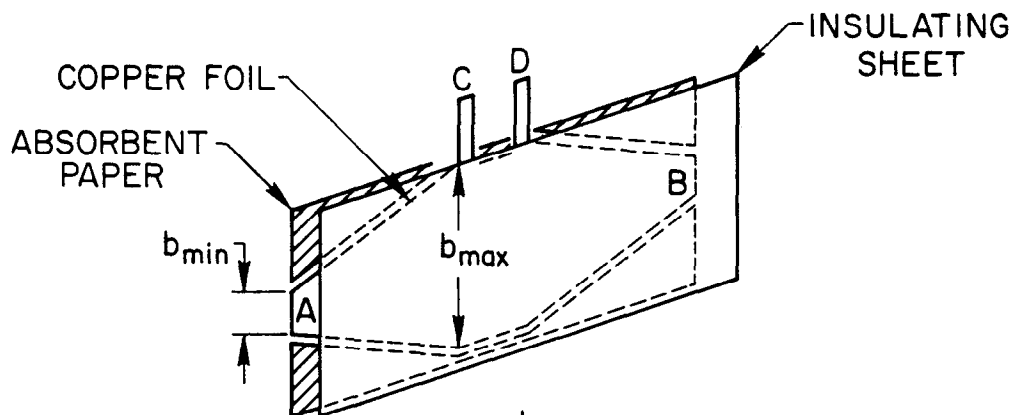
The autotransformer designed by J. C. Martin and I. Smith¹ is shown schematically in Figs. C.1 a, b, c, d. It consists of 0.002- to 0.005-inch copper foil cut to the shape indicated in Fig. C.1a and attached to a sheet of polyethylene or mylar insulation. As indicated in Fig. C.1b absorbent (toilet) paper of about the same thickness as the copper is inserted around the edges of the copper to fill the remaining space. The sandwich is then wound on an insulating cylinder (e.g., a cylinder made of lucite) which has an outer radius and length appropriate for the particular transformer being constructed. As indicated in Figs. C.1c and C.1d, a second insulating cylinder is added after the winding is completed, and the two cylinders are sealed at the bottom by an insulating plate. The result is put into an evacuated chamber for several hours and is then vacuum impregnated with copper sulfate solution which has previously been outgassed. The copper sulfate* has the important function of distributing the field smoothly at the edges of the copper winding so that breakdown through the insulating sheets does not occur. The tapered windings are intended to optimize the flux linkage from primary to secondary.

The arrangement used for generating a high voltage pulse is shown in Fig. C.2a. The primary inputs of the transformer (C and D of Figs. C.1a-d) are connected across a capacitor C_{prim} at a voltage V_{in} by closing a switch S. The outputs of the secondary, A and B, are applied to the load C_{sec} , which might, for example, be a Blumlein. Alternate arrangements are shown in Figs. C.2b and C.2c. The transformer of Fig. C.2b is constructed by cutting off the pattern of Fig. C.1a just left of the point C and by using C as one of the secondary as well as one of the primary leads. The transformer of Fig. C.2c is constructed by winding the original sandwich back upon itself just after the point D and by using D as both a primary and a secondary lead.

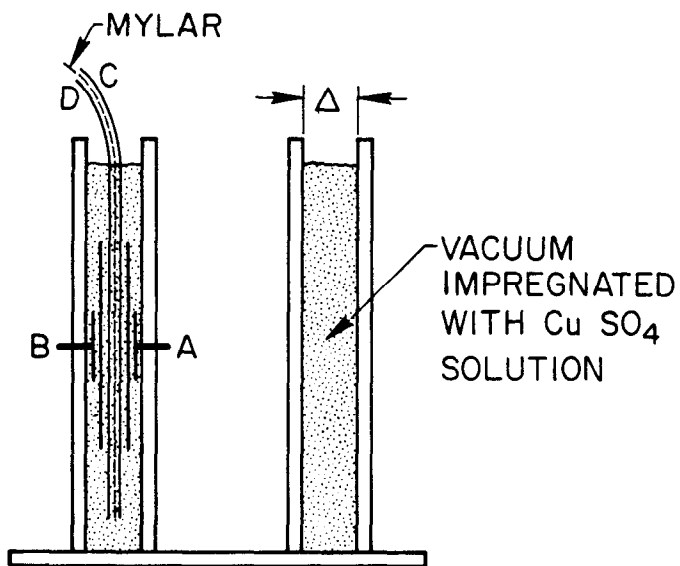
* The resistivity of the copper sulfate solution should be of the order 10^4 ohm-cm.



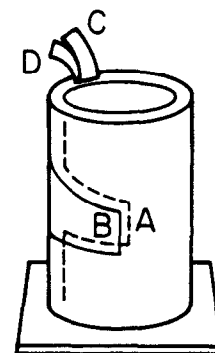
a.



b.



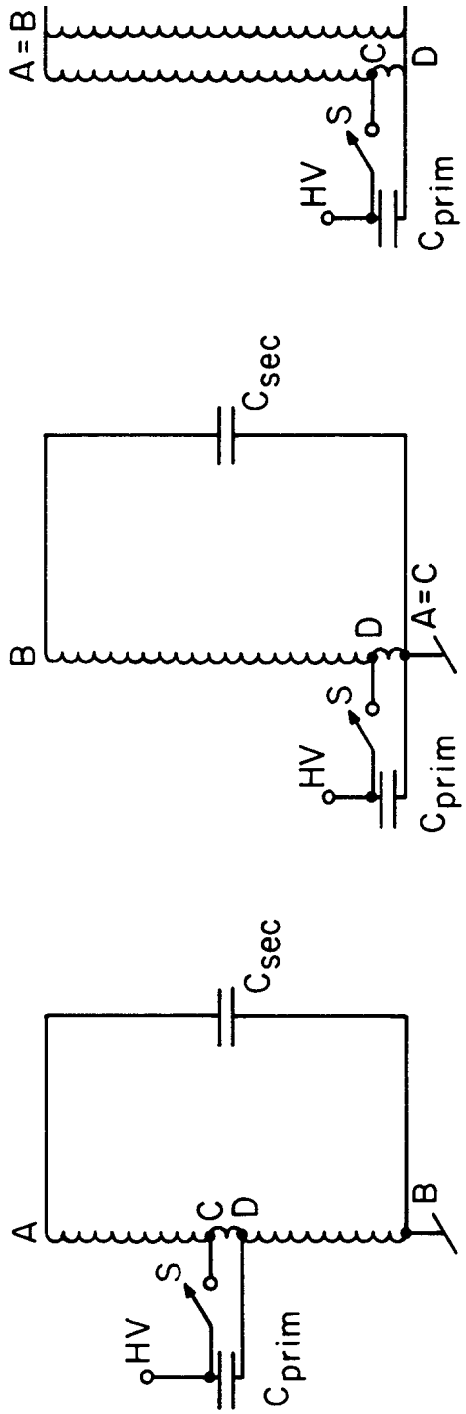
c.



d.

757A26

FIG. C. 1--Layout and construction details for the autotransformer developed by J. C. Martin and I. Smith of AWRE.



a. b.

FIG. C. 2--Three different circuit configurations for the autotransformer developed by J. C. Marti

An equivalent circuit for the autotransformer is shown in Fig. C.3. The leakage inductance L_{leak} in nH can be calculated from the total thickness of the windings Δ , the minimum and maximum widths of the windings b_{min} and b_{max} , and the radius of the transformer r :

$$L_{\text{leak}} = p \frac{36 \Delta r}{(2b_{\text{max}} + b_{\text{min}})} \text{ nH} . \quad (\text{C-1a})$$

The parameter p has a value of 1/2 for the circuit of Fig. C.2a, 2.0 for the circuit of Fig. C.2b, and 1.0 for the circuit of Fig. C.2c. All dimensions are in cm. The primary inductance is given by

$$L_{\text{prim}} = \frac{40 r^2}{r + b_{\text{max}}} \text{ nH} . \quad (\text{C-1b})$$

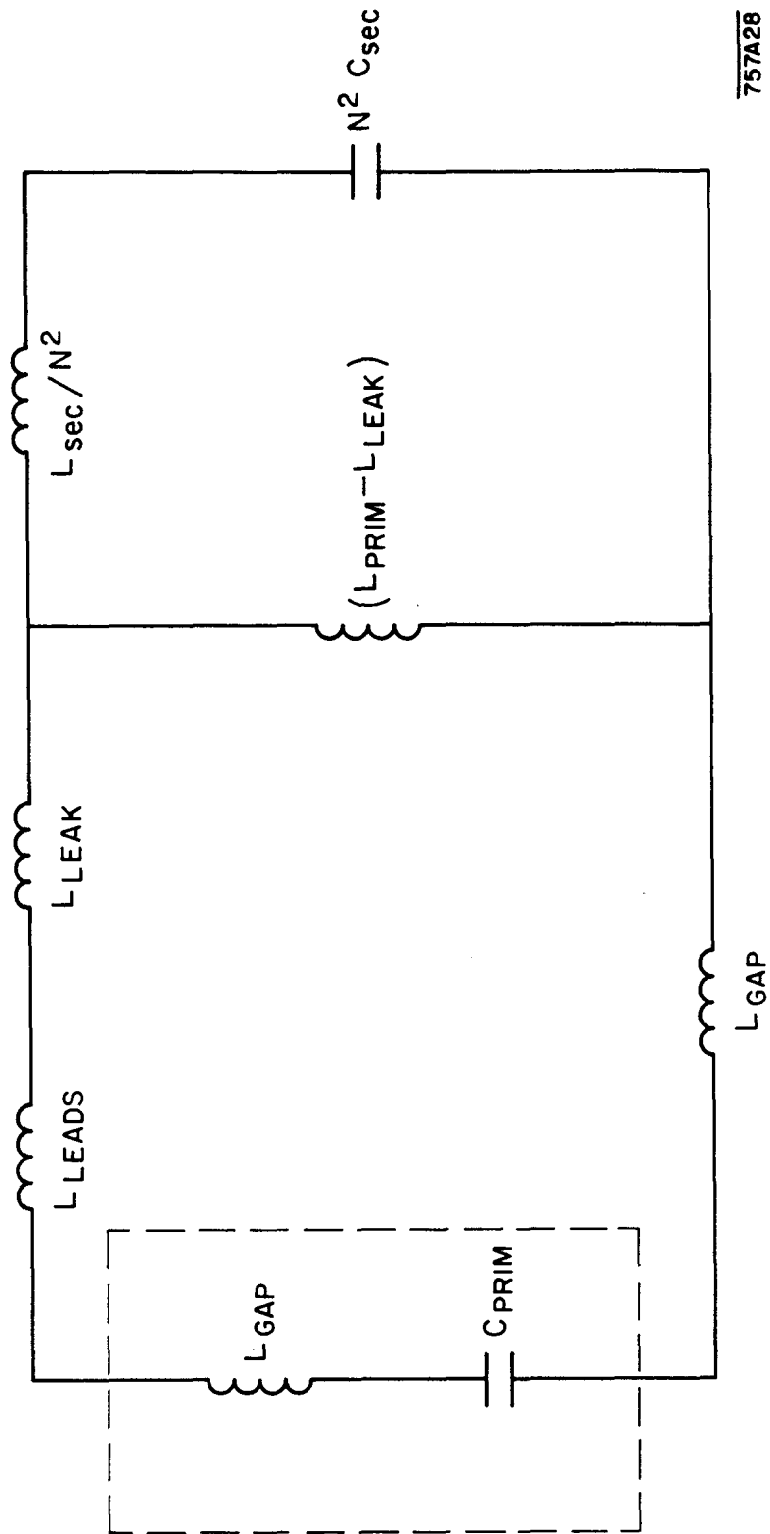
Neglecting L_{sec}/N^2 , the ratio of output to input voltages is given by

$$V_{\text{out}}/V_{\text{in}} = \left[\frac{L_{\text{prim}} - L_{\text{leak}}}{L_{\text{prim}} + L_{\text{leads}} + L_{\text{cap}} + L_{\text{gap}}} \right] [N] \left[\frac{2 C_{\text{prim}}}{C_{\text{prim}} + N^2 C_{\text{sec}}} \right] \quad (\text{C-1c})$$

where N is the turns ratio. The final factor, $2 C_{\text{prim}}/(C_{\text{prim}} + N^2 C_{\text{sec}})$, is the "ringing efficiency"; the first factor is an expression for the loss in voltage due to the various inductances. The rise time of the output pulse in nsec is given by

$$\begin{aligned} T &= \pi \left(L_{\text{total}} \cdot C_{\text{total}} \right)^{1/2} \text{ nsec} \\ &= \pi \left[\left(L_{\text{gap}} + L_{\text{cap}} + L_{\text{leads}} + L_{\text{leak}} \right) \left(\frac{C_{\text{prim}} N^2 C_{\text{sec}}}{C_{\text{prim}} + N^2 C_{\text{sec}}} \right) \right]^{1/2} \text{ nsec} \quad (\text{C-1d}) \end{aligned}$$

where L is expressed in nH and C in nF. It is assumed throughout that $2r$ is greater than b_{max} and that r is much greater than Δ .



757A28

FIG. C. 3--Equivalent circuit for the autotransformer developed by J. C. Martin and I. Smith of AWRE.

Some calculations based upon Eqs. (C-1a-d) are plotted in Figs. C.4 and C.5. In Fig. C.4, the rise time T is given as a function of b_{\max} for various values of r and for all three transformer configurations. The turns ratio N , typically in the range 16-20, was adjusted to satisfy the requirement $V_{\text{out}}/V_{\text{in}} = 800 \text{ kV}/50 \text{ kV} = 16$, where V_{out} was the required output voltage assumed for the two-meter chamber and where V_{in} was the voltage rating of two ESC 259* capacitors in series. Our intention in this case was to minimize the rise time for the given output voltage. The fixed parameter values were:

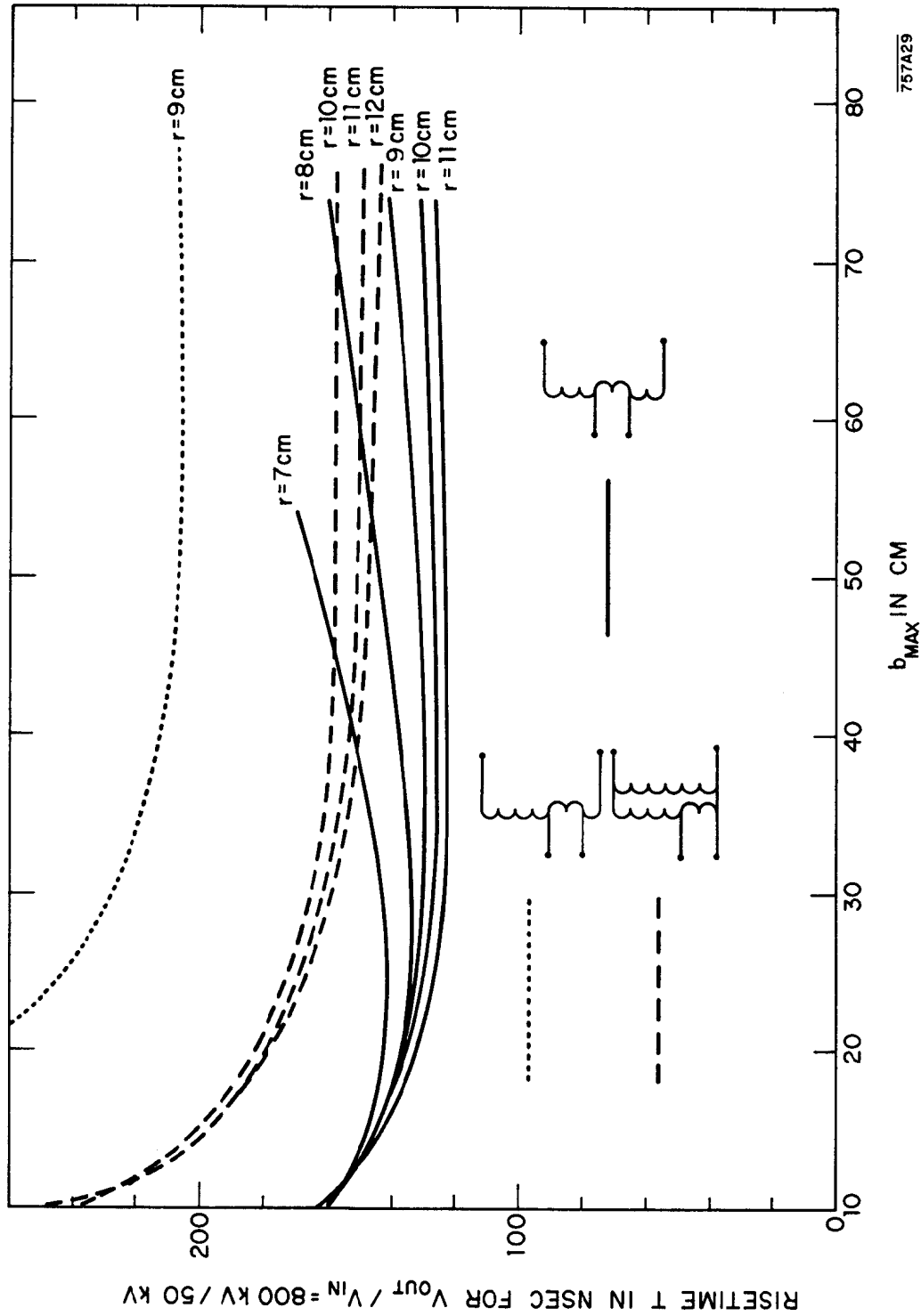
$$\begin{array}{ll}
 C_{\text{prim}} = 500 \text{ nF} , & L_{\text{leads}} = 6.0 \text{ nH} , \\
 V_{\text{in}} = 50 \text{ kV} , & C_{\text{sec}} = 0.9 \text{ nF} , \\
 L_{\text{cap}} = 1.0 \text{ nH} , & \Delta = 1.5 \text{ cm} , \\
 L_{\text{gap}} = 4.0 \text{ nH} , & \text{Input energy} = 624 \text{ joules} .
 \end{array}$$

As indicated in Fig. C.4, the center-tap transformer is preferred; however, it is inconvenient in practice since the input leads attain roughly half the output voltage during the pulse. The rise time decreases slowly with transformer radius (as long as $2\pi Nr \ll TC$), and it is fairly close to minimum for $b_{\max} \geq 20 \text{ cm}$.

In Fig. C.5, we have plotted V_{out} versus T for various values of r and b_{\max} in the center top configuration with four ESC 295 capacitors in series. In this case, the number of turns was chosen to maximize V_{out} ; the resulting value was $N = 16$ at every point. The fixed parameters were:

$$\begin{array}{ll}
 C_{\text{prim}} = 250 \text{ nF} , & L_{\text{leads}} = 6.0 \text{ nH} , \\
 V_{\text{in}} = 100 \text{ kV} , & C_{\text{sec}} = 0.9 \text{ nF} , \\
 L_{\text{cap}} = 2.0 \text{ nH} , & \Delta = 3.0 \text{ cm} , \\
 L_{\text{gap}} = 4.0 \text{ nH} , & \text{Input energy} = 1240 \text{ joules} .
 \end{array}$$

*Tobe Deutschmann Laboratories, Canton, Massachusetts



757A29

FIG. C. 4--Calculated rise time in nsec for $V_{out}/V_{in} = 800 \text{ kV}/50 \text{ kV}$ versus b_{max} , the maximum width of the tapered autotransformer winding. Calculations were made for the three circuit configurations indicated and for the transformer radii shown with each curve. Additional parameter values are included in the text.

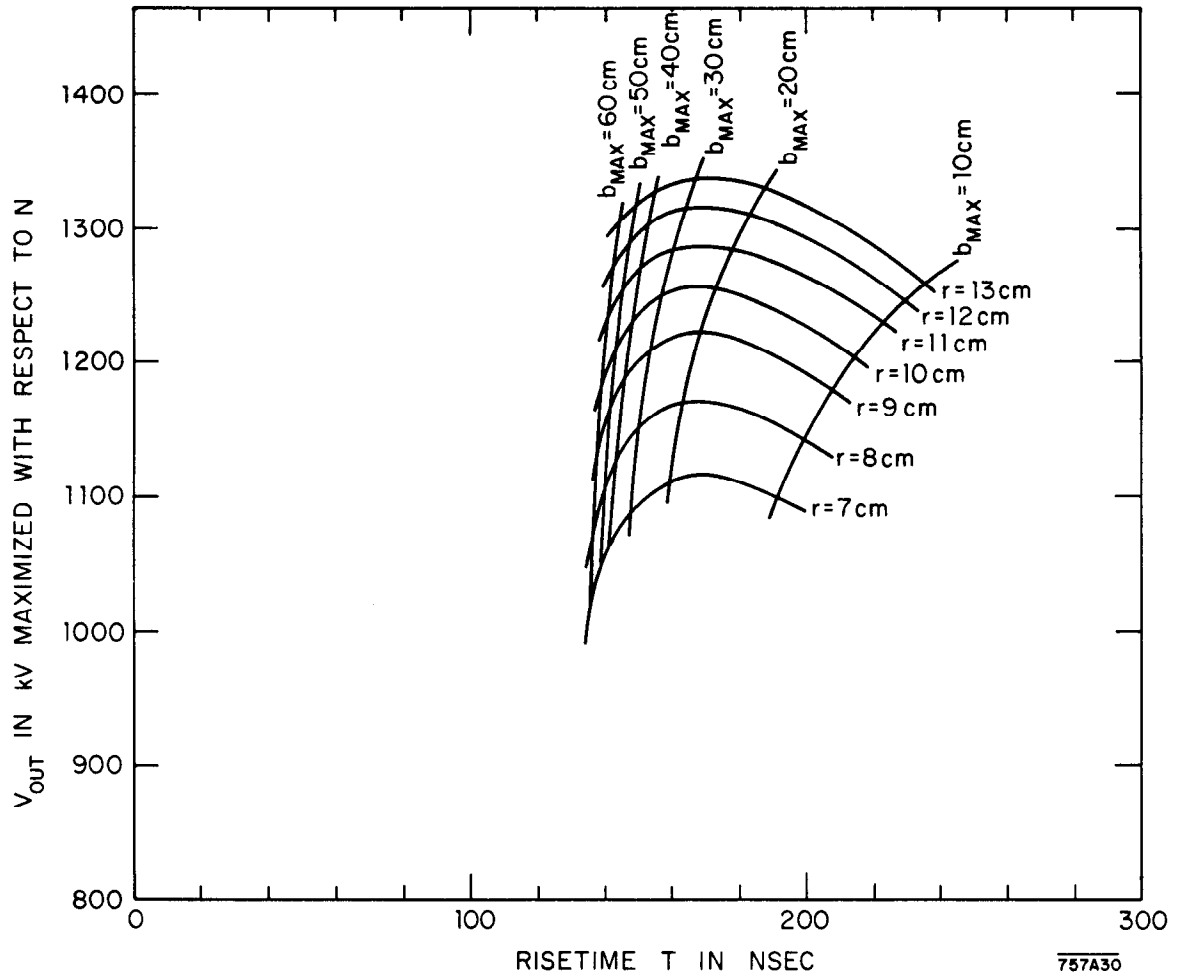


FIG. C.5--Calculated output voltage maximized with respect to the number of turns in a center-tap autotransformer versus the output rise time in μsec . The maximum width b_{MAX} of the tapered winding, and the radius r identify the different curves. Additional parameter values are included in the text.

Figure C.5 illustrates that the output voltage has a maximum as a function of T as well as b_{\max} and N , and that ultimately the rise time can be shortened only by sacrificing output voltage. Since the transformer would be followed in our application by a pulse-shaping network, the rise time is important only in that it adds to the delay in applying the final pulse to the streamer chamber.

REFERENCE

1. J. C. Martin and I. Smith, private communication.